

DEVELOPMENT of a FAST and HIGHLY EFFICIENT
GAS IONIZATION CHAMBER

for

PATIENT IMAGING and DOSIMETRY

in

RADIATION THERAPY

DE-FG07-00ID13918

R. Hinderler

H. Keller

T.R. Mackie

M.L. Corradini

Medical Physics and Nuclear Engineering & Engr. Physics
University of Wisconsin, Madison WI 53706

DEVELOPMENT of a FAST and HIGHLY EFFICIENT GAS IONIZATION CHAMBER
for
PATIENT IMAGING and DOSIMETRY in RADIATION THERAPY

R.Hinderler, H.Keller, T.R.Mackie, M.L.Corradini

Executive Summary

In radiation therapy of cancer, more accurate delivery techniques spur the need for improved patient imaging during treatment. To this purpose, the megavoltage radiation protocol that is used for treatment is also used for imaging.

The design of a highly efficient new detector based on gas ionization chamber technology will be optimized for megavoltage photon beams. High spatial resolution is achieved by dividing the gas volume into small cavities with metallic septal plates separating each gas cavity. When the septal plates are made of a suitable metal (e.g., aluminum, brass or tungsten), the septa serve as a buildup material for producing additional charged particles and, at the same time, limiting inter-channel cross-talk. This research project was successful in designing, fabricating, testing and evaluating such detectors for use in medical imaging.

Monte Carlo computer models were used to optimize the experimentally verified conceptual prototypes. The material composition, optimal dimensional spacings for the cavities and septal plates were determined, and can now be used to improve on the conceptual prototype design.

Our hypothesis was that such a detector would be more efficient and faster than current megavoltage detector technologies. This hypothesis proved to be reasonable accurate, and the detector can not only be used for imaging applications in a radiotherapy context, but could potentially be a non-destructive assay technique for waste characterization.

1. Introduction

1.1 Radiation therapy

Radiation therapy, or radiotherapy, is the treatment of diseases, in particular cancer, with ionizing radiation such as x-rays. Although radiation therapy is already a well-established treatment technique, there is still room for further improvement. Any improvement of the treatment outcome could increase the quality of life or even save the life of many patients. This thesis tries to make a small contribution.

1.2 Megavoltage photon detection and imaging in radiation therapy

1.2.1 The need for megavoltage photon detection and imaging

The goal of radiation therapy is the accurate delivery of a prescribed radiation dose to the target volume (tumor) while sparing the surrounding normal (healthy) tissue. However, even small deviations from the desired dose distribution can reduce the tumor control significantly or increase the rate of normal tissue complications (Dutreix 1984, Herring and Compton 1971). The International Commission on Radiation Units (ICRU) suggests the dose delivery to be accurate within $\pm 5\%$ (ICRU 1976). This places tight tolerances on all steps of radiotherapy including treatment planning and the actual radiation delivery. One of the most critical parts is the precise field placement with respect to the tumor during the entire course of treatment. The involved geometric uncertainties can be separated into two categories: setup errors, which refer to the positioning of the patient assuming no change in the anatomy, and organ motion, which refers to the position and shape of the target and surrounding critical structures. The latter point

includes, among other things, a potential change of the tumor's position and shape during the course of therapy, e.g. due to rectal filling or even breathing during the treatment itself. In addition, many tumors shrink during the course of treatment, which usually takes from six to eight weeks. Studies have shown that (significant) discrepancies in field placement frequently occur, especially for complicated cases (Marks *et al.* 1974, Rabinowitz *et al.* 1985). The advent of intensity modulated radiation therapy (IMRT) aggravates the problem further. IMRT uses nonuniform beam intensities to allow the delivery of dose distributions that conform to the target shape. This often results in steeper dose gradients, which make proper patient positioning an even greater concern (Swindell and Gildersleve 1991). However, imaging of the patient and the target volume can help to reduce the geometric uncertainties (Griffiths 1990, Marks *et al.* 1976). As the linear accelerator (linac) employs megavoltage x-rays to destroy the tumor, an obvious approach would be to make use of the megavoltage photons exiting the patient to acquire these images. Some suggest that patient positioning should be checked for many or even for each treatment session (fraction) (Leong and Shimm 1985). Adaptive radiation therapy relies on such a systematic treatment variation monitoring (Yan *et al.* 1997). The acquired data allows a re-optimization of the treatment (Wu 2002).

The ultimate function of imaging is not the acquisition of a high quality image but to aid the therapist in determining whether a patient is positioned properly or not. This requires a quantitative analysis on the basis of the acquired image, known as image registration. However, this task is not straightforward and there are many proposed methods. A brief summary of the different kinds of registration can be found in Munro (Munro 1995). Lu (Lu 2001) describes methods of motion detection and correction in conformal radiotherapy.

Megavoltage photon detector systems used in radiotherapy have potential applications other than imaging, e.g. delivery verification and dose reconstruction. Although desired in conventional radiotherapy, these applications are of particular interest in IMRT due to the complex beam shapes employed. Delivery verification uses the signal measured at the exit detector to determine the actual fluence incident on the patient (Kapatoes *et al.* 2001a). This allows the verification of the desired radiation delivery. Dose reconstruction, on the other hand, uses the incident fluence actually delivered and a computed tomography (CT) scan of the patient to determine the dose actually deposited (Kapatoes *et al.* 2001b). The dose distribution computed by dose reconstruction can be compared with the planned one.

Megavoltage photon detection and imaging is not only of interest in radiation therapy but also in other fields. Imaging of high-energy gamma rays can be used to characterize nuclear waste, such as identifying hot spots in mixed waste in order to reduce the volume of high-level waste that requires extensive treatment or long-term storage (Phillips 1995, Phillips 1997). Another application involves the acquisition of megavoltage CT (MVCT) images of dense or massive objects, especially for nondestructive material testing (Ruchala 1999).

1.2.2 Implementation: portal imaging and megavoltage CT

There are two general approaches to detect and form an image of megavoltage photons in radiation therapy - portal imaging and megavoltage CT. Portal imaging employs exit detectors to acquire megavoltage transmission images. Consequently, portal images are projection images. To get three-dimensional information, a set of orthogonal images can be acquired.

One of the most important developments for portal imaging was the introduction of portal films in 1966 (Swain and Steckel 1966). The film is placed in between a front metal plate and a rear plate made either of plastic or metal. The front plate generates high-energy electrons, while the rear plate acts as an electron backscattering material. Later, films with specialized film emulsions were developed whose sensitivities were appropriate for radiotherapy (Langmack 2001). Portal films can be categorized as either localization films, where only a small dose is used to get an image of the patient position or verification films, where the film is left in place for the entire duration of the treatment session. Although portal films still find widespread use at clinics they exhibit certain limitations, which include

- time consuming and labor intensive handling
- low contrast for megavoltage radiation, because of low subject contrast and scattered radiation
- no real-time imaging capability; thus limited possibilities of correcting the patient position prior to treatment
- analog detector, thus limited quantitative analysis (e.g. image registration) and processing (e.g. change of brightness and contrast of the object)

Digital detectors try to overcome these limitations. As a consequence, on-line electronic portal imaging devices (EPIDs) were introduced. They provide digital images that allow a quantitative analysis. Image processing like windowing and leveling can reduce the problem of low contrast. Imaging is usually performed in real-time, allowing intervention and intelligent use of the data.

The other approach to detect and image megavoltage photons is MVCT. MVCT goes one step further than portal imaging. It uses the linac beam to acquire CT images. Unlike portal images, MVCT images inherently provide 3-dimensional data. Another important difference is that MVCT images do not only show the patient's bony anatomy but also soft tissue details including the tumor. In addition, x-ray linear attenuation coefficients at megavoltage energies can be derived (Ruchala *et al.* 2000) and directly applied to tissue inhomogeneity corrections in treatment planning. The first MVCT system was developed at the University of Arizona (Tucson, Arizona) and later at the Royal Marsden Hospital (Surrey, England) by Swindell and colleagues (Lewis *et al.* 1988, Lewis *et al.* 1992, Simpson *et al.* 1982). In principle, portal imaging and MVCT do not necessarily require different detector technology. For instance, EPIDs can be used for cone beam MVCT imaging.

1.2.3 Types of detectors used

The modern era of electronic portal imaging began in the early 1980s with the acquisition of megavoltage transmission images with a fluoroscopic system developed by Baily *et al.* (Baily *et al.* 1980). Nowadays, there is a variety of EPIDs. Some of them are commercially available while other systems are "home-made". Commercially available systems include camera-based EPIDs (Shalev *et al.* 1989, Visser *et al.* 1990) and matrix ion chambers (Meertens *et al.* 1985, van Herk and Meertens 1988). However, they have never found widespread clinical usage. Much more promising are the so-called active matrix flat panel imagers (AMPFIs). AMPFIs are currently introduced to diagnostic imaging (Yaffe and Rowlands 1997) but they also show great promise in portal imaging (Antonuk 1993) and cone beam MVCT (Groh *et al.* 2002, Jaffray and Siewerdsen 2000, Jaffray *et al.* 2000, Midgley *et al.* 1998, Mosleh-Shirazi *et al.* 1998a). In

megavoltage photon imaging an additional metal plate is placed above the detector to increase the detection efficiency. The incoming megavoltage x-rays interact in the metal and produce high-energy electrons, which subsequently deposit their energy in the detection medium. These detectors use either the indirect or the direct approach to detect x-rays. Indirect detection is based on the conversion of x-rays into visible and ultraviolet light through use of a scintillating screen and a subsequent conversion of these photons into electron-hole pairs with a photosensitive pixel array. Antonuk *et al.* (Antonuk *et al.* 1990, Antonuk *et al.* 1991a) developed such a detector using an amorphous silicon (a-Si) readout array. Each pixel element of the array consists of a photodiode and a thin film transistor (TFT). The TFT controls the readout of the signal. Amorphous silicon has the advantage of being resistant to radiation-damage. Direct detection, on the other hand, is based on the direct conversion of x-rays into electron-hole pairs within a photoconductor like amorphous selenium (a-Se) (Falco *et al.* 1998, Mah *et al.* 1996, Zhao and Rowlands 1992). These charges are separated and collected through the use of an electrical field that is applied between a metal plate and an array of detector pixel electrodes. The charges are stored by capacitors in the pixel electrodes. At the present time it is unclear, if the direct detection method offers advantages over the indirect detection method.

In addition to these commercially available detectors, there are many “home-made” systems. For instance, Taborsky *et al.* (Taborsky *et al.* 1982) developed a scanning-diode array. It uses a linear array of silicon photodiodes which is translated through the field. On the contrary to area detectors, such a linear array utilizes only a small fraction of the available radiation. Only scanning systems with a significantly higher efficiency than area detectors could compensate for this drawback. Swindell’s group (Morton *et al.* 1991, Swindell *et al.* 1988) investigated a

scanning array of zinc tungstate detectors with some 50% efficiency. Recently, this group also presented the construction of a large-area detector with a quantum efficiency (QE) of about 18% (Mosleh-Shirazi *et al.* 1998b, Mosleh-Shirazi *et al.* 1998c). This detector employs the same components and imaging geometry as the present camera-based EPIDs except for the use of a two-dimensional array of custom-made 1 cm thick CsI(Tl) scintillation crystal detector elements instead of the conventional phosphor screen. The crystals are thick enough to attenuate the photon beam significantly. Besides the high QE, the system offers the advantage of a significantly increased optical coupling efficiency due to the columnar structure of the used scintillator. The cost for such a scintillation crystal array, however, might be prohibitive.

1.2.4 Helical tomotherapy and its megavoltage photon detector

Helical tomotherapy is radiation therapy using a rotating fan beam of intensity-modulated radiation (Mackie *et al.* 1993, Mackie *et al.* 1999, Olivera *et al.* 1999). In helical tomotherapy, the linear accelerator, a multi leaf collimator (MLC) and a megavoltage photon exit detector are integrated together on a single gantry. An MLC is a mechanical device that modulates the intensity of the x-ray beam. An artist's rendition of a tomotherapy unit is shown in figure 1.1.

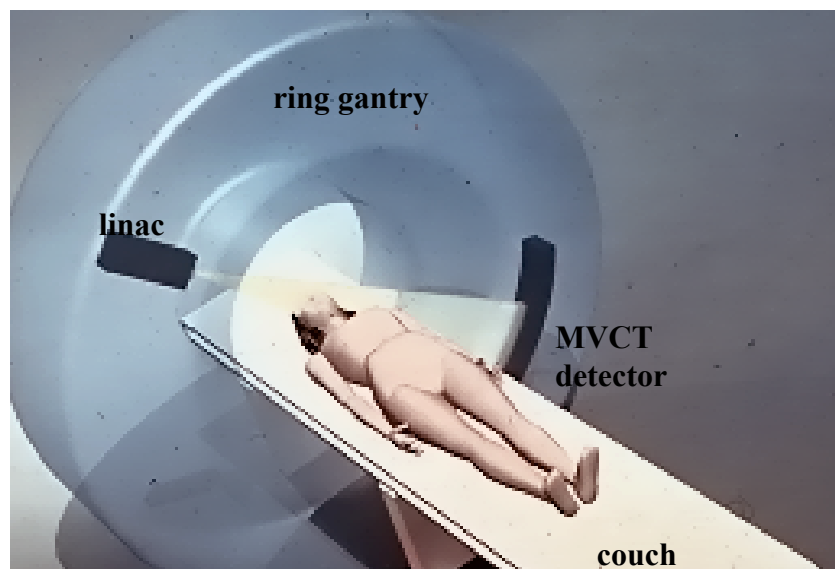
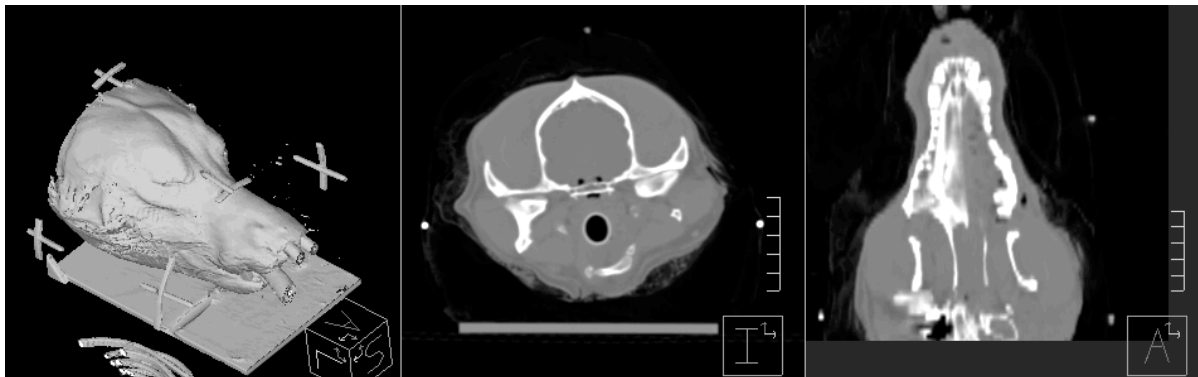


Figure 1.1 Artist's rendition of a helical tomotherapy unit. A linear accelerator (linac) is used to irradiate the tumor of the patient with megavoltage x-rays. Megavoltage photons exiting the patient are detected with a megavoltage CT detector (MVCT detector). A ring gantry allows the linac as well as the detector to rotate around the patient.

The megavoltage photon detector employed is a 738-channel General Electric Medical Systems single row xenon gas ionization detector (Milwaukee, WI). Its structure is discussed in detail in chapter 3.2.1. Although originally designed for applications in diagnostic CT, this detector proved to be very useful for MVCT (Ruchala *et al.* 1999, Ruchala *et al.* 2002). Figure 1.2 shows a volume rendering of an image set, a transverse as well as a coronal tomographic slice image of a German shepherd head cadaver acquired on the University of Wisconsin - Madison tomotherapy benchtop unit. For comparison, the equivalent kVCT images are included. It should be emphasized that these MVCT images are significantly better than the images typically seen in the literature especially for comparable radiation doses imparted (Guan and Zhu 1998, Hesse *et al.* 1998, Jaffray *et al.* 1999). Besides MVCT, the detector is used for a variety of other tasks including delivery verification and dose reconstruction.



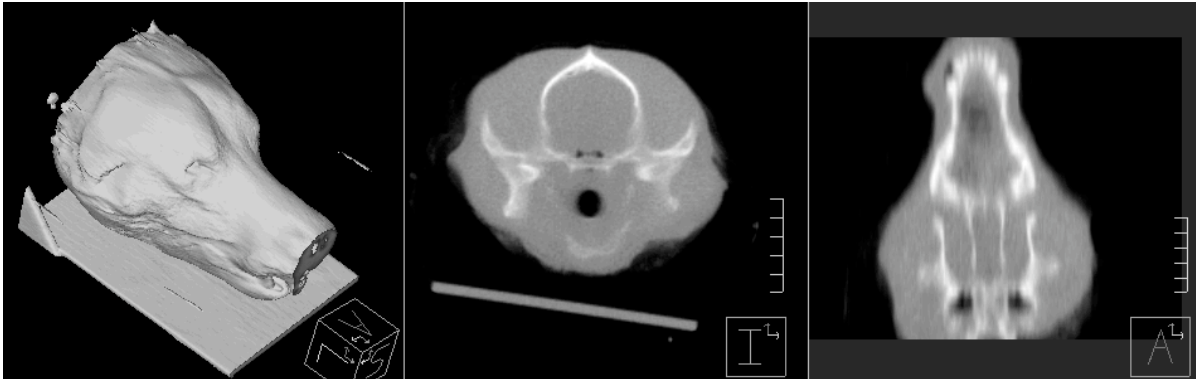


Figure 1.2 A volume rendering of an image set (left), a transverse (center) as well as a coronal tomographic slice image (right) of a German shepherd head cadaver acquired on the University of Wisconsin tomotherapy benchtop unit. The upper row shows a 6 cGy kVCT on a Siemens Hi-Q scanner and the lower row shows a 10 cGy MVCT image acquired with the 738-channel General Electric xenon detector (Courtesy of K. Ruchala, Tomotherapy Inc.).

1.3 Assessment of the image quality

The quality of an image is defined by its usefulness to serve a certain task. In radiology, for instance, the quality of an image is characterized by its usefulness in determining an accurate diagnosis. Image quality, however, is subjective and depends on the function of the image. In general, the quality is determined by physical parameters as well as by the observer's perceptual response. The assessment of both aspects became more difficult with the advent of digital images. Unlike analog systems, images from digital devices have been sampled, quantized and processed. Image processing provides an almost unlimited degree of image manipulation, which makes the gauging of observer response very challenging. Unlike the observer's response, the physical parameters can be objectively quantified. A minimum analysis would include the characterization of the signal transfer through the (detector) system in form of the modulation transfer function and the noise in form of the noise power spectrum. Both quantities can be

incorporated in the so-called detective quantum efficiency. All of these quantities can either be derived from the raw data of the detector or from the final image. In the latter case not only the characteristics of the detector are of importance but also the subsequent processing of the raw data whereas in the former case the quantities of interest are solely determined by the characteristics of the detector (and maybe by the source and detection geometry used).

1.4 Thesis motivation and objectives

A major challenge of imaging with high-energy photons is the intrinsically low subject contrast. At megavoltage energies the photon mass attenuation coefficients for different kinds of soft tissues are very similar. These coefficients, however, ultimately determine the image contrast. The low subject contrast is in part compensated by the higher photon fluence impinging on the detector in comparison to diagnostic radiology. The higher photon fluence can be attributed to the much higher doses delivered in radiation therapy. In addition, high-energy photons are much more penetrating and primary x-ray quanta are not attenuated by grids, which are usually employed in diagnostic radiology. To make use of the higher fluence, efficient megavoltage photon detectors are required. Currently employed EPIDs, however, have a quantum efficiency of only 2% to 4% for megavoltage beams (Pang and Rowlands 2002). Even the promising flat panel imagers reach a DQE value at zero spatial frequency of only about 1% (El-Mohri *et al.* 2001, Munro and Bouius 1998). The relatively poor image quality of current EPIDs is due to poor characteristics of the systems themselves rather than a fundamental limitation of imaging with megavoltage photons (Boyer *et al.* 1992). This fact holds promise for future EPIDs that may far outperform those described in the previous section.

The xenon CT detector used for the helical tomotherapy unit shows great promise in this respect. A quantum efficiency of 44.4% and a detective quantum efficiency at zero spatial frequency of 31.4% were reported in recent Monte Carlo studies (Keller *et al.* 2002). However, the detector design exhibits certain limitations that motivate the development of a new system based on the same principle of photon detection. The single row detector cannot easily be extended to an area/multirow detector. In addition, this type of detector is no longer manufactured. Design of a new system, on the other hand, allows an optimization of the geometry specifically for the detection of megavoltage photons, for instance through Monte Carlo simulations. Not only do physical considerations play an important role in the development but also financial and technical issues as well. One objective of this thesis is the development of small-scale prototype detectors based on a novel efficient principle of megavoltage photon detection and imaging. Another objective is the Monte Carlo simulations of the prototype detectors as well as of proposed larger detector arrays. The objectives also include a more detailed study of the physical principle of megavoltage photon detection. From the resulting findings design considerations of a large-scale detector, which is capable of portal imaging or MVCT imaging, can be derived.

1.5 Thesis outline

The first part of the thesis deals with the development of single element prototype detectors. These detectors were characterized in a series of measurements. As a proof-of-principle of the novel concept of megavoltage photon detection and imaging, MVCT images of a contrast resolution phantom were acquired. Due to the encouraging first findings, multielement detectors

were developed and tested as described in the following section of the thesis. Monte Carlo simulations of these prototypes provided additional information about the process of megavoltage photon detection and the significance of the design. The next part of the thesis describes the transition to a larger detector array. It was found that the extension to a multirow/area detector requires a careful investigation of the design prior to the manufacturing process. For this purpose, Monte Carlo studies of a proposed multirow/area detector were performed. One way to evaluate a given detector design is to split the signal of a detector element into a primary and crosstalk component. This approach resulted in valuable design considerations. It has, however, certain limitations. Thus, a more comprehensive analysis in form of the determination of the detective quantum efficiency (DQE) was investigated. The DQE is probably the single best quantity to quantify the efficiency and performance of a given detector design. As a first step towards the determination of the DQE, several methods to determine the modulation transfer function of the investigated detector array were determined. Besides the development of the prototype detectors, this constitutes a major part of the thesis since the determination of the modulation transfer function of a detector with a severely inhomogeneous detection medium has never been investigated in detail before. The other quantity required to determine the DQE is the so-called noise power spectrum. Its derivation is sketched in the final part of the thesis. Figure 1.3 shows a schematic outline of the thesis.

The thesis concludes with a wealth of design considerations of a large-scale detector for megavoltage photons resulting from the development of the prototype detectors, the experimental studies and the Monte Carlo simulations.

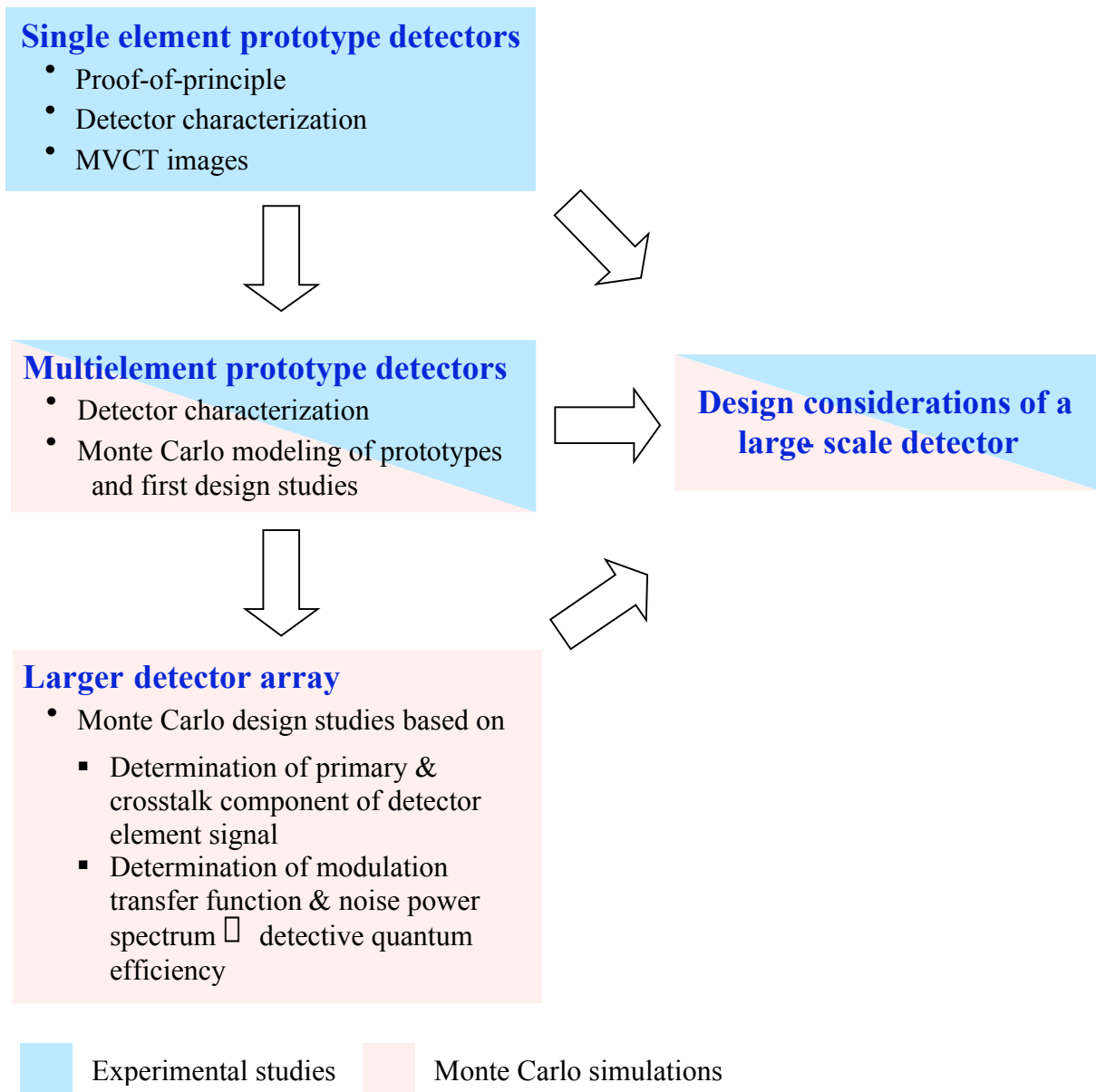


Figure 1.3 Schematic outline of the thesis

2. Theory

This chapter discusses the theory behind the evaluation of the performance of a digital detector in more detail. The evaluation is largely based on the determination of the modulation transfer function (MTF), the noise power spectrum (NPS) and the detective quantum efficiency (DQE) of a digital detector. The DQE, which combines the MTF and the NPS, can serve as a single quantity to judge the performance of a detector system. For the sake of clarity, most of the following discussion focuses on a one-dimensional description. The extension to the two-dimensional case is relatively straightforward. In addition, the spatial frequency will be referred to as simply the frequency in the following paragraphs.

2.1 Performance evaluation of digital detectors

The characterization of the performance of a detector is based on a sophisticated theory. As the response of a detector system is spatially correlated, a large part of the theory relies on a description in the frequency domain. Spatial correlation means that the response at a given location is not independent from the response(s) at other locations. In particular, the signal as well as the noise are always to some degree spatially correlated. The main concept of the frequency description includes the MTF, which describes the signal transfer through the system, the NPS, also called Wiener spectrum, which describes the noise characteristics, and finally the DQE, which combines the two former quantities (ICRU 1995). The DQE is probably the single best quantity to describe the performance of a detector (Metz *et al.* 1995). These concepts have been applied in a relatively straightforward fashion to analog systems, such as screen film

systems (Barnes 1982, Bunch *et al.* 1987, Bunch 1989, ICRU 1986). A modification of these concepts allows their applications to digital systems (Dobbins III *et al.* 1992, Hillen *et al.* 1987, Wagner and Sandrik 1979). The interpretation of the results, however, requires great care when the digital system is undersampled.

Undersampling occurs when the image is not sampled fine enough. A digital detector can record all input signals properly with frequencies up to the so-called cutoff frequency f_c . This frequency is determined by the Nyquist theorem and can be calculated as

$$f_c = \frac{1}{2 \Delta x} , \quad (2.1)$$

where Δx designates the sampling interval and $1/\Delta x$ the sampling rate. Δx can also be interpreted as the detector pitch, the center-to-center distance of two abutting detector elements. If the object to be imaged contains signals with frequencies beyond the cutoff frequency and if the MTF extends beyond the cutoff, aliasing will occur. Signals with frequencies beyond the cutoff will be mapped back to lower frequencies by reflecting them at the cutoff frequency. Thus, these higher frequencies masquerade or take the "alias" of another, lower frequency.

In practice almost all digital systems are to some degree undersampled due to practical constraints. The design of a suitable system and the need for a reasonable size of the image data usually dictate the choice of the sampling rate. One difficulty with undersampling is the resulting lack of spatial invariance. Spatial invariance is an important practical requirement of the linear-systems theory. The above concepts, however, are based on this theory. An important consequence of the lack of spatial invariance is that the response of the system to a delta function input depends on the location of the input with respect to the detector matrix.

Mathematically, the system response depends on the location (phase) of the sampling comb with respect to the object to be imaged. The general concepts of the performance evaluation of detectors can be modified so that they are applicable to undersampled systems as will be outlined in the following section. Dobbins provides an excellent description of the proper interpretation of the MTF, NPS and DQE for digital detector systems, which might be undersampled (Dobbins III 1995, Dobbins III 2000).

2.2 Presampling MTF and digital/expectation MTF

The MTF describes the transfer of the modulation of a sinusoidal signal from the input of a (detector) system to its output for all spatial frequencies. There are two general definitions of the MTF. First, the MTF can be defined by means of the response of a system to a single frequency sinusoidal input. In the absence of aliasing, the response is a sinusoidal output signal with the same frequency as the input but with a reduced amplitude. The MTF curve describes the response at all frequencies. Knowing the maximum (max) and minimum (min) value of the sinusoidal input (in) and output (out) signal, the value of the MTF at the frequency f of the sinusoid can be determined as

$$MTF(f) = \frac{\frac{\max_{out}(f) - \min_{out}(f)}{\max_{out}(f) + \min_{out}(f)}}{\frac{\max_{in}(f) - \min_{in}(f)}{\max_{in}(f) + \min_{in}(f)}} \quad (2.2)$$

In optics, sine wave test patterns are commercially available (e.g. on a film) (Boone *et al.* 1996). Interestingly, Johansson *et al.* generated an optical sine wave pattern interferometrically

(Johansson *et al.* 1991). It is, however, very difficult to generate a sinusoidally varying x-ray intensity. In practice, a square wave pattern (bar phantom) is employed (Dainty and Shaw 1974, Stiersdorfer and Spahn 1999), which produces a sinusoidally varying x-ray intensity including some higher harmonic contributions. This approach, however, is not recommended for a rigorous evaluation of the MTF.

The other definition describes the MTF as the response of a system to a delta function input:

$$MTF(f) = |OTF(f)|, \quad (2.3)$$

where OTF designates the optical transfer function. In two dimensions the OTF is defined as the Fourier transform of the point spread function (PSF), the output of a system in response to a delta function at its input. The OTF and thus the MTF are normalized to 1 at zero frequency. The concept of the line spread function (LSF) is similar to the PSF. The LSF describes the response of a system to a line input. The result is a one-dimensional MTF in the direction perpendicular to the line input. For measurements, the LSF is often preferred over the PSF (Barrett and Swindell 1981). When a radiation beam is collimated to approximate a point source, there might be very little radiation left. This is less of a problem for a beam that is collimated with a thin slit to approximate a thin line source.

The equivalence of the two general definitions of the MTF can be understood, when the LSF is represented as a sum of sine waves ranging in frequency from 0 to infinity. The relative modulation of each sine wave and thus its amplitude is given by the MTF. For digital systems, however, the two definitions are only equivalent, if the system is not undersampled.

To circumvent the problem of undersampling, two alternative descriptions of the classical MTF were introduced: the presampling MTF (MTF_{pre}) and the expectation MTF (EMTF). MTF_{pre} excludes the final stage of sampling, which introduces aliasing in case of undersampling. Sampling results in one sample per detector pitch Δx . The result is a digital MTF (MTF_d), which is only defined up to the cutoff frequency (although MTF_d is replicated at higher frequencies). If MTF_{pre} extends beyond the cutoff frequency, the detector will be confronted with the aliasing

effect. When MTF_{pre} is determined, the aliasing effect is avoided by sampling the response of the detector at a much higher rate than the actual sampling rate of one sample per detector pitch. This aspect is particularly important for delta and line-type input signals as they represent broad frequency inputs. Fujita *et al.* (Fujita *et al.* 1992) describe a method how such an oversampling can be achieved. The authors introduced the so-called slanted slit technique to measure an oversampled LSF. Here the slit, defining the line input, is aligned at a small angle with respect to a detector row (column). The actual sampling rate depends on the tilt angle. Another way to achieve oversampling is to determine the detector response for a whole series of delta function or line inputs, which are displaced by a subdetector element increment (Dobbins III 1995, Park *et al.* 1984). In general, the oversampling rate has to be chosen in such a way that the associated cutoff frequency is so high that any residual aliasing is negligible.

The EMTF, on the other hand, is based on the digital OTF (OTF_d). OTF_d can be determined by taking the Fourier transform of the system response when a delta function is the input. In case of undersampling, OTF_d has a phase (location) dependence due to the lack of shift invariance. If the delta function points at a location, which is at the distance a relative to the origin (center) of the detector element, then the amplitude of OTF_d at the frequency f_1 can be determined as (Dobbins III 1995):

$$|OTF_d(f_1, a)| = \sqrt{\sum_{i=1}^N \sum_{j=1}^N MTF_{pre}^2(f_i) + \sum_{i=1}^N \sum_{\substack{j=1 \\ j \neq i}}^N [R(f_i)R(f_j) - P_{ij} I(f_i)I(f_j)] \cos[2\pi a(f_i + P_{ij}f_j)]} \quad (2.4)$$

$$\sqrt{\sum_{i=1}^N \sum_{\substack{j=1 \\ j \neq i}}^N [I(f_i)R(f_j) + P_{ij} R(f_i)I(f_j)] \sin[2\pi a(f_i + P_{ij}f_j)]}^{1/2}$$

$0 \leq f_i \leq f_c$

where $P_{ij} = -1$ if i and j are both odd or both even and $P_{ij} = +1$ if i and j have opposite parities. $R(f)$ and $I(f)$ are the real and imaginary components of OTF_{pre} . The variable a can also be interpreted as the phase. Interestingly, if the digital system was not undersampled, Eq. (2.4) would reduce to a single term, leaving $|OTF_d(f_1, a)| = MTF_{pre}(f_1)$ in the range of $0 \leq f_1 \leq f_c$. Sampling results in the replication of OTF_d in frequency space. These replica, however, only overlap and cause aliasing, when the system is undersampled.

Similar to Eq. (2.3), the relationship between OTF_d and MTF_d is given by

$$MTF_d(f_1, a) = |OTF_d(f_1, a)| \quad \text{for } 0 \leq f_1 \leq f_c \quad (2.5)$$

Finally, the EMTF is obtained as the average of MTF_d over all phases of the sampling comb.

The EMTF is then

$$EMTF(f_1) = \langle MTF_d(f_1, a) \rangle = \frac{1}{\Delta x} \int_0^{\Delta x} da |OTF_d(f_1, a)| \quad \text{for } 0 < f_1 < f_c, \quad (2.6)$$

where the average over all possible phases ranges from 0 to Δx . The result is an approximate “average MTF” that is spatially shift invariant. The Eqs. (2.4) - (2.6) relate EMTF to MTF_{pre} (OTF_{pre}).

Table 2.1 contrasts the concept of MTF_{pre} and EMTF (MTF_d). MTF_{pre} describes the response of a digital system to a single sinusoid input, i.e. modulation out as a fraction of modulation in. MTF_{pre} is often used to evaluate modifications of a given detector design and to compare different kinds of detector systems. EMTF (MTF_d), on the other hand, is more suitable to describe the final, sampled image. A reliable quantitative comparison of two digital systems

using EMTF (MTF_d), however, requires great care. When there is undersampling, such a comparison is not at all straightforward, as illustrated in the following example (Dobbins III 1995).

Figure 2.1 shows MTF_{pre} and MTF_d of two hypothetical systems. System 1 has a typical MTF_{pre} that extends beyond the cutoff frequency, i.e. the system is undersampled. This is not true for system 2. Its MTF_{pre} exhibits a sharp cutoff at f_c . Although both systems have quite different MTF_{pre} the MTF_d are identical. Consequently, both systems would respond equivalently to a line-type input since such an input corresponds to a broad frequency input. For a single sinusoid near the cutoff frequency, however, system 2 is clearly superior. The corresponding value of its MTF_{pre} is significantly higher than for the other system.

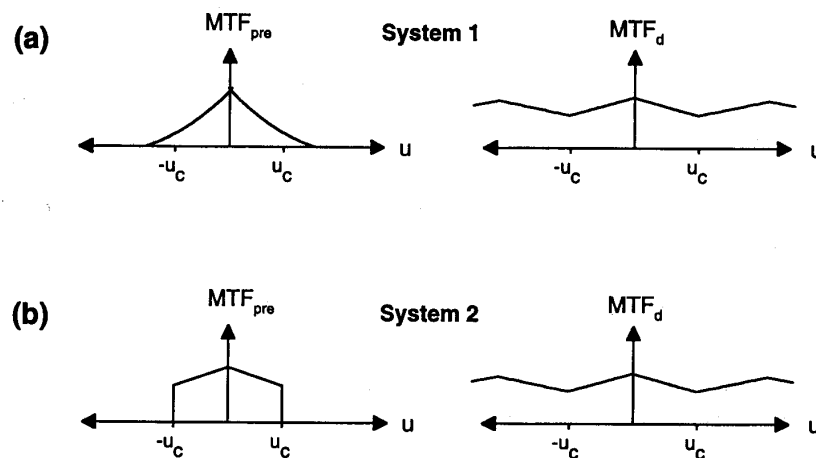


Figure. 2.1 Illustration of the unreliability of a comparison of two digital detector systems based on the digital MTF (MTF_d) when undersampling is present. The figure shows the presampling MTF (MTF_{pre}) and the MTF_d for two hypothetical systems. Although both systems have identical MTF_d their MTF_{pre} are quite different. u_c designates the cutoff frequency (from Ref. (Dobbins III 1995)).

intentionally blank

In a mathematical sense, the values of these digital quantities outside the range $0 \leq f_1 \leq f_c$ can be found by reflecting the function about the zero frequency (to get the symmetric negative part of the function) and replicating it every $2f_c$ (to get the replica in frequency space). For practical purposes, however, the digital quantities are only defined from zero frequency up to the cutoff frequency since the detector is only able to provide frequency information within that range.

2.3 Digital noise power spectrum

The NPS can be thought of as the variance of the image intensity (i.e. image noise) as a function of the frequency. Unlike MTF_d in the undersampled case, the digital NPS (NPS_d) is always shift invariant. NPS_d has no phase (location) dependence because the NPS is defined as an ensemble average. The ensemble average includes contributions from all possible random phases of the noise. NPS_d , however, is also plagued with the problem of aliasing. The noise components with frequencies greater than f_c get aliased into the image noise at lower frequencies. Similar to MTF_d , NPS_d can be expressed as (Giger *et al.* 1984)

$$NPS_d(f) = NPS_{pre}(f) \sum_{n=-\infty}^{\infty} \delta(f - n \cdot \frac{1}{\Delta x}) = NPS_{pre}(f) + \sum_{n=1}^{\infty} NPS_{pre}(f \pm \frac{n}{\Delta x}), \quad (2.7)$$

where NPS_{pre} denotes the “presampling” NPS, the NPS of the system excluding the final sampling stage. \sum designates the sampling comb, i.e. a string of delta functions separated in frequency space by the reciprocal of the detector pitch Δx .

In practice, it is not possible to measure NPS_{pre} because any input contains all noise frequencies simultaneously, including those above f_c . NPS_d , on the other hand, can be

determined by collecting a series of so-called flood field images. Flood field images are acquired with a broad beam that covers a large part of the detector matrix without an object in place. Taking into account the discrete nature of the digital detector, NPS_d can be determined for the *two-dimensional case* as

$$NPS_d(u, v) = \lim_{N_x, N_y, \Delta x, \Delta y} \lim_{M \rightarrow \infty} \frac{N_x N_y \Delta x \Delta y}{M} \sum_{m=1}^M \left| FT \left\{ I_m(x, y) - \bar{I}(x, y) \right\} \right|^2, \quad (2.8)$$

where u and v stand for the frequency variables in two dimensions. N_x , N_y and Δx , Δy designate the number of the detector elements, the detector element width, respectively, in the x- and y-direction. M denotes the number of flood field images $I(x, y)$. $\bar{I}(x, y)$ is the average flood field image. Ideally, N_x , N_y as well as M go to infinity. In practice, however, it is sufficient when these quantities are large enough. The meaning of “large enough” must be judged for each detector system separately. Eq. (2.8) assumes that the forward Fourier transform includes the factor $1/(N_x \cdot N_y)$.

2.4 Digital detective quantum efficiency

The DQE combines the two quantities MTF and NPS. It is a measure for how much less efficient a given detector system utilizes the signal-to-noise ratio (SNR) at its input in comparison to an ideal detector. For the two-dimensional case the digital DQE (DQE_d) can be calculated as

$$DQE_d(u, v) = \frac{MTF^2(u, v)}{SNR_{in}^2 NNPS_d(u, v)} \quad (2.9)$$

where SNR_{in} designates the SNR at the input of the detector system (see discussion below). There is a debate on what to use for the MTF. Some authors use the EMTF (Neitzel *et al.* 1994), whereas others employ MTF_{pre} (Fujita *et al.* 1989). For a comprehensive treatment of the problem, Dobbins suggests to report the DQE_d for both kinds of MTFs. Finally, $NNPS_d$ denotes the digital normalized NPS, which can be determined as

$$NNPS_d(u, v) = \frac{NPS_d(u, v)}{(large\ area\ signal)^2} \quad (2.10)$$

The large area signal, in turn, is the average detector element signal for a given exposure with a broad beam.

The DQE_d is sometimes also written as

$$DQE_d(f) = \frac{SNR_{out}^2(f)}{SNR_{in}^2(f)} \quad (2.11)$$

where SNR_{in} and SNR_{out} designate the signal-to-noise ratio at the input and output of the detector, respectively. The SNR_{in} is set equal to SNR_{ideal} , where SNR_{ideal} refers to the SNR of an ideal detector. There is, however, no consensus on what is considered to be the ideal detector when an energy integrating detector, irradiated with a polyenergetic beam, is investigated. Energy integrating means that the detector element response can directly be related to the amount of energy deposited in the element. Some authors (Dainty and Shaw 1974, Tapiovaara and Wagner 1985, Zhao *et al.* 1997) argue that a photon counting detector should always be regarded as the ideal detector. Hence, the noise at the input is solely determined by the varying number of photons incident on the detector (Poisson noise). In this case SNR_{in}^2 is equal to the average number of incident photons per unit area. Other authors (Dobbins III *et al.* 1995, Hillen *et al.* 1987) consider most of the x-ray detectors to be energy integrating detectors. Thus, the

energy would be the relevant quantity. This implies that besides the Poisson noise, the additional noise originating from the polyenergetic nature of the beam has to be included in the determination of SNR_{in} . It is recommended that Eq. (2.9) should be taken as the general definition of the DQE_{d} .

3. Materials and Methods

3.1 *Novel principle of megavoltage photon detection and imaging*

Most of the MV photon detectors currently employed in radiation therapy are based on the same design principle. It consists of a front metal plate to increase the detection efficiency and an underlying active medium (also known as recording medium). The incoming megavoltage photons interact in the metal mostly through the Compton effect and produce high-energy electrons. Subsequently, these electrons deposit their energy in the active medium as shown in figure 3.1 (a). However, only a small fraction of the incident photons interacts in the metal plate. Thicker plates can increase the number of interacting photons but at the same time the fraction of high-energy electrons reaching the active medium decreases. In addition, the larger thickness results in an increased spread of the high-energy electrons and thus in a spatial degradation of the signal. The active medium usually has a lower density so that only a small part of the incident photons directly interact there. As for the metal plate, a thicker active medium usually results in a blurring of the signal.

This work investigates a new approach (Hinderer *et al.* 2001), which places the metal along the direction of the beam rather than perpendicular to it as illustrated in figure 3.1 (b). This has the big advantage that the metal can be made thick enough to attenuate the photon beam almost completely. Together with the interspersed active medium, which allows the creation of a recordable signal, this increases the detector efficiency tremendously. A detector based on this idea could be regarded as a binary system. The first component is a converter that produces

high-energy electrons through interactions of the incoming photons and the other one is the interspersed active medium where the high-energy electrons deposit their energy. A potential drawback of this design might be the scattered photons originating from the Compton events. Unlike the conventional design, the scattered photons have a higher probability to interact in the detector again and thus contributing to the crosstalk because of the increased length of the detector in beam direction.

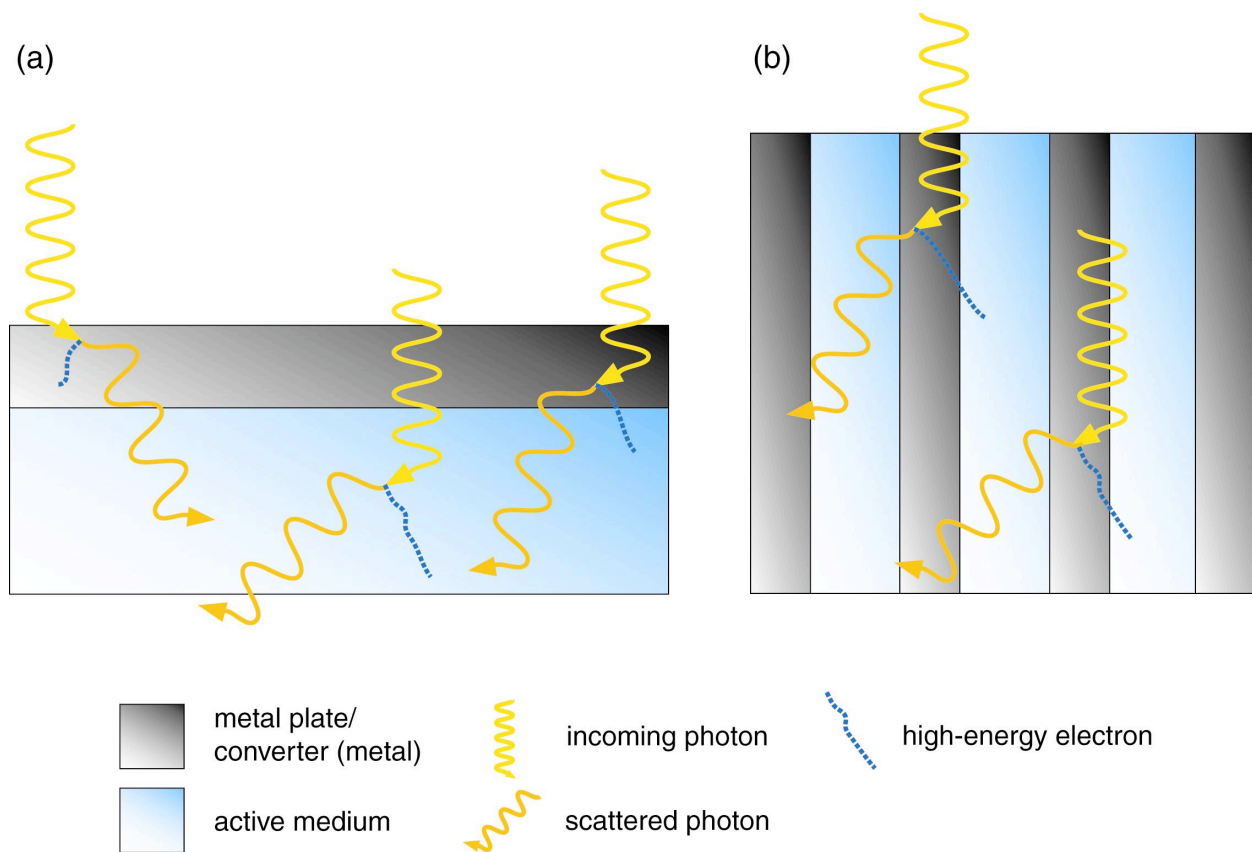


Figure 3.1 (a) Common design of MV photon detectors currently employed in radiation therapy. A front metal plate is used to increase the detection efficiency. Incoming photons interact in the metal and produce high-energy electrons that deposit their energy in the

Figure 3.1 (b) Investigated design of a more efficient MV photon detector. The converter material (metal) is placed along the direction of the beam rather than perpendicular to it. Thus the converter can be made thick enough to attenuate the photon beam almost

active medium. A certain fraction of the photons directly interacts in the active medium. This design, however, is inherently inefficient since only a small part of the incoming photons interacts in the detector due to its limited thickness. This increases the detector efficiency tremendously. The interspersed active medium allows the creation of a recordable signal. The scattered photons, however, contribute to the crosstalk.

There are many possible embodiments of such a binary system. The converter material of choice is a metal with a sufficiently high physical density and atomic number to maximize the number of interactions of the MV x-rays and to minimize the crosstalk among the detector elements. At the same time the converter material, which surrounds the active medium, is supposed to define the detector element. A multirow or area detector would consist of a regular two-dimensional array of such elements. The active medium, on the other hand, must be able to convert the energy deposited by the high-energy charged particles into a recordable signal. There is a large variety of possible active media available including scintillators that transform the energy into ultraviolet or visible photons. Subsequently, these photons can either directly be detected by photosensitive detectors (Antonuk *et al.* 1991b, Yaffe and Rowlands 1997) or they can be transmitted via optical fibers to photodetectors that are located outside the direct beam of radiation (Yaffe 1993). Another possibility for the active medium are semiconductors like selenium (Boag 1973, Zhao and Rowlands 1995). In these materials the deposited energy is converted into electron-hole pairs that are separated and collected by an applied electrical field. A similar approach employs a gas rather than a solid active medium. In this case the high-energy electrons create ionization charges in the gas that are, once again, separated by an electrical field. Unlike solid active media, high-energy photons rarely directly interact in the gas.

The work presented focuses on gas as the active medium. This embodiment is based on the principle of an ionization chamber, which represents a mature and relatively simple technology. It also offers the advantage of resistance to radiation damage. In addition, the prediction of the signal is straightforward since it is reasonable to assume that the signal is proportional to the amount of deposited energy in the gas (Hinderer *et al.* 2002a).

Other active media like amorphous selenium or scintillators are much more demanding in terms of engineering. In principal, scintillation based detectors should be more efficient than gas ionization based systems since more photons directly interact in the active medium. Scintillation based systems, however, often suffer from a low light collection efficiency (Munro *et al.* 1990, Wirrwar *et al.* 1999).

3.2 Xenon gas ionization CT detector

3.2.1 Structure of the detector

As discussed in the introduction, the helical tomotherapy unit employs a 738-channel General Electric single row xenon gas ionization CT detector. Figure 3.2 shows the structure of the detector. A detector element, also called a channel, is confined by two tungsten plates that are kept at a high voltage. The space in between is filled with xenon gas at a pressure of 25 atm. In the center of the element is a third tungsten plate, which serves as the collecting plate. It is kept at floating ground. The center-to-center distance of two adjacent elements is 1.28 mm. The

738 channels are arranged along an arc, which is focused towards the x-ray source. As the system is a single row detector, only one slice image can be acquired at a time.

An integral part of this CT detector is the data acquisition system (DAS). The DAS measures the continuous, low-level currents coming from the detector elements. It conditions and digitizes the currents and transfers them to a host computer. A microprocessor controls the setup conditions and operating modes of the DAS. The microprocessor, in turn, is controlled by the host computer.

The employed DAS (General Electric 1988) is a filter-type DAS that is able to handle the signals from the 738 detector elements. Each signal is filtered by a 3-pole Butterworth lowpass filter to eliminate the high-frequency noise from the low-level input signals. Subsequently, the signal current is converted to a voltage, which can be processed by the analog-to-digital converter (ADC). The ADC provides the digital output of the DAS. It samples the temporally varying voltage at regular intervals. To avoid aliasing, only those frequencies are retained by an analog filter that are below the Nyquist frequency (equal to half of the ADC sampling frequency). Note, that this ADC sampling has no relationship to the spatial sampling of the image by the detector elements.

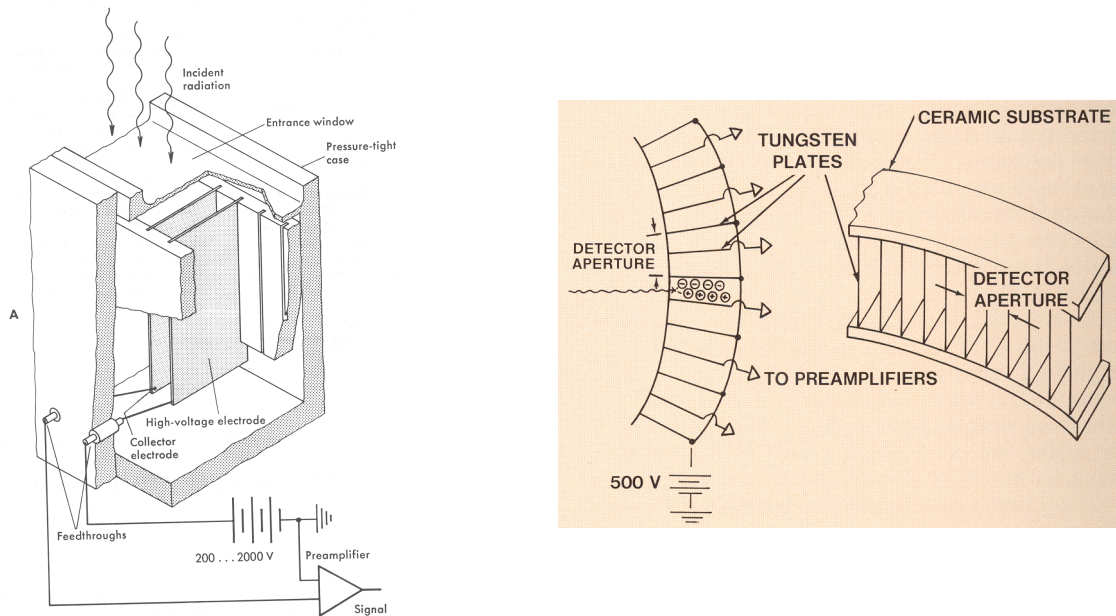


Figure 3.2 Structure of the single row xenon gas ionization CT detector employed by the helical tomotherapy unit. A detector element is confined by two tungsten plates, which are kept at a high voltage. The space in between is filled with xenon gas at a pressure of 25 atm. In the center of the element is a third tungsten plate that is used as the collecting plate. The collected charges from this plate are transferred to a preamplifier. The plates are held in place and insulated against each other by two ceramic substrates. The center-to-center distance of two adjacent elements is 1.28 mm. 738 of such detector elements are arranged along an arc in a pressure-tight case. The arc is focused towards the x-ray source (from Ref. (Peschmann 1981) (left) and (General Electric) (right)).

This xenon gas ionization detector was originally designed for kVCT applications (Peschmann 1981, Yaffe *et al.* 1977). Intriguingly, it proved to be an excellent detector for megavoltage photons. When figure 3.2 is compared with figure 3.1 b), it is obvious that this CT detector is an example of the proposed design of an efficient detector for megavoltage x-rays. Although the detector can be used for the detection of kilovoltage as well as of megavoltage x-rays, the principle of signal generation is quite different for the two cases as indicated in table 3.1. The different mechanisms of signal generation have important consequences with respect to the alignment of the detector.

Table 3.1 Table 3.1 contrasts the difference of the xenon gas ionization CT detector, when it is employed for the detection of kilovoltage x-rays and megavoltage x-rays, respectively.

	kilovoltage x-rays	megavoltage x-rays
principle of signal generation	<p><i>xenon gas</i></p> <p>Most of the x-rays interact in the pressurized gas in photoelectric and Compton events. The electrons produced in these interactions deposit their energy in the gas.</p> <p><i>gas pressure</i></p> <p>Up to a certain point, a higher gas pressure increases the photon attenuation, and thus the signal, exponentially. Not only the signal increases with pressure but also the DQE.</p> <p><i>tungsten plates</i></p> <p>When x-rays hit a tungsten plate, the photons get absorbed without the generation of a recordable signal. Electrons created in interactions in the metal do usually not have sufficient energy to reach the gas cavity. In general, the plates confine the elements and minimize the extent of the crosstalk. In addition, they serve as an inherent collimation so that the detection of scattered radiation coming from the patient is minimized.</p>	<p>Only a small fraction of the x-rays directly interacts in the gas. The gas, however, is the medium where the signal is ultimately generated.</p> <p>A higher gas pressure increases the detector efficiency only marginally. Up to a certain point, the recorded signal, however, increases proportionally to the pressure (Hinderer <i>et al.</i> 2002b). In general, larger signals can be read out more accurately and at a lower cost (Gordon 1981).</p> <p>Most of the x-rays interact in the tungsten plates due to their high density and high atomic number. The dominating Compton events result in the production of electrons. These electrons usually have enough energy to reach the gas cavity where they deposit their energy. Besides the conversion of x-rays into high-energy electrons, the tungsten plates confine the elements and minimize the extent of the crosstalk.</p>
alignment of detector	<p>The alignment of the detector is critical. The arc must be focused towards the x-ray source so that the photons can travel parallel to the tungsten plates. Even a small misalignment results in the absorption of the x-rays by the tungsten plates.</p>	<p>The detector does not have to be aligned with respect to the x-ray source. If the detector was not focused towards the x-ray source, the detection efficiency would even increase (Keller <i>et al.</i> 2002). In an out-of-focus arrangement a larger fraction of the photons have to travel through tungsten. In an <i>in focus arrangement, on the other hand, fewer</i></p>

in-focus arrangement, on the other hand, fewer photons travel through metal.

3.3 Prototype detectors

The high DQE(0) value together with the reported MVCT images of the xenon gas ionization CT detector encouraged the development of the first prototype detectors based on the same principle of megavoltage photon detection and imaging using the binary system approach introduced in chapter 3.1. The first few prototype detectors consisted of just a single detector element. Then small single row prototypes and finally a 4x4 element detector were developed and tested.

3.3.1 Single element prototype detectors

3.3.1.1 Structure of the prototype detectors

The purpose of the first few prototype detectors was to prove the usefulness and feasibility of the presented novel concept of megavoltage photon detection. The first prototypes consisted of a single detector element in form of a hollow brass tube. Brass was chosen as the converter material since it is easily machinable, low in expense and it has a relatively high density of about 8.5 g/cm^3 . The tubes were filled with pressurized xenon gas. Xenon is an inert noble gas with a high density and consequently a high electron collision stopping power.

Four different kinds of brass tubes were evaluated. As shown in figure 3.3, they were mounted on a rack to allow for concurrent measurements. They were spatially separated to minimize their mutual interference. While the tube with the rectangular (A) cross section used a

collecting bar (a), the tubes with a square (B), hexagonal (C) and round (D) cross section employed a collecting wire (b). These collecting structures were placed inside the tubes where they span the whole length of it. Also, the cross section of the three latter tubes was about half as large as the one of the rectangular tube. The rectangular tube had outer dimensions of 2.38 mm by 4.76 mm and a wall thickness of 0.36 mm. The wall thickness was the same for all tubes. The resolution in the plane of the detector is largely given by the outer dimensions/periodicity of the tubes. The tube length of 6 cm corresponds to an attenuation of the photon beam of about 93% for a 4 MV linear accelerator spectrum. This number is based on the mean free path length in brass for this polyenergetic beam provided by a Monte Carlo simulation. While the collecting bar had the dimensions of 0.38 mm by 3.00 mm the diameter of the collecting wire was around 0.51 mm. Printed circuit boards, that were a part of the rack, allowed a precise centering of the collecting electrodes. To prevent bending of the tubes and the collecting structures, the detectors were fixed to the rack at both ends. The whole assembly was immersed into a gas within a pressure vessel. Vent holes allowed the diffusion of the gas into the tubes. Finally, a high voltage was applied across the tubes and the collecting electrodes.

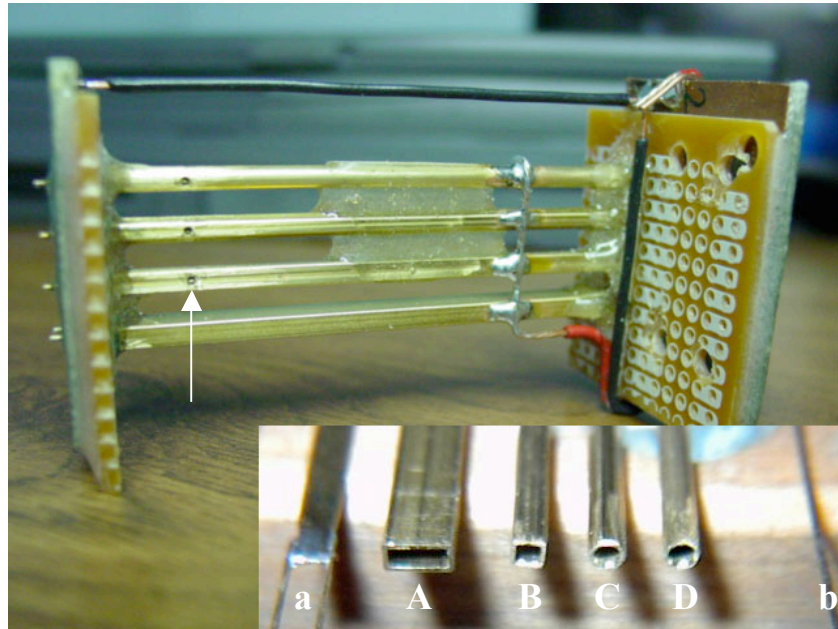


Figure 3.3 The single element prototype detector consisted of a hollow brass tube. Four different kinds of brass tubes were evaluated. They were mounted on a rack (to make a concurrent testing feasible) and subsequently immersed into a gas within a pressure vessel. The MV photons come from the left and travel along the tubes. The inset shows the tubes with a rectangular (A), square (B), hexagonal (C) and round (D) cross section. While the rectangular tube employed a collecting bar ((a); the two attached wires helped to center it), the other ones used a collecting wire (b). The arrow indicates the vent holes.

Proper guarding of each tube is a critical issue. When two pieces of metal, exhibiting a high potential difference, are separated by an insulator, a leakage current can flow. This current flows across as well as along the surface of the insulator. A leakage current can significantly alter the signal read out. To prevent its flow, a grounded sheet of metal, serving as the so-called guard electrode, can be put, together with the insulator, in between the two pieces of metal. Figure 3.4 shows the guarding chosen for the brass tubes. Two printed circuit boards were put together with their copper coated sides touching each other. This copper coat was put at ground potential. Consequently, there is no electrical field and thus no current between the copper and the

collecting wire, which is on floating ground. An eventual current can only flow between the copper and the brass tube.

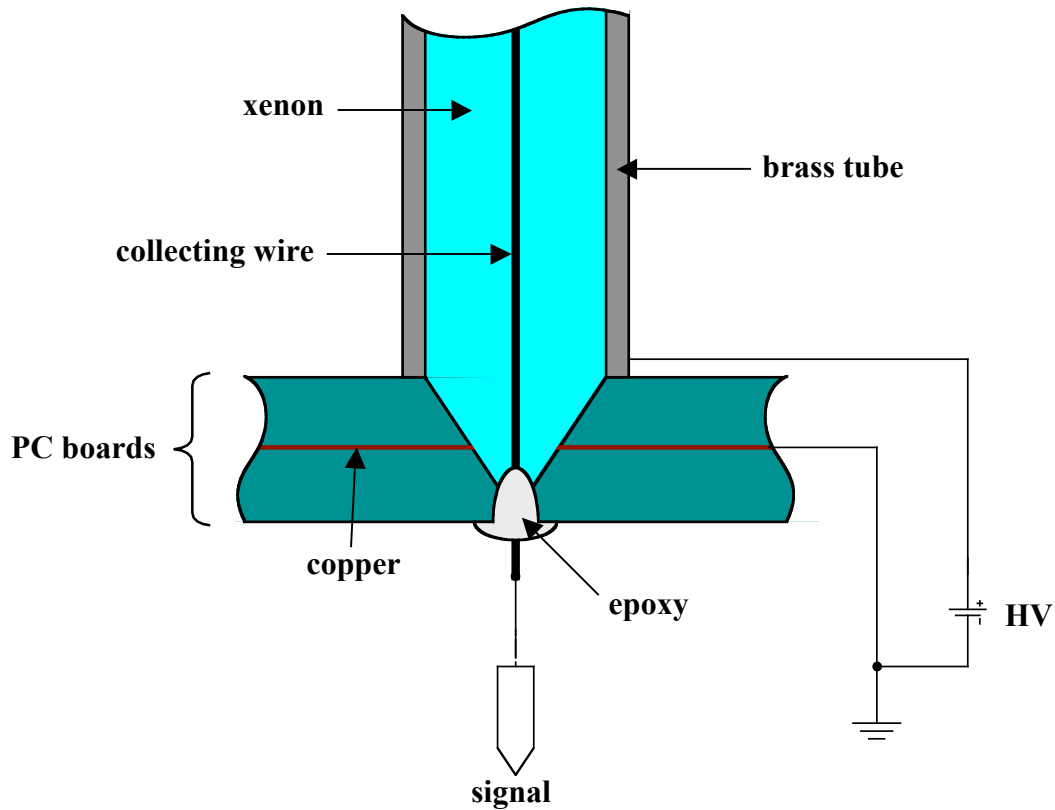


Figure 3.4 Schematic drawing illustrating the principle of guarding of the brass tubes. Two pieces of printed circuit (PC) boards were put together with their copper coated sides touching each other. This layer of copper was put on ground. Therefore, the flow of a leakage current between the collecting wire, which was on floating ground, and the brass tube, which was on a high positive potential, was prevented.

3.3.1.2 Experimental setup

To take data with a pressurized gas, the rack with the prototype detectors was placed inside a pressure vessel, which can hold pressures of up to 7 atm. The vessel's entrance wall was made of aluminum and was about 1.5 cm thick resulting in an attenuation of the incoming beam by

roughly 20%. An external power supply provided the high voltage required for the detectors. To minimize the amount of noise and the influence of electromagnetic stray fields, the detector signals were relayed by a specially shielded and grounded ribbon cable to a data acquisition system. This DAS is the same as the one employed for the General Electric single row xenon gas ionization CT detector. The DAS is an essential part of the University of Wisconsin - Madison tomotherapy benchtop. All data is transferred from the DAS to a computer allowing the remote and automated control of the prototype detectors. The center of the tubes was 145 cm away from the target of the linac to simulate the geometry of a clinical tomotherapy unit. The linac used is a General Electric Orion (Buc, France) accelerator with a nominal energy of 4 MV and an average energy of about 1.36 MeV. For the phantom measurements, an actuator centered at the isocenter (93 cm away from the target) was used. It allows a translation, vertical movement and rotation of the phantom. This setup results in a magnification of about 1.56, i.e. the resolution in the object plane is 1.56 times finer than in the detector plane. Two important features of this system facilitate the readout of the detectors after each linac pulse – the speed of the detectors themselves and the synchronization of the DAS with the linac. Figure 3.5 shows the experimental setup.

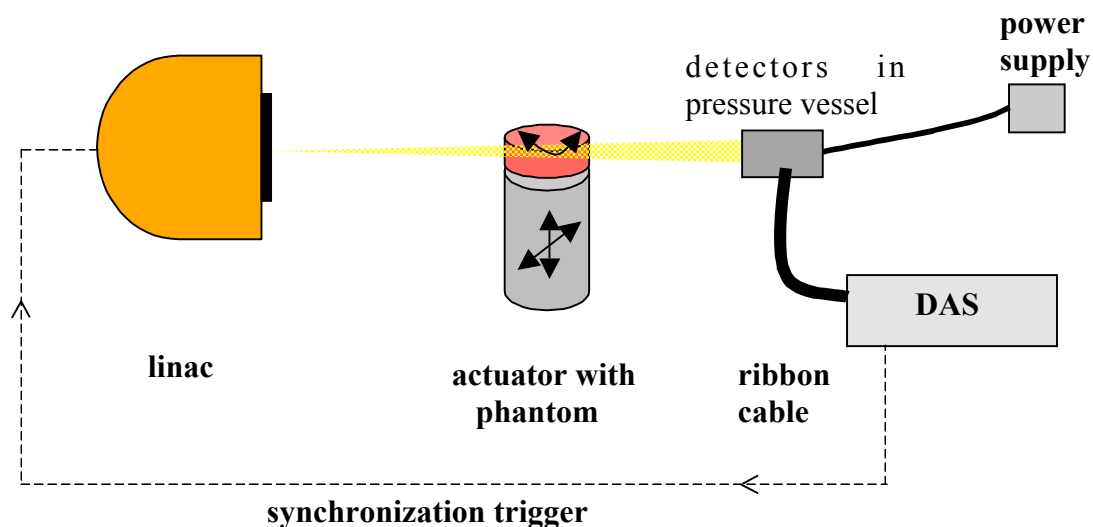


Figure 3.5 Schematic drawing of the experimental setup for the characterization of the single element prototype detectors that were placed inside a pressure vessel. A power supply provided the required high voltage for the detectors. The signals were recorded by a data acquisition system (DAS) via a ribbon cable. The data recording was synchronized with the linac using the indicated linac pulse trigger. In case of phantom studies, a phantom was placed on an actuator in between the linac and the detectors.

A larger scale detector would essentially employ the same setup. The main components are a sufficiently large pressure vessel with feedthroughs for the signal carrying wires and a DAS. The DAS must be able to handle concurrently the signal from many detector elements. The employed DAS was designed to read out 738 elements. Multiple DAS can be used to read out even more elements.

3.3.1.3 Measurements

3.3.1.3.1 Conversion of the DAS/digital units into absolute charge readings per linac pulse

The DAS maps the measured signal of a detector element to a digital output scale ranging from 0 to 2^{20} DAS/digital units. To convert the DAS units into absolute charge values, the signal current of the rectangular tube was directly measured with a calibrated electrometer (Keithley, Cleveland, OH). The reading was corrected for leakage. In another measurement, the signal of the rectangular tube was recorded by the DAS. The signal was averaged over 2000 linac pulses. Readout of the DAS with the linac beam off, allowed the determination of the background signal that was subtracted from the DAS reading. To allow for a comparison, both values were normalized to the same linac output level. Based on the conversion factor

$$\text{conversion factor} = \frac{\text{measured current}}{\text{linac frequency} \cdot \text{DAS reading}}, \quad (3.1)$$

the DAS reading can be converted into an absolute charge per linac pulse reading, where the pulse repetition frequency of the linac was 200 Hz.

3.3.1.3.2 Saturation curves

To determine a suitable voltage across the tube and the collecting electrode, the signal of the tubes was measured as a function of the applied voltage. In addition, these measurements allow a quantitative comparison of the signal of the different kinds of tubes. As the DAS can handle only negatively biased collecting electrodes, positively charged gas ions are collected. Measurements were done for the rectangular and hexagonal tube in 6 atm of air and for the rectangular, hexagonal and square tube in 6 atm of xenon. The data from the DAS was processed by subtracting the background signal and by correcting for the varying linac output. This DAS data processing was done for all further measurements. In addition, the leakage current, which increases linearly with the applied voltage, was subtracted. Finally, the readings were averaged over several thousand linac pulses to get the average charge per linac pulse at a given voltage.

3.3.1.3.3 Detector signal as a function of the gas pressure and gas type

Measurements with air and xenon, respectively, at different pressures ranging from 1 atm to 6 atm allow a further characterization of the prototype detectors. Similar to an ionization chamber, the signal is expected to rise linearly with pressure. Any nonzero y-intercept indicates an induced signal due to electromagnetic stray fields and megavoltage x-ray radiation induced signals in the cables and connectors used for the readout. These y-intercepts were determined

and used to approximate the induced signal. The induced signal was subtracted from each measured data point assuming that it is independent of the gas pressure. Finally, a comparison of the signal measured in air and xenon at a given pressure provides further insight and permits a comparison with theoretically predicted values.

3.3.1.3.4 Megavoltage CT images of a contrast phantom

So far only characteristics of the detectors themselves were investigated but the ultimate goal is the evaluation of the imaging capability with megavoltage photons. One of the most critical quantities in assessing the quality of megavoltage photon images is the contrast resolution. For this purpose, MVCT images of a contrast phantom (CIRS, Norfolk, VA) were acquired with the different kinds of brass tubes at 6 atm of xenon in a fashion consistent with a first generation CT scanner. The phantom contained nine plugs of different contrasts, which are defined in terms of electron densities with respect to water:

$$\% \text{ contrast} = 100 \cdot \frac{\rho_e - \rho_e^w}{\rho_e^w}, \quad (3.2)$$

where ρ_e^w and ρ_e are the electron density of water and the material of interest, respectively. This phantom was placed on the actuator and translated in increments of 2 mm. After each translational step the phantom was rotated by 360 degrees while the transmitted radiation was detected. This process was repeated until the whole phantom was translated across the tubes. Reconstruction of the images requires the subtraction of the background signal and the knowledge of the signal with the linac beam on but with no phantom in place (air scan). The latter signal is used to normalize the measured transmission data. The reconstruction was based

on parallel-ray geometry and used filtered backprojection, where in our case several linac pulses were averaged to yield one projection. The imaging dose was about 27 cGy for the 4 MV linac beam. If the linac beam is collimated down to the size of the detector element, the dose to the phantom would essentially be equal to the imaging dose. The calculation of the dose to the center of the phantom for an axial scan is based on an approach described by Balog (Balog 1998). It estimates the dose to the center of the phantom D_C to within 5% based on the formula

$$D_C = \dot{D}(d_{\max}) \cdot \frac{1 \text{ min}}{60 \text{ s}} \cdot \Delta t \cdot \text{TMR} \cdot \text{scatter estimate} . \quad (3.3)$$

The dose rate \dot{D} is measured at the depth of maximum dose (d_{\max}) and, in this case, is equal to about 200 cGy/min. The rotation period Δt was chosen to be 12 s. TMR designates the tissue maximum ratio. This parameter and the scatter estimate are tabulated in (Balog 1998) for different depths in the phantom.

3.3.2 Multielement prototype detectors

Based on the experience and findings of the single element prototype detectors, the first multi-element prototype detectors were built and investigated. Several single row systems with just a few elements were constructed. Finally, a 4x4 element detector was built. These detectors were experimentally evaluated using a setup similar to the one shown in figure 3.5. Monte Carlo simulations provided additional insight. The problems associated with the transition to a multielement system were also analyzed.

3.3.2.1 Single row prototype detectors

The first built single row prototype detector had five elements. Each element consisted of a triangular shaped aluminum high voltage (HV) electrode and a steel shim. The HV electrode was formed from a 254 μm thick Al sheet. A bending of the sheet at right angles is problematic at this scale. Thus, a triangular shaped electrode structure was chosen. As shown in figure 3.6, the HV electrode was kept in place with two Al spacers. The 127 μm thick steel shims served as the collecting electrodes. They were embedded in an epoxy base. The detector pitch was 1.45 mm. To ensure a sufficient attenuation of the photon beam, the length of the detector along the beam axis, including the shims and HV electrode, was 42 mm. Only the three inner elements were used for read out. The shims in the outer elements served as guard electrodes to minimize any leakage current flowing between the HV electrode and the collecting electrodes. The elements were read out with an electrometer one at a time. The charge reading for a certain amount of time of irradiation was used as a measure for the signal. Similar to the previous measurements, the data was corrected for varying linac output as well as for any leakage current. All measurements were done in air at atmospheric pressure. The voltage applied across the electrodes was 110 V. Several measurements were performed using the 4 MV Orion linac to characterize the detector. For the following measurements, the detector signal is represented as the accumulated charge for an irradiation of 100 monitor units (MU).

To evaluate the response of the detector to different beam field sizes, the three elements were read out for different field widths. In vertical direction the field size was kept constant at 12 mm so that it just covered the height of the elements. This minimizes the signal generation in any other part of the detector.

Another measurement addressed the issue of the alignment of the detector with respect to the photon beam. To determine the angular sensitivity of the signal of the central element (element c; see figure 3.6 for an explanation of the element labeling), the detector was rotated about its vertical axis in angular increments as indicated in figure 3.6 (a). For the 0 degree position, the shims and the walls of the detector elements were aligned with respect to an adjusted laser beam, which indicated the photon beam axis. The chosen field size of $10 \times 5 \text{ cm}^2$ encompassed the whole detector at all angular positions.

To investigate the significance of the material of the HV electrode, HV electrodes made of aluminum, copper, lead and tantalum were fabricated and tested. The investigations focused on the practicality of using the different metals.

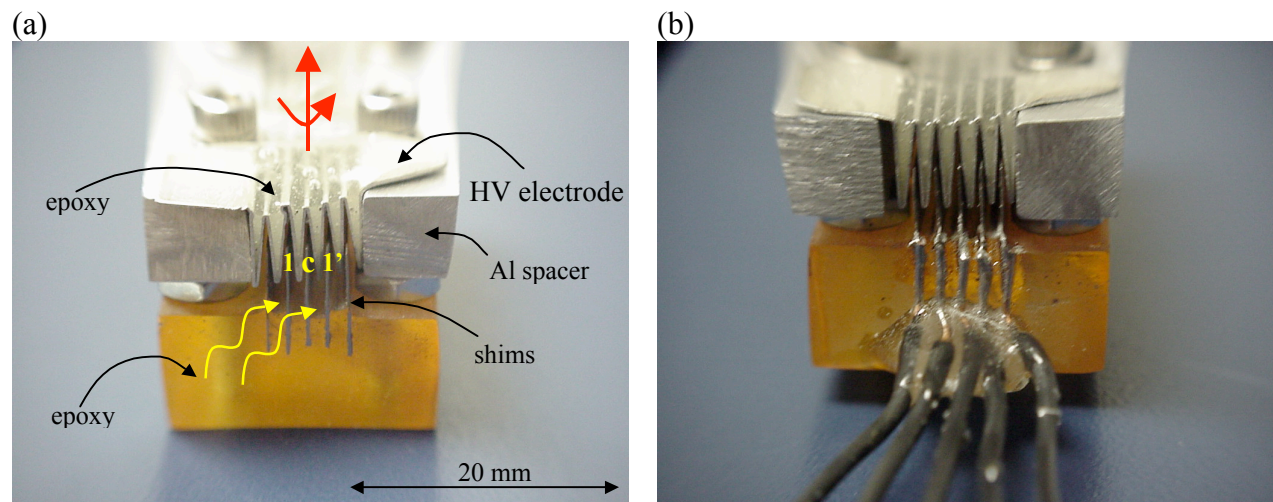


Figure 3.6 First built single row prototype detector. (a) Front view: Each element consists of a triangular shaped aluminum HV electrode and a steel shim, which serves as the collecting electrode. The upper grooves of the HV electrode were filled with epoxy to mechanically stabilize the structure. Only the inner three elements were used for read out. The labels c, 1 and 1' designate the central element and the two adjacent elements. The shims in the outer elements served as guard electrodes. In one experiment, the detector was rotated about its vertical axis as indicated, to evaluate the angular sensitivity of the detector signal. (b) Rear view: Each shim was connected to a cable to read out the signal and to guard the electrode, respectively.

Based on the experience with the previous detector, a more advanced prototype was built and tested. The detector distinguished itself as more reliable and rugged. The HV electrode consisted of a block of aluminum with seven regular 1.02 mm wide rectangular notches, which formed the elements of the detector. This electrode rested on the same piece of epoxy with the immersed steel shims as it was used for the previous prototype detector. Figure 3.7 shows a drawing of the front view of the detector. This design results in a more uniform response of the different detector elements. In addition, problems with short-circuits due to shims that are in contact with the HV electrode are minimized. A voltage of 110 V was put across the electrodes. As for the previous single row prototype detector, the outermost steel shims served as guard electrodes. The leakage current was on the order of a few pA and negligible in comparison to the signal current, which was usually on the order of a few nA.

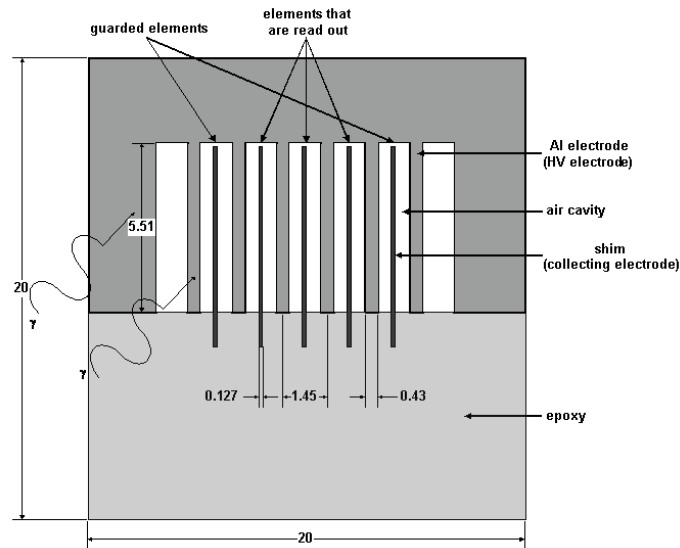


Figure 3.7 Front view of the more advanced single row prototype detector. The HV electrode, made of aluminum, forms uniform elements. It rests on the same epoxy base with the immersed steel shims as it was used for the previous prototype detector. This design results in a more uniform response of the individual elements. In addition, problems with short-circuits due to shims that are in contact with the HV electrode are minimized. The detector extends 42 mm into the paper plane (all dimensions are in mm).

To characterize this detector, measurements similar to the ones with the previous prototype, were taken. In addition, the charge per collecting gas volume of element c (see figure 3.8 for an explanation of the element labeling) was compared with that of a Farmer ionization chamber (Exradin, model A12, Standard Imaging, Middleton, WI) positioned at the depth of maximum dose (d_{\max}). Farmer chambers are commonly employed in radiation therapy for the purpose of dosimetry. The measurement is intended to illustrate the significance of the metal surrounding the gas cavity as well as of the shims in regard to the signal generation. Both detectors were placed at the isocenter of the linac and irradiated under the same conditions. The field size was $10 \times 5 \text{ cm}^2$. Once again, the accumulated charge for an irradiation of 100 MU was measured.

To better understand the signal formation, Monte Carlo simulations were performed on the real detector geometry. Ultimately, such simulations can help to optimize the detector geometry. For this purpose, the MCNP 4C Monte Carlo code (Briesmeister (ed) 1997) was employed. The photon source was modeled as a point isotropic source with the energy spectrum of the Orion accelerator. This spectrum was derived from Monte Carlo simulations modeling the whole treatment head of the linac (Glass). It was assumed that the deposited energy in the air cavity is proportional to the detected signal. This is a reasonable assumption for ionization-type detectors (Hinderer et al. 2002a). Figure 3.8 shows a diagram of the modeled geometry.

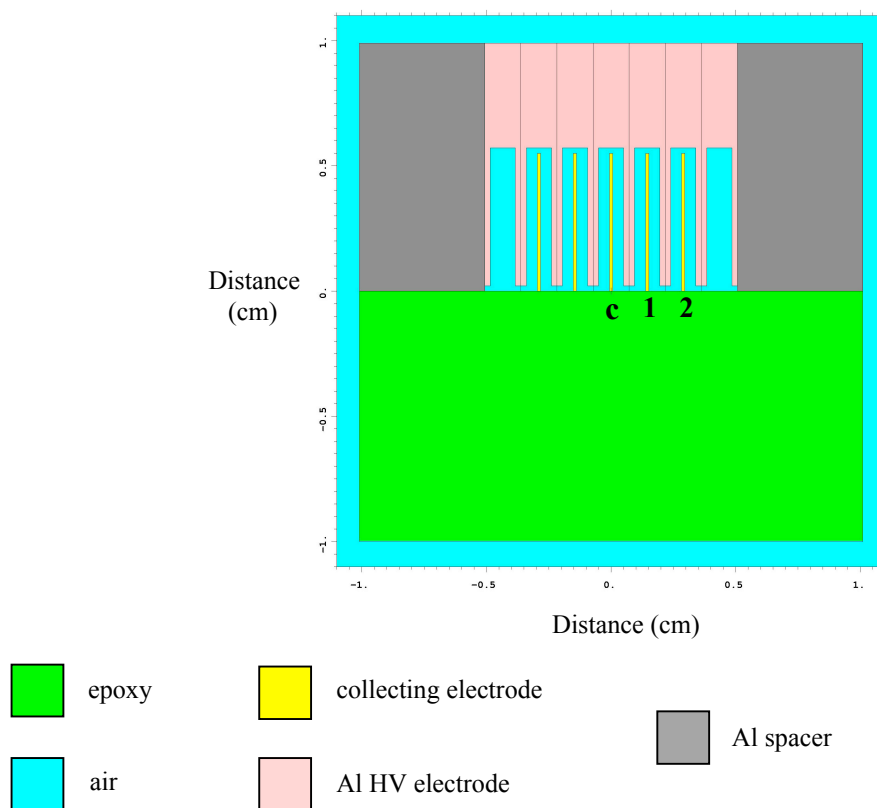


Figure 3.8 Illustration of the detector geometry as it was modeled for the Monte Carlo simulations. This model is based on figure 3.7. The labels c, 1 and 2 designate the elements whose signal was scored. Among others, this model was used to define the components of the detector whose contributions to the signal of the elements was

scored. Note that the walls of the elements, formed by the grooved part of the HV electrode, do not touch the epoxy base to prevent the flow of any leakage current.

At first, the contributions of the different components of the detector to the deposited energy in the gas of the elements c, 1 and 2 was investigated. For this purpose, the detector was decomposed into the components HV electrode, shims, epoxy, Al spacer and air as indicated in figure 3.8. The contributions were estimated by adding the individual components one-by-one starting with just air. For each step, the deposited energy was scored in the same volumes, namely the gas cavities of the elements. For the simulations, an air pressure of 1 atm was assumed. As for the measurements, the distance between the modeled point source and the front face of the detector was 91.0 cm. The source formed a cone beam with a full opening angle of about 3.8 degrees. This ensures that the whole detector is well within the beam.

The thickness of the wall of the elements, formed by the grooved part of the HV electrode, is of great interest in regard to the signal generation. To investigate this issue, the thickness of the wall was varied while the detector pitch was kept constant. The signal of an element was scored separately in the elements c, 1 and 2 using the previously mentioned cone beam. In addition, the signal per gas volume was determined for the element c for the different wall thicknesses. To get additional information about the primary signal, scored in the element c, and about the crosstalk, scored in the elements 1 and 2, a narrow beam was employed in another simulation. The beam covered exactly the central element, which ranges from the midline of the wall of one electrode to the midline of the other electrode wall. In the vertical direction the beam covered the whole HV electrode.

To study the importance of the HV electrode material in regard to the primary signal and the crosstalk, the above calculations were repeated for copper and tungsten for the same wall thicknesses.

Finally, the same narrow beam was employed to investigate the influence of an Al sheet, which was placed directly in front of the detector, on the scored signal. Such a sheet might serve as a build-up material provided that an appropriate thickness is chosen.

3.3.2.2 4x4 element prototype detector

The next step in the development of an efficient detector system for megavoltage photons was the transition from a single row detector to a multirow/area detector. Figure 3.9 shows the first prototype of this kind. This detector, consisting of 4x4 elements, was built and tested.

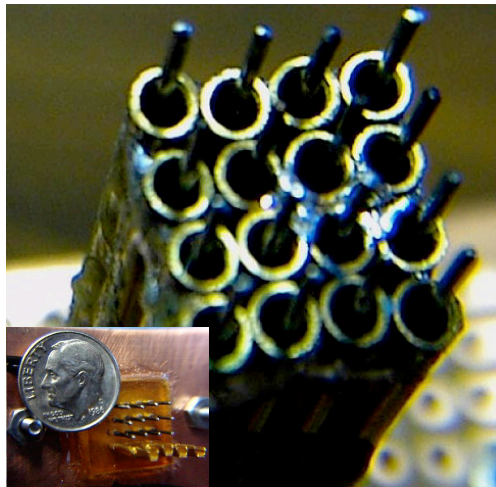


Figure 3.9 4x4 element prototype. Each element consists of a hollow brass tube with a carefully centered collecting wire in it. The tubes have an outer diameter of 2.38 mm, a wall thickness of 0.36 mm and a center-to-center spacing of 2.54 mm. The collecting steel wire has a diameter of 0.64 mm. The inset shows the rear view of the detector with the collecting wires kept in place by an epoxy base. These wires were directly connected to a ribbon cable, which was used to read out the detector elements.

3.4 Monte Carlo-based characterization of a multirow/area detector model

Before larger prototype detectors can be built, a careful investigation of the design is required. Monte Carlo studies of a given design prior to the manufacturing process can save time and reduce the costs. In addition, Monte Carlo simulations can provide insight into basic physical processes of the detector, which are not easily experimentally or analytically accessible. The preliminary studies of the single row prototype detector already illustrated the power of Monte Carlo simulations. These simulations were extended to a multirow/area detector model. The simulations of the prototype detector indicated the enormous significance of the wall thickness and material. Thus, the primary signal, recorded by the irradiated element, as well as the total amount of crosstalk, recorded by all other elements, were scored for the multirow/area detector model for a range of wall thicknesses and for the materials brass and tungsten. Moreover, the total signal, recorded by an element in case of a broad beam irradiation, was determined. A similar approach is employed to study the significance of the collecting wire and the length of the detector in beam direction.

Although important conclusions can be drawn from these simulations, they do not allow a comprehensive treatment of the problem. For instance, not only the total amount of crosstalk is of importance but also its spatial distribution. Crosstalk with a broad distribution has different consequences than crosstalk that concentrates around the irradiated element. A quantity, which quantifies the efficiency and performance of a given detector design, is required. The $DQE(f)$ is the single best quantity to do this (Metz et al. 1995). As it is a function of the spatial frequency,

it takes into account any spatially varying effects such as the amount of crosstalk. The determination of the $DQE(f)$ requires the knowledge of the MTF and NPS. Particularly, the determination of the MTF of a digital x-ray detector with a severely inhomogeneous detection medium, however, has never been investigated in detail. Thus, a large part of this chapter deals with the determination of the MTF of such detectors. The implementation of three different approaches was investigated and their results were compared. Finally, the determination of the digital NPS is sketched.

3.4.1 Primary signal, total amount of crosstalk and total signal

The Monte Carlo simulations in this part are based on a detector model consisting of an array of rectangular elements as shown in figure 3.10. There are two collecting wires in each cavity. The usage of two wires increases the charge collection efficiency. Alternatively, a collecting bar could be employed. However, there might be some manufacturing issues. A bar would require a rectangular slot for fixation, which is usually not easily machined.

The rectangular structure has several advantages. Unlike an array of tubes, the whole volume is utilized for signal generation and detection. In addition, this kind of geometry is relatively easily manufactured. One possibility is the assembly of sheets of metal with appropriate grooves cut, for instance, with lithography. In principle, the rectangular element can be broken up into two square elements. This would result in a uniform response and resolution in both directions. Rectangular elements, however, exhibit a signal that is about twice as large. As the measurements with the brass tubes with different cross sections indicated, the magnitude of the signal is of concern. A higher signal usually means a more accurate and simpler read out, a

higher signal-to-electronic (induced) noise ratio and a larger dynamic range. These points illustrate why the measurements with the rectangular tube were most accurate and most easily performed. Moreover, the larger element size reduces the number of required elements to cover a certain area.

The rectangular nature of the detector, though, has consequences on the spatial resolution. For instance for MVCT, the resolution in z -direction (cf. figure 3.10), corresponding to the slice thickness, is compromised. The spatial resolution in x/y -direction, corresponding to the slice image plane, is roughly twice as large as in the z -direction. This is common practice in the field of computed tomography and does not necessarily impose any limitations (Kalender 2000).

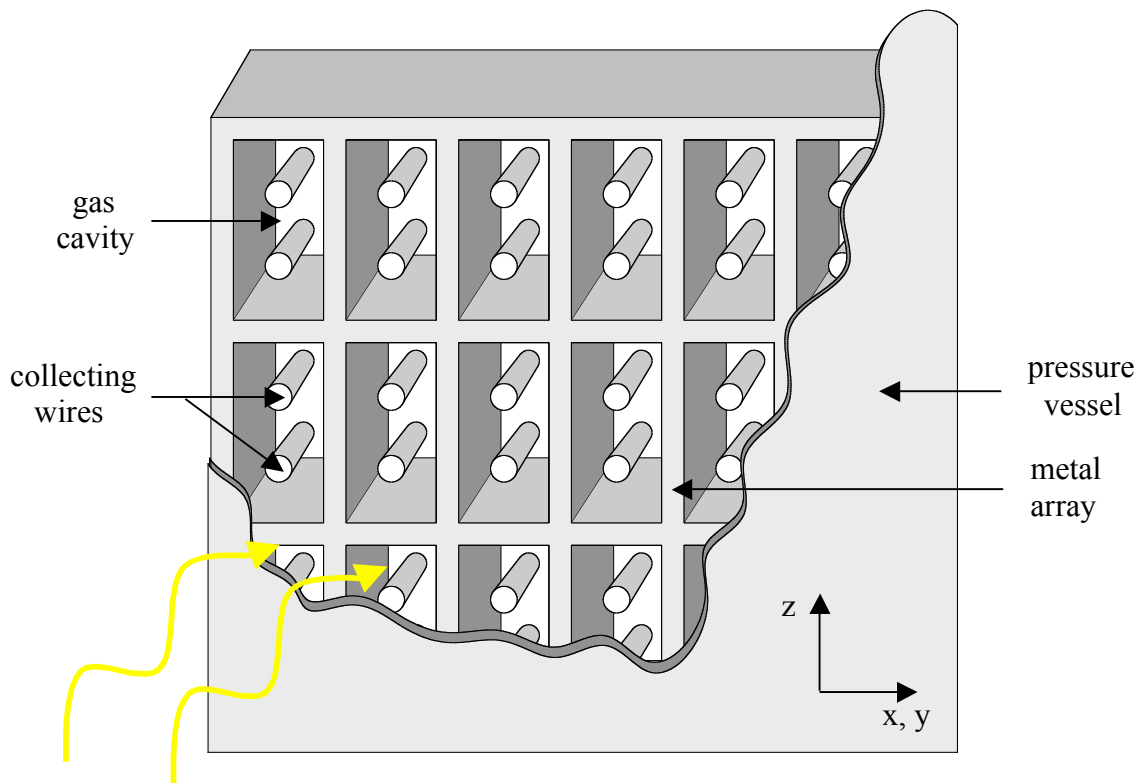


Figure 3.10 Detector model used for the Monte Carlo simulations in this subchapter (For simplicity, the pressure vessel was not considered for the simulations). It consists of an array of rectangular elements and two collecting

wires in each xenon gas cavity. To ensure a sufficiently large detector signal for a given spatial resolution, rectangular elements were chosen rather than square ones. In MVCT, this results in a better resolution in the slice plane (the x/y-plane) than in the z-direction (corresponding to the slice thickness). See text for more details on the dimensions of the detector.

The modeled detector array consisted of brass (Cu: 61.75%, Zn: 34.8%, Pb: 3.1%, Fe: 0.35%). The collecting wires were composed of steel (iron) and the cavities were filled with xenon gas at a pressure of 6 atm. The element size was $1.6 \times 3.2 \times 60 \text{ mm}^3$. In general, a wall thickness of 250 μm was chosen. Depending on the kind of simulation, an array of at least 21×21 elements was modeled. This takes into account that the recorded signal decreases rapidly with increasing distance from the irradiated point (element).

Again, the Monte Carlo code used for the presented work was MCNP 4C. For all simulations the deposited energy in the gas of the elements was scored as a measure of the signal. The cutoff energy, chosen for the photons as well as the electrons, was 20 keV to speed up the calculations. Simulations at lower cutoff energies like 10 keV did not reveal any statistically significant differences. Two different linac photon energy spectra were employed for the simulations. The first one matches the spectrum of the 4 MV UW tomotherapy benchtop linac, which was already employed in previous simulations. The other spectrum represents the 6 MV linac from the first tomotherapy machine at the UW hospital with an average energy of about 1.8 MeV (Jeraj). Although this spectrum is obsolete due to a later tuning of the linac, the principal conclusions drawn from the obtained results should not be very different. Above all, the main idea of these simulations is to have a realistic spectrum with a higher average energy than the benchtop unit. If not indicated elsewhere, the 4 MV photon spectrum was used. The lower energy seems to be more appropriate for imaging due to the lower associated dose at a given image quality. All

simulations in this part of the thesis were based on a parallel beam geometry. The number of source particles run was chosen in such a way that the statistical error of the scored deposited dose of the irradiated element never exceeded a few percent. Due to the small statistical errors, no error bars were plotted in the diagrams.

3.4.1.1 Separation of the total signal into a primary and crosstalk component

The separation of the total signal into a primary and crosstalk component allows a more detailed characterization of the detector. For this purpose, a beam was employed that covers exactly one detector element. An element is defined to range from the midline of the left wall to the midline of the right wall and equivalently in the perpendicular direction. The irradiated element was located in the center of the array. The chosen beam size is the smallest one, which still employs the periodicity of the detector array. The deposited energy was recorded in all elements. The primary signal is only recorded by the irradiated element whereas the spatial distribution of the crosstalk is recorded by all other elements. It is important to note that the crosstalk signal in a given element is equal to the amount of crosstalk contributed to the element in the center by the given element when it would be irradiated (reciprocity principle). Consequently, the sum of the primary signal and the total amount of crosstalk amounts to the total signal recorded by the central element in the case of a broad beam irradiation. A broad beam is defined to cover many elements. An array with a suitable wall thickness would be characterized by a high primary signal since the amount of deposited primary energy is a measure of the efficiency of signal generation and detection. At the same time the total amount of crosstalk should be kept at a minimum. Finally, a high total signal would be advantageous for practical reasons. A more detailed study would incorporate the spatial pattern of the crosstalk.

To illustrate this concept, the primary signal as well as the pattern of the crosstalk was determined for a 41x41 element detector array made of brass.

3.4.1.2 Significance of the wall thickness of the detector array

To investigate the significance of the wall thickness of the detector array on the extent of crosstalk and amount of primary energy recorded, arrays with different wall thicknesses were modeled. Unlike the detector model introduced in figure 3.10, an array of square elements with one collecting wire in each element was employed in this section. The length of an element was 5.4 cm. At the time of the simulations the practical advantages of a rectangular element was not obvious yet. However, the kind of geometry will likely not change the principal findings. It should be emphasized that, by definition, a given element contributes one half to the wall thickness while the other half comes from the adjacent element. The width of the square element was held constant at 1.5 mm.

The primary signal, the total amount of crosstalk and the total signal were scored for detector arrays of different wall thicknesses and materials. The investigated materials were brass and tungsten. Tungsten was chosen as an example of a high density and high atomic number material. To ensure a fair comparison, the length of the detector was 5.4 cm for both materials. In practice, however, the length of the detector in beam direction would be chosen in such a way that a sufficiently large fraction of the incoming photons is attenuated. Thus, the length of the detector would depend on the wall material chosen. To evaluate the dependence of the results on the energy spectrum of the linac, the simulations were done for the 4 MV beam as well as for the

6 MV beam. Table 3.2 compares the physical density as well as the atomic number of brass and tungsten.


Table 3.2 Physical density and atomic number of brass and tungsten

metal	density (g/cm ³)	atomic number
brass ¹	8.50	38.9
tungsten	19.25	74

¹ brass is an alloy consisting mainly of copper and zinc; the exact composition (60-63% Cu, 32.05-37.15% Zn, 2.5-3.7% Pb and 0.35% Fe) was taken from the data sheet for the brass tube used for the measurements; the effective Z value was calculated for Compton interactions (i.e. linear weighting of the atomic numbers)

3.4.1.3 Distribution of the deposited energy in an element along the direction of the beam

Another design parameter of interest is the length of the detector array in beam direction. For a better understanding, the amount of primary energy as well as the amount of crosstalk deposited at different depths of the detector were determined similar to a depth-dose-profile in radiation therapy. For this purpose, the gas in the element was divided into 10 scoring slabs of 0.6 cm thickness, oriented perpendicular to the direction of the beam as shown in figure 3.11. Consequently, each slab provides a value of the deposited energy at the location (depth) of the slab. These simulations were done for the irradiated element (element A) providing information about the behavior of the primary signal as well as for the two elements, which are one and two element widths away from the irradiated element (element B and C, cf. figure 3.11), respectively. The latter two signals are a measure of the behavior of the crosstalk.



scoring
gas slabs

Figure 3.11 Schematic drawing of the geometry used to determine the amount of primary energy as well as the amount of crosstalk deposited at different depths of the detector similar to a depth-dose-profile in radiation therapy. The detector model is the same as the one shown in figure 3.10. Element A is the irradiated element. The crosstalk was scored in the elements B and C. The gas volume was divided into 10 0.6 cm thick scoring slabs oriented perpendicular to the beam. Element A provides information about the distribution of the primary signal along the direction of the beam, whereas elements B and C provide information about the distribution of the crosstalk in the beam direction. This information can be used to find an appropriate length of the detector in beam direction. Although not shown, the simulations were done with the collecting wires in place.

3.4.1.4 Significance of the collecting electrodes

Next, the significance of the collecting electrodes in terms of alteration of the amount of deposited energy was investigated. For this purpose, the primary signal was scored for collecting electrodes of different shapes and dimensions. A detector element without any electrodes was used for reference. Subsequently, a pair of collecting wires, that span the whole length of the detector element, was placed into the cavity. This calculation was repeated for wires of different diameter and finally, for a collecting bar. The kind of collecting electrode also influences the charge collection efficiency. This issue was evaluated qualitatively.

3.4.2 Determination of the presampling MTF

So far, the Monte Carlo-based analysis of the multirow/area detector model allowed to draw important conclusions. To find a suitable detector design, however, a quantity, which quantifies the efficiency and performance of a given design, is required. As already pointed out, this can be accomplished by $DQE(f)$. As a first step towards the determination of the $DQE(f)$, the determination of the $MTF_{pre}(f)$ for the investigated detector design is discussed.

3.4.2.1 Background

In chapter 2 the difficulties associated with undersampled digital detectors was discussed. The situation is further complicated for detectors with severely inhomogeneous detection media. For such detectors, the lack of shift invariance is even more pronounced. Most papers, which describe the determination of the MTF of digital detectors using the Monte Carlo method, deal with homogeneous detection media like amorphous selenium (a-Se) or phosphor plates (Lachaine and Fallone 1998, Lachaine *et al.* 2001, Lachaine and Fallone 2001). For such media, the spread of the deposited energy and thus the signal can be modeled as for any analog system. In practice, the detection medium is subdivided into thin volumes, which score the amount of deposited energy (the signal). If necessary, the sampling of the spread function can be treated in a separate stage. Kausch *et al.* (Kausch *et al.* 1999) evaluated systems consisting of different combinations of metal plates and phosphor screens used for imaging in radiation therapy. The authors score the deposited energy spread in the phosphor. Afterwards, another Monte Carlo code is used to simulate the spread of the generated optical photons. Another work (Spyrou *et al.* 2002) presents Monte Carlo generated images of a bar pattern, which can be used to derive the

MTF. Finally, Cunningham (Cunningham 1997) investigated the degradation of the DQE due to a non-unity detector fill factor at diagnostic energies using an analytical approach.

In this work different Monte Carlo-based approaches to determine MTF_{pre} of a x-ray detector with a severely inhomogeneous detection medium are presented. Unlike other approaches, this work derives MTF_{pre} by scoring the signal in each detector element separately. In other words, the scoring volumes used for the simulations are identical to the actual active volumes of the detector elements. The presented approaches are applicable to a broad range of inhomogeneous x-ray detectors in the diagnostic as well as in the megavoltage energy regime.

As already discussed in the introduction of chapter 3.4 in a more general way, a Monte Carlo-based approach has several advantages. Analytical approaches like the cascaded model (Cunningham *et al.* 1994, Cunningham *et al.* 2002, Rabbini *et al.* 1987), where an imaging system is represented by a series of cascaded processes or stages, on the other hand, are not an alternative. Their extension to inhomogeneous detection media is very challenging and not yet done for a general case or for megavoltage energies and energy integrating detectors, in particular.

Three different methods to determine MTF_{pre} are investigated. The first one is based on sinusoidal input signals. The second approach implements the slanted slit technique and the last one employs a series of delta function inputs shifted by subpixel increments to acquire an oversampled PSF. The implementations of these approaches are illustrated using the proposed multirow/area detector model. The thus determined MTF_{pre} are compared and the strengths and weaknesses of each method are discussed.

3.4.2.2 Detector model

The detector model is based on the model introduced in chapter 3.4.1.2. The element size, however, was chosen to be $1 \times 1 \text{ mm}^2$ and 40 mm in beam direction. The somewhat smaller element size reduces the amount of time required for a Monte Carlo simulation without restricting the possibility to apply the presented methods to a detector array with larger elements. The cavities were modeled to be filled with xenon gas at a pressure of 6 atm. For simplicity, the collecting electrodes were not modeled. The wall thickness was 200 μm if not otherwise stated. The detector array modeled consisted of a 121×121 element array. For the simulations, the 4 MV MVCT beam of the original University of Wisconsin tomotherapy prototype machine was employed.

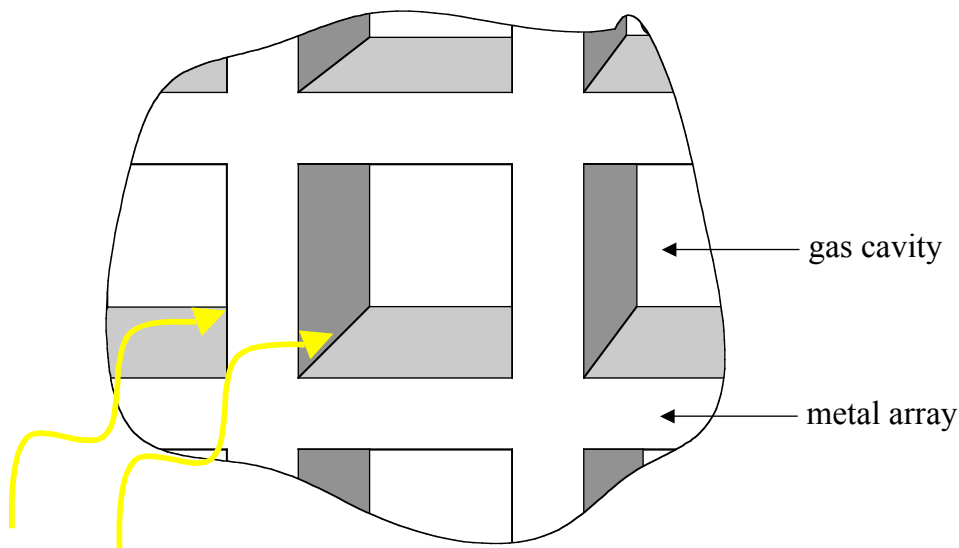


Figure 3.12 Schematic drawing of a part of the multirow/area detector model, which was used to investigate the implementations of three different Monte Carlo-based approaches to determine MTF_{pre} of detectors with severely inhomogeneous detection media. For simplicity the collecting electrodes were not modeled. See text for more details on the chosen design parameters.

3.4.2.3 Slanted sine wave approach

The slanted sine wave approach is based on Eq. (2.2). The practical generation of a sinusoidally varying x-ray intensity is very difficult, whereas the implementation of this definition of the MTF in Monte Carlo simulations is straightforward. It can be shown (Kuhn and Schwierz 1990) that a sinusoidal input as illustrated in figure 3.13 results in the same sinusoidal output with the exception of a reduced amplitude and a phase shift. For a detector with a LSF that is symmetric when reflected at the y-axis, the phase shift is either 0 degree or 180 degrees. In principle slightly more than two samples per sine wave period are required to sample a sine wave properly. However, to investigate the detector response for frequencies beyond the cutoff frequency of the detector, the sinusoidal input was slanted with respect to the detector matrix at an angle of 3 degrees to achieve oversampling. The effective sampling interval $\Delta x'$ was determined to be

$$\Delta x' = \Delta x \tan(\theta) = 0.052 \text{ mm} \quad (3.4)$$

for a detector pitch Δx of 1 mm and a tilt angle of 3 degrees. Thus, the slanting results in an approximately 19 times finer sampling.

As illustrated in figure 3.13, the locations of the scored values of the sinusoidal output are reconstructed by perpendicularly projecting the center of each detector element to a line that runs parallel to the sinusoidal input. Afterwards the scored output values are fitted to a sinusoidal curve. The value of the MTF at the frequency of the sinusoidal input can be calculated using Eq. (2.2).

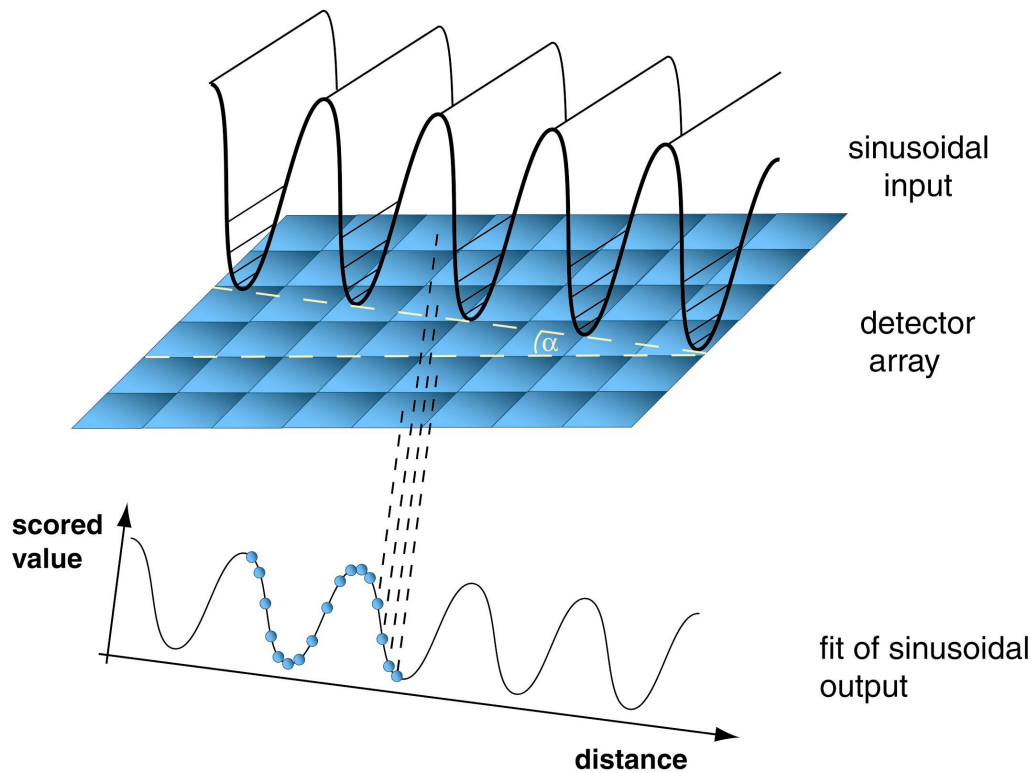


Figure 3.13 Illustration of the slanted sine wave approach. The input, representing a sinusoidally varying x-ray intensity, is slanted with respect to the detector matrix to achieve oversampling. α indicates the tilt angle between the sinusoidal input and the detector row. The input results in the same sinusoidal output with the exception of a reduced amplitude and an eventual phase shift of 180 degrees. The sinusoidal output is obtained by perpendicularly projecting the center of each detector element to an axis, which runs parallel to the sinusoidal input. The scored deposited energy values are plotted at the projected locations. Finally, the data values are fitted to a sine function.

By simulating sinusoids of different frequencies, a one-dimensional representation of MTF_{pre} can be acquired. To make this approach more efficient, an input signal consisting of superimposed sine waves of different frequencies can be generated. This allows the acquisition of MTF_{pre} up to, for instance, its first zero-crossing in one Monte Carlo simulation. This simulation takes as long as a simulation for a single sinusoid. To illustrate this idea, a calculation

of three superimposed sinusoids was performed. Each sinusoidal contribution was weighted equally.

3.4.2.4 Slanted slit approach

The slanted slit approach relies on Eq. (2.3). It is often employed to measure MTF_{pre} of a digital detector. This work, however, implements Fujita's method of a slanted slit (Fujita et al. 1992) in a Monte Carlo simulation. Unlike the experimental equivalent, one does not have to be concerned about the determination of the precise tilt angle of the slit, a varying slit width or a changing x-ray intensity along the slit. On the contrary to the slanted sine wave approach, this technique relies on a broad frequency input in form of an infinitesimally thin line-type input. This slit beam was oriented at an angle of 3 degrees with respect to the detector matrix. The scored detector element values in the vicinity of the slit beam represent the values of the one-dimensional LSF at locations, which correspond to the distances obtained by perpendicularly projecting the centers of the detector elements to the slit beam axis. Similar to the slanted sine wave approach, a 19 times finer sampling was achieved with slanting.

To illustrate how MTF_{pre} can be employed as a first step towards a careful detector design evaluation, MTF_{pre} was determined for detector arrays with different wall thicknesses. The element spacing was kept constant at 1 mm. Four different wall thicknesses were investigated including a 0 μ m thick wall. This special case corresponds to a hypothetical detector consisting only of a xenon gas medium. In this case, the signal is generated by integrating the deposited energy in the gas over $1 \times 1 \times 40 \text{ mm}^3$ volumes.

To get additional insight into the process of photon detection, MTF_{pre} was further analyzed. For this purpose, MTF_{pre} for a wall thickness of 600 μm was split into two components. The first component can be attributed to the primary photons. The other one is mainly caused by scattered photons that undergo further interactions. The source of these scattered photons are the primary photons, which have interacted in the detector. A separation of these two components is possible by fitting an appropriate function through the tails of the LSF. This fit describes the contribution of the scattered photons to the LSF over its whole range. The other component can be calculated by subtracting this fit from the total LSF. In other words, the LSF can be represented as a sum of two individual LSFs. The Fourier transform of these two LSFs yields the corresponding MTF_{pre} . The MTF_{pre} of the total LSF, in turn, is the weighted sum of its individual MTF_{pre} .

To verify that the tails of the LSF are caused by the scattered photons, the slanted slit simulation was repeated. This time, however, the photon fluence through each gas cavity was scored rather than the amount of deposited energy in the gas. The Monte Carlo code MCNP employs the so-called track length estimate to determine the photon fluence through a volume. The photon fluence was scored separately for the primary/unscattered photons and the scattered photons (first to fourth order scattering separately). By default, the MCNP code defines a primary/unscattered photon as a photon, which did not undergo any events since its creation. Thus, it is not able to distinguish between incoming primary photons and photons created by bremsstrahlung, photoelectric and other events as long as they did not undergo any interactions since their creation.

3.4.2.5 Oversampled PSF approach

The PSF approach also relies on Eq. (2.3). Unlike the other two approaches, it yields a two-dimensional representation of MTF_{pre} . The method employs multiple infinitesimally small pencil beams to determine an oversampled PSF. To ensure oversampling (in both dimensions), 13x13 beams covered a detector element. For each pencil beam the deposited energy in the gas was scored in the surrounding 51x51 elements. The beams were not equidistantly spaced. The spacing of the beams pointing at the gas was larger since this part of the PSF was not expected to change rapidly with distance. Consequently, 7x7 beams were directed at the 800 μ m wide gas cavity and the remainder of the beams at the metal wall. In practice, however, only one eighth of the total number of pencil beams needs to be simulated. The data for the other beams can be reconstructed using arguments of symmetry. Due to the low interaction probability in the gas, 12 times more photons histories were run for beams pointing at the gas than for beams pointing at the metal. For each pencil beam the data was remapped using the reciprocity principle. Subsequently, the data from all beams was combined to yield an oversampled PSF. A value of this PSF at a given location indicates the amount of deposited energy in the gas of the central element of the scoring array for an imaginary pencil beam that points at that location. The final result can be interpreted as a "reciprocal" PSF. To determine the associated MTF, the Fourier transform of the PSF needs to be taken. Each practical implementation of a Fourier transform, however, requires an equidistant spacing of the data points. Thus, the PSF was interpolated to a data point spacing of 10 μ m in both dimensions.

It is important to stress that the response was scored in a two-dimensional array of detector elements for each pencil beam. Thus, it is sufficient to raster only a single element with pencil beams. Other implementations are only feasible, when there is a limited amount of crosstalk as

is often the case for diagnostic energies. Drost and Fenster (Drost and Fenster 1982), for instance, translated a slit beam across a single row detector and measured the response in a given single detector element for each slit position.

To evaluate the influence of the wall thickness of the detector array on the extent of the crosstalk and the signal generation, the determination of the oversampled PSF was repeated for the wall thicknesses of 150 μm and 350 μm . For this simulation, an element size of $1.5 \times 1.5 \times 50 \text{ mm}^3$ was chosen.

To illustrate the difference between MTF_{pre} and MTF_{d} and to evaluate the influence of the inhomogeneity of the detector on MTF_{d} , a set of MTF_{d} were determined for a few selected pencil beam locations. Unlike MTF_{pre} , there is no unique MTF_{d} due to undersampling *and* the inhomogeneous nature of the detection medium. Each pencil beam pointing at a location somewhere within the detector element is associated with its own MTF_{d} . To determine such a MTF_{d} , the detector response was scored in 51×51 elements for a given beam. Contrary to MTF_{pre} , the data was not remapped and the data from different pencil beams was not combined to yield one PSF. Hence, each pencil beam results in an undersampled PSF with a data point spacing of 1 sample/mm. The Fourier transform of this PSF divided by the volume underneath the PSF yields MTF_{d} .

3.4.3 Digital Noise Power Spectrum

Besides MTF_{pre} , NPS_{d} has to be known to determine DQE_{d} of the investigated detector model with the wall thickness of 200 μm . The determination of NPS_{d} is based on Eq. (2.8). To

acquire the required flood field images, the geometry shown in figure 3.14 was employed. To minimize any edge effects, the irradiated area is significantly larger than the scoring area. Ideally, the size of the irradiated area would be chosen in such a way that the signal contribution from the incident photons in the periphery of the irradiated area to the scored signal is negligible. In practice, however, time constraints of the simulation impose a limit on the size of the irradiated area. For the same reason the geometric area of the detector model should be significantly larger than the irradiated area. A total of 90 flood field images were acquired using the 4 MV beam of the first tomotherapy machine. For each image $4 \cdot 10^7$ photons were incident on the detector.

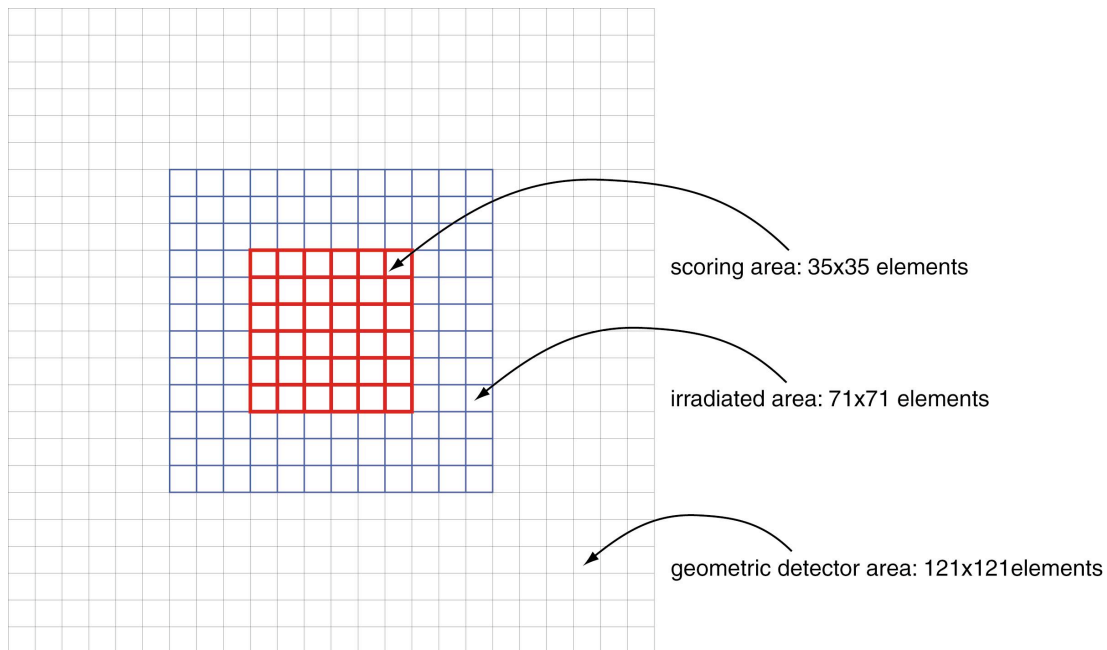


Figure 3.14 Geometry used to estimate NPS_d of the investigated detector model. To minimize any edge effects, the irradiated area is significantly larger than the scoring area. For the same reason the geometric area of the detector is significantly larger than the irradiated area.

Eq. (2.8) requires an infinitively large flood field image. The finite size of the scoring array used leads to a multiplication of the data by a corresponding boxcar function. Consequently, the real NPS_d is convolved with the square modulus of a two-dimensional sinc function. The sidelobes of the sinc squared function produce spectral leakage, wherein noise power from nearby frequencies are mixed in the convolution process. This leakage is particularly pronounced for smaller scoring arrays. To alleviate this problem, each noise image can be multiplied by a special window function (Press *et al.* 1988) separately in the two spatial directions (Stiersdorfer and Spahn 1999). The effects of different kinds of window functions (such as the Parzen and Welch window) on the shape and magnitude of NPS_d were investigated.

Another problem is the required knowledge of the average flood field image. An estimate can be obtained by averaging over the acquired individual flood field images. This estimate of the true mean can lead to erroneous values of NPS_d at lower frequencies in particular for a limited number of individual flood field images (Cunningham 2000).

Dainty and Shaw (Dainty and Shaw 1974) provide a simple expression to estimate the value of NPS_d at zero frequency:

$$NPS_d(0,0) \approx A \sigma_A^2, \quad (3.5),$$

where A designates the area of the flood field image, which is equal to $(35.1 \text{ mm})^2$ in the investigated case. σ_A^2 stands for the variance of the mean detector signal determined from the individual flood field images. The thus determined estimate of $NPS_d(0,0)$ was compared with the

corresponding value of NPS_d obtained through the application of Eq. (2.8). Also an agreement indicates proper normalization of NPS_d .

4. Results

4.1 Prototype detectors

4.1.1 Single element prototype detectors

The single element prototype detectors consisting of different kinds of hollow brass tubes were tested and characterized. In addition, MVCT images of a contrast resolution phantom were acquired to evaluate the imaging capabilities of the prototype detectors.

4.1.1.1 Conversion of DAS/digital units into absolute charge readings per linac pulse

To permit the conversion of the DAS readings into units of charge per linac pulse, the following conversion factor was determined:

$$\text{conversion factor} = \frac{4.97\text{nA}}{200\text{Hz} \cdot 26380 \text{ DAS units}} = 9.42 \cdot 10^{-16} \frac{C}{\text{DAS unit}} . \quad (4.1)$$

The measurements were done with the rectangular tube due to its high signal to induced signal ratio. The conversion factor was used to scale the signal values in many of the subsequent plots.

4.1.1.2 Saturation curves

To determine an appropriate bias voltage for the prototype detectors, saturation curves for the different kinds of tubes were recorded. Figure 4.1 shows the signal of the rectangular and hexagonal tube filled with 6 atm of air as a function of the applied voltage. The saturation curve recorded by the rectangular tube starts to rise again at a voltage of about 110 V. A possible explanation is a disproportionally increasing leakage signal at higher voltages. The curve recorded by the hexagonal tube, on the other hand, does not rise significantly for voltages greater than 70 V.

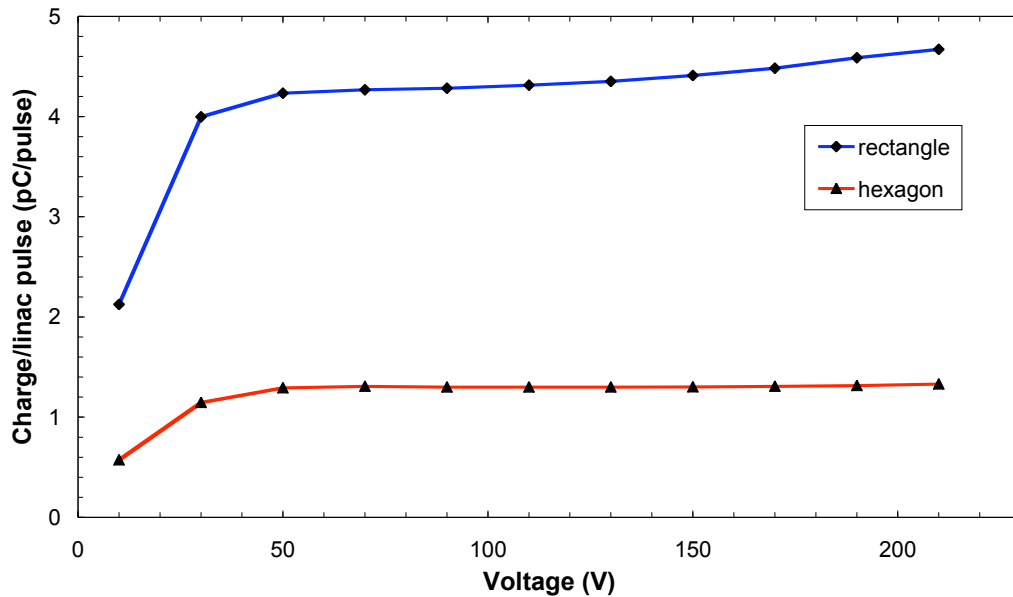


Figure 4.1 Saturation curves for the rectangular and hexagonal tube filled with 6 atm of air. The curve recorded by the rectangular tube starts to rise again at a voltage of about 110 V. A possible explanation is a disproportionately increasing leakage signal at higher voltages. As the recorded signal was averaged over several thousand linac pulses, the statistical error associated with the measurements is negligible.

The same measurement was repeated for 6 atm of xenon as shown in figure 4.2. The signal does not increase significantly for voltages greater than 130 V. Based on figure 4.1 and figure 4.2 a bias voltage of 110 V was chosen for all subsequent measurements. This voltage ensures a sufficiently large charge collection efficiency. On the other hand, the potential is low enough to prevent arcing and increased leakage due to dust and machining defects associated with the handcrafted detectors.

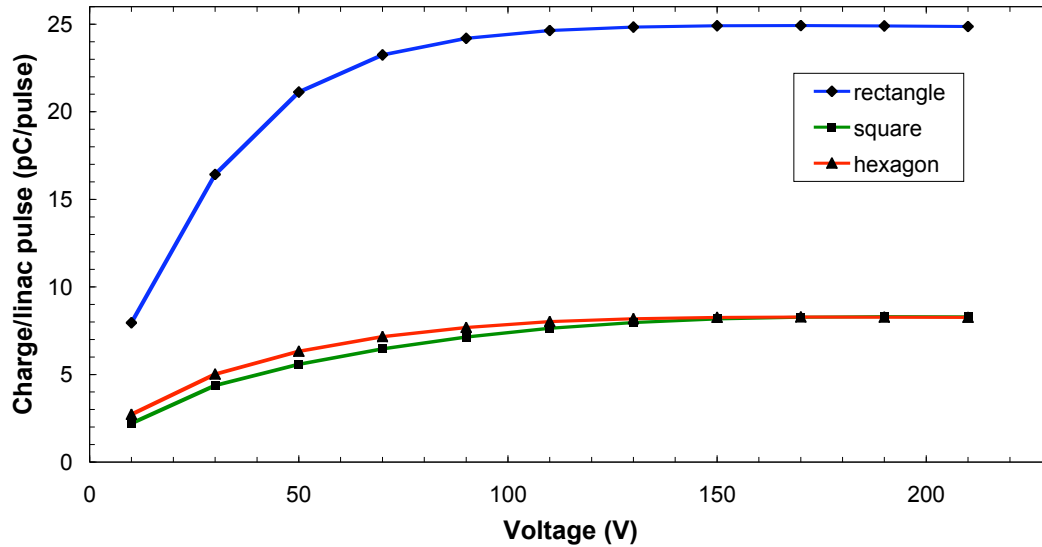


Figure 4.2 Saturation curves for the rectangular, square and hexagonal tube filled with 6 atm of xenon. The rectangular tube shows a significantly larger signal mainly due to its larger cross section. As the recorded signal was averaged over several thousand linac pulses, the statistical error associated with the measurements is negligible.

Because of similar collecting volumes, the hexagonal and square tube show a similar saturation curve. Interestingly, the square tube shows a somewhat lower signal at lower voltages likely because it is more difficult to collect the ionization charges in the corners at lower voltages. At a voltage of 210 V the signal of the rectangular tube is about 3.0 times larger than that of the other two tubes. A factor of roughly 2 is predicted by the difference in the gas volume. Other factors to consider include the shape of the tube and the kind of collecting electrode, i.e. collecting wire versus bar. The latter point was investigated in more detail using Monte Carlo simulations as discussed in a later subchapter.

4.1.1.3 Detector signal as a function of the gas pressure and gas type

To investigate the significance of the type of the gas used and its pressure, the detector signal was recorded for a range of gas pressures using different gases. Figure 4.3 demonstrates the linear increase of the detector signal with rising pressure for air and xenon. This finding was expected, as the electron collision stopping power, describing the energy loss of the high-energy electrons due to hard and soft collisions in the gas, is proportional to the density of the gas and thus approximately proportional to its pressure. However, all linear fits of the data points are associated with a nonzero y-intercept indicating an induced signal originating from electromagnetic stray fields and megavoltage x-ray radiation induced signals in the cabling and connectors. As illustrated in figure 4.3, these y-intercepts were determined from the linear fits and subtracted from the measured data points as an approximate correction for the induced signal as shown in figure 4.4. It was assumed that the magnitude of the induced signal is independent of the gas pressure.

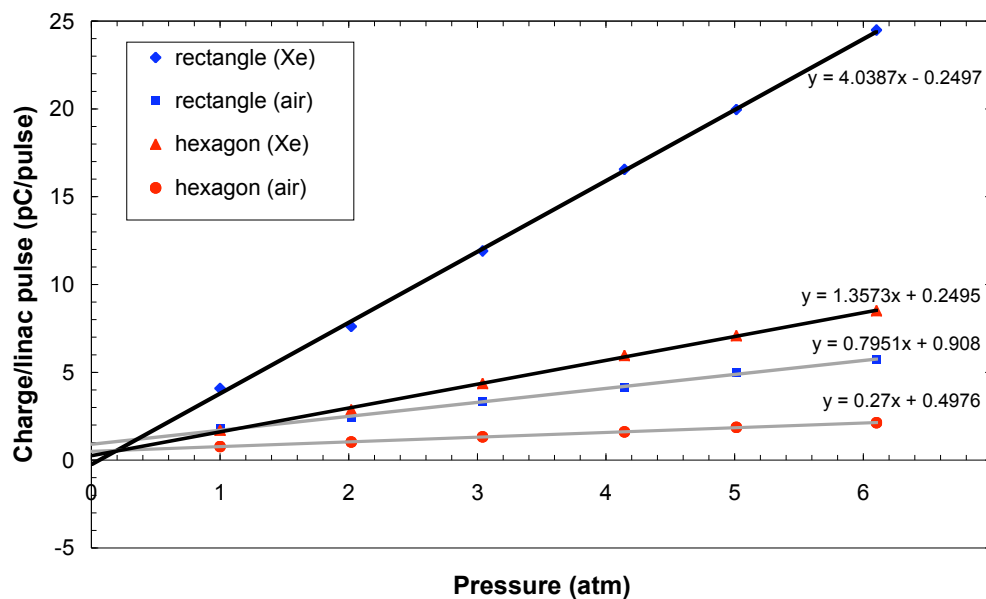


Figure 4.3 Signal of the rectangular and hexagonal tube as a function of the gas pressure for air and xenon. The electron collision stopping power, describing the energy deposition of the high-energy electrons in the gas, is proportional to the pressure of the gas, resulting in the observed linear relationship. For any given pressure and kind of tube, the signal for xenon is significantly larger than for air largely due to the higher density of xenon. The y-intercepts of the linear fits of the data points are a measure for the amount of induced signal originating from electromagnetic stray fields and megavoltage x-ray radiation induced signals in the cabling and connectors.

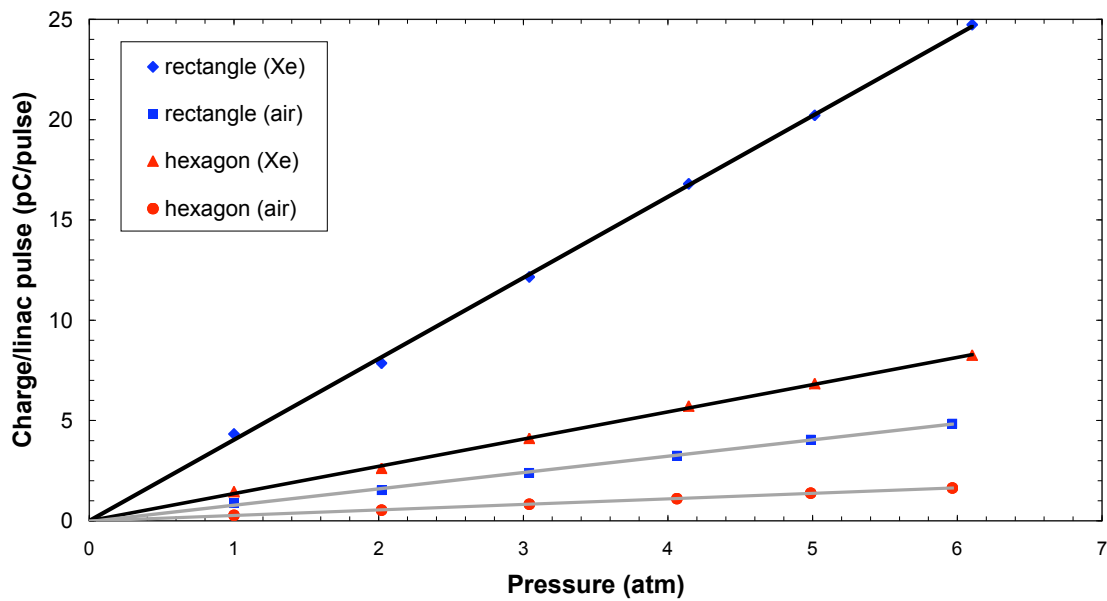


Figure 4.4 Signal of the rectangular and hexagonal tube as a function of the gas pressure for air and xenon. In contrast to figure 4.3, the induced signal (offset) was subtracted from the measured data points. Thus, the linear fits through the corrected data points exhibit the proper quantitative relationship.

For any given pressure and kind of tube, the signal measured for xenon is significantly larger than for air. This observation can largely be attributed to the about 4.6 times higher density of xenon. As already pointed out, the energy deposition of the high-energy electrons, and thus the signal, is proportional to the density of the gas. In addition, the W-value, which describes the average amount of energy required to create an ion pair in the gas, is around 1.5 times lower in xenon. An effect that makes xenon less efficient than air is the about 1.5 times lower electron mass collision stopping power. All three factors together should result in a 4.8 times higher

signal in xenon. This is in excellent agreement with the measured value of 4.9. The relevant properties of both gases are summarized in table 4.1. For both, the measurements in air and xenon, the same bias voltage was employed. As previously shown, there is a slight difference in the collection efficiency in the two different gases. This could result in the small observed discrepancy.

Table 4.1 Properties of the employed gases air and xenon as they are relevant in explaining the large signal measured in xenon opposed to air.

	air	xenon
density ¹ (g/cm ³)	1.205 10 ⁻³	5.485 10 ⁻³
W-value ² (eV/i.p.)	33.97	22.1
electron mass collision stopping power ³ (MeV cm ² /g)	1.712	1.143

¹ at 1 atm and 20°C (Attix 1986)

² (Attix 1986)

³ at the mean energy of the high-energy electrons (about 0.68 MeV) (NIST 2000)

4.1.1.4 Megavoltage CT images of a contrast phantom

To assess the capability of the prototype detectors to acquire MVCT images, a phantom containing plugs of different contrasts was scanned. These images permit an evaluation of the image quality in particular of the contrast resolution. Figure 4.5 shows MVCT slice images acquired with the hexagonal and rectangular tube, respectively. The image acquired with the square tube is very similar to the hexagonal one. This finding was expected due to the similarity of these two tubes (see discussion of saturation curves). The biggest difference between the two

images is the higher noise content of the image acquired with the hexagonal tube. Because of the smaller cross sectional area this tube utilizes less photons for the image formation than the rectangular tube. In both images contrasts down to about $\pm 4\%$ are clearly visible. Even the -2.4% contrast plug is discernible when these images are displayed on a monitor. There are also a few streak artifacts and a ring artifact visible. It should be emphasized that they are not an inherent problem of the detector. They are most likely due to an imperfect implementation of the parallel-beam geometry and due to a linac failure that caused the ring artifact. The dose to the center of the phantom associated with each of these images was around 27 cGy for 6 atm of xenon.

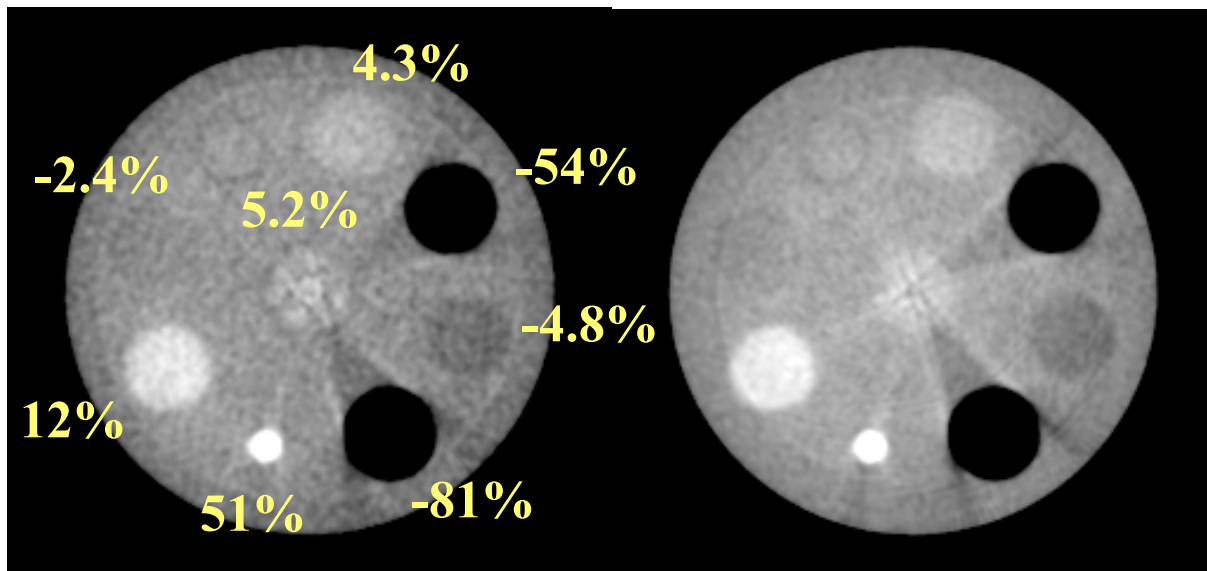


Figure 4.5 MVCT slice image of a contrast phantom acquired with the hexagonal (left) and rectangular tube (right). The numbers denote the contrasts of the plugs in terms of electron densities. The dose to the center of the phantom associated with each of these images was about 27 cGy for 6 atm of xenon. The visible artifacts are most likely due to an imperfect implementation of the parallel-beam geometry.

4.1.2 Multielement prototype detectors

The results of the single element prototype detectors encouraged the development of multielement detectors. The first detectors of this kind were single row prototypes. Then, a 4x4 element detector was built and tested.

4.1.2.1 Single row prototype detectors

The first multielement prototype detector, shown in figure 3.6, consisted of a single row of five elements. As a first step towards the characterization of this detector, the response of the elements c, 1 and 1' was measured for different field sizes. Figure 4.6 shows that the recorded signals increase continuously with the field width. For larger widths the increase levels off. These results were expected since the output factor of the linac increases in a similar fashion (Kahn 1994). In other words, the detector responds to the changing dose rate of the linac.

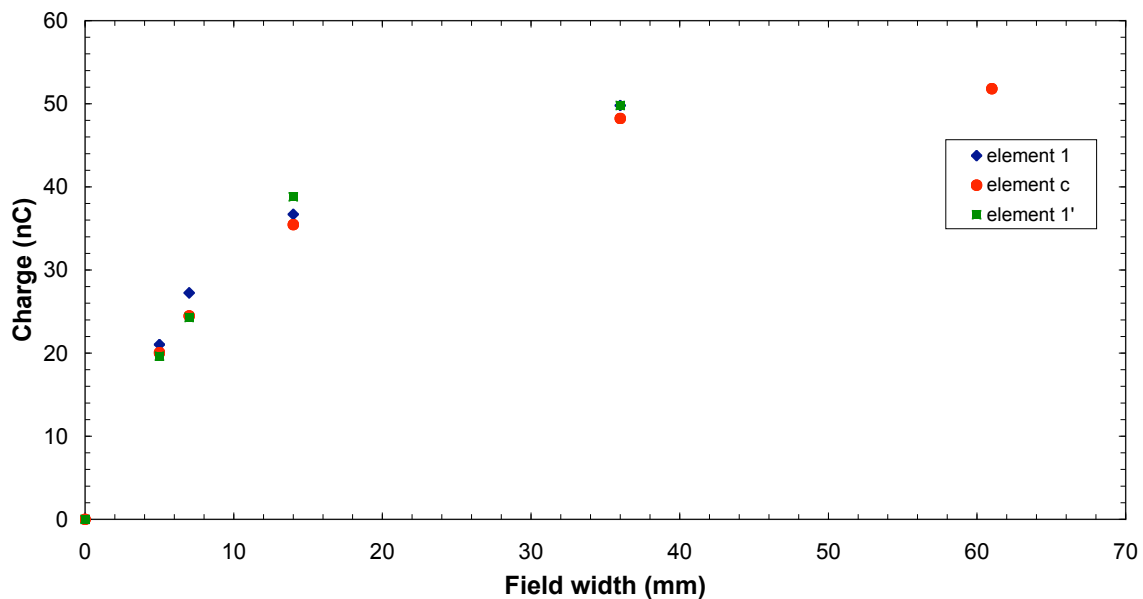
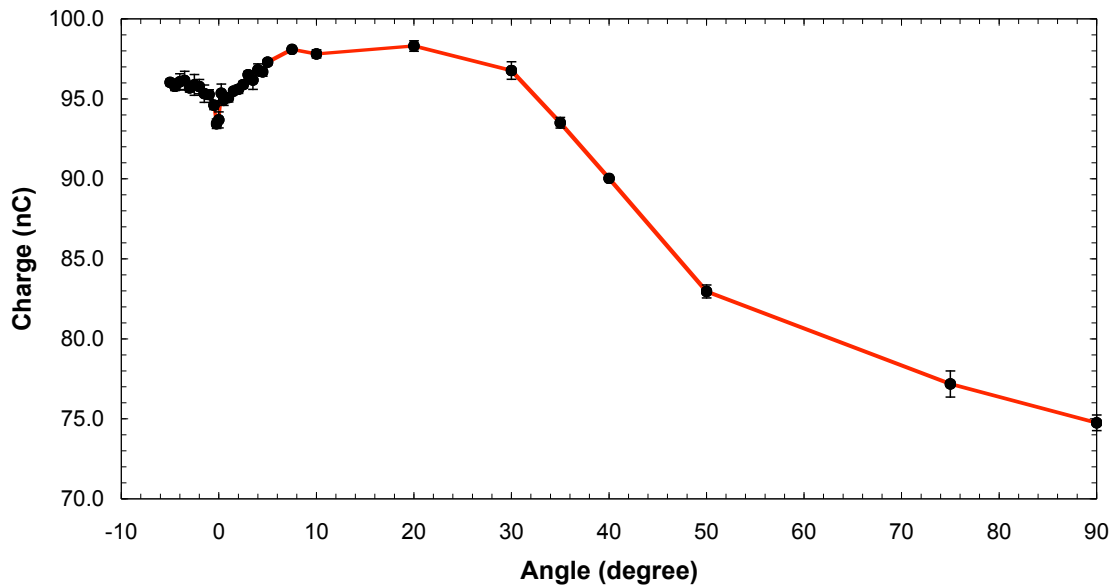


Figure 4.6 Measured response of the elements c, 1 and 1' of the first multielement prototype detector for different field sizes (cf. figure 3.6 for labeling of elements). The response is expressed as the collected charge for a 100 MU

irradiation. The field size in the vertical direction was kept constant at 12 mm. At a field width of 61 mm only element c was read out. The elements exhibit a non-uniform response due to the non-uniform element and detector structure (cf. figure 3.6). The 1 σ error bars, determined from a set of repeated measurements, are too small to be shown (less than 1% for each data point).

To determine the angular sensitivity of the detector, the detector was rotated about its vertical axis. The signal of the central element c was read out at different angular positions. Figure 4.7 shows the response for an angular range of -5 degrees to +90 degrees. Clearly, there is a minimal response at an angle of about 0 degree. At this angle the walls of the elements, the shims and the HV electrode structure run parallel to the photon beam. Thus, a large fraction of the photons traverses the detector without traveling through metal. As soon as the detector is rotated, the signal rises. Now a larger fraction of photons travels through at least a little bit of



metal. Consequently, more interactions take place and the signal increases. For angles greater than about 20 degrees, the signal starts to decrease. At these angles, an increasing fraction of the photons has to travel through the Al spacer and the elements, which lie in front of the central element. This material results in an increased attenuation of the beam. Figure 4.8 shows an enlarged view of the angular response around 0 degree. The slight asymmetry of the curve results in part from the behavior of the linac, whose output slightly changes with time.

Figure 4.7 Signal of the central element of the first multielement prototype detector for different angular orientations. The signal is expressed as the collected charge for a 100 MU irradiation. The detector was rotated about its vertical axis. At an angle of 0 degree the metal structures of the detector run parallel to the beam. Thus, a large fraction of the photons traverses the detector without traveling through metal. The 1σ error bars were determined from a set of repeated measurements.

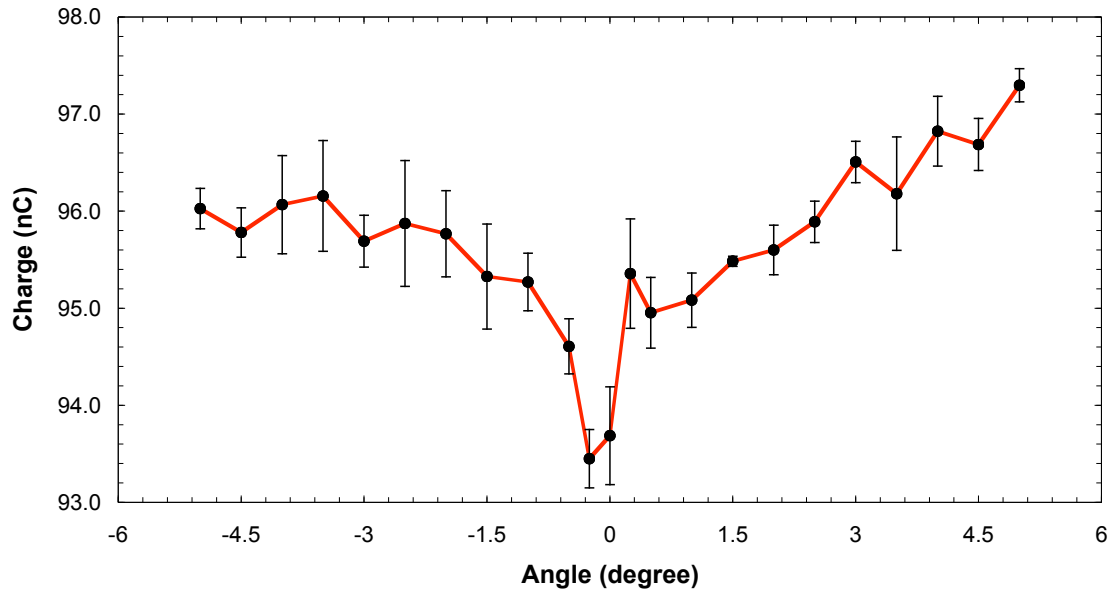


Figure 4.8 Enlarged view of figure 4.7 showing the minimal detector response at the angle of about 0 degree. The 1σ error bars were determined from a set of repeated measurements.

To investigate the importance of the material of the HV electrode, HV electrodes made of aluminum, copper, lead and tantalum were fabricated and tested. The investigations focused on practical aspects. Lead and tantalum have a high density of 11.35 g/cm^3 and 16.4 g/cm^3 resulting in an increased attenuation of the photon beam. Lead, however, is a soft metal. It can easily be scratched and deformed. Consequently, the detector with a lead HV electrode showed severe problems with arcing and short-circuits. Tantalum, on the other hand, caused problems during the fabrication of the HV electrode although this metal is considered to be ductile. Ultimately, the same problems of arcing and short-circuits were observed with tantalum. Copper has an

intermediate density of 8.96 g/cm^3 . Although the fabrication of the HV electrode with copper was straightforward, large leakage currents during the testing were observed. Finally, aluminum with its lowest density of 2.7 g/cm^3 , formed the most reliable and rugged HV electrode.

The purpose of the next prototype was to built a more reliable and rugged detector especially in regard to the leakage current and short-circuits. This also includes the need for a more uniform structure of the elements. Based on the previous findings, aluminum was the material of choice for the HV electrode. The second single row prototype detector is shown in figure 3.7 and figure 3.8.

To illustrate the effectiveness of the detector in comparison to a conventional ionization chamber, the charge per collecting gas volume was measured for the central element c as well as for a Farmer ionization chamber. Both detectors were irradiated under the same conditions. The collecting volume of the central element (excluding the volume occupied by the shim) was measured to be

$$(0.102 \cdot 0.551 \cdot 4.2) \text{ cm}^3 \square (0.0127 \cdot 0.54 \cdot 4.2) \text{ cm}^3 = 0.207 \text{ cm}^3 . \quad (4.2)$$

The volume of the Farmer chamber, on the other hand, was specified to be approximately 0.7 cm^3 . Knowledge of the volumes, together with the measured charge values, allow a calculation of the signal per collecting gas volume value, which was determined to be 464 nC/cm^3 for the central element and 35 nC/cm^3 for the Farmer chamber. Thus, the measured charge per collecting volume was about (13 ± 1.5) times larger for the prototype detector than for the ion chamber. The error was estimated from the dominant error of the central element

measured gas volume. This result illustrates the highly effective signal generation of the Al HV electrode and the steel shim, which surround the gas cavity.

To better understand the contributions of the different components of the detector to the measured signal, Monte Carlo simulations were performed using the real detector geometry. For this purpose, the detector was decomposed into HV electrode, shims, epoxy, Al spacer and air components. Table 4.2 summarizes the results. A broad beam was used for the simulations. If all components were replaced by air, the scored signal would only be 3% to 4% of the original signal. This illustrates that very few photons directly interact in air. Intriguingly, surrounding the air cavities with the HV electrode made of aluminum increases the scored signal by a factor of 12. Although the steel shims occupy only a small volume in comparison to the HV electrode, they contribute about 1/3 to the total signal. This is due to the high density of steel, which is about three times higher than for aluminum. These figures illustrate the importance of high density materials in regard to the signal generation. Other components such as the epoxy also contribute to the signal. Interestingly, the contribution of the shims to element 2 is significantly lower than to element c and 1. This finding might indicate the significance of the crosstalk, which partly originates from the shims. One of the elements bordering element 2 does not have a shim (cf. figure 3.8). Thus the crosstalk from this shim is missing, which could explain the lower contribution of the shims to element 2. The contributions of the shims to the elements c and 1 are about the same. This, in turn, might indicate that most of the crosstalk originating from the shims, comes from the shims located in the adjacent elements and not from elements farther away. The recorded crosstalk from the Al spacer, on the other hand, is largest in element 2. It is lowest in the element c, since it gets attenuated by several shims and element walls before it

reaches the central element. Although the three investigated elements have the same structure, the scored total signal is different due to crosstalk. Crosstalk is particularly important at megavoltage photon energies.

Table 4.2 Percentage contributions of the different components of the detector to the signal scored in the elements c, 1 and 2. The contributions were determined by adding the individual components one-by-one in the order listed. For each step, the deposited energy was scored in the same volumes, which correspond to the gas cavities of the elements. To allow for a comparison of the contributions of the different elements on an absolute basis, the total signal recorded by an element is listed as an absolute value. A broad beam was used for the simulations.

Percentage signal contribution from	element c	element 1	element 2
air	3.7	3.5	3.5
Al spacer	2.2	3.8	8.0
epoxy	13.7	15.0	15.6
shims	35.6	33.6	22.2
Al HV electrode	44.8	44.1	50.7
total (absolute value (a.u.))	1.00	1.06	1.06

These findings motivated the investigation of the influence of the wall thickness on the signal and the crosstalk. For this purpose, a narrow beam, covering only the central element, was employed. Therefore, element c records the primary signal whereas elements 1 and 2 score the amount crosstalk. In addition, the signal per gas volume was determined for element c as a measure of the effectiveness of the signal generation. Table 4.3 summarizes the results. As can

be seen, the primary signal is largest for the two smaller wall thicknesses. The primary signal per gas volume, on the other hand, continuously decreases with decreasing wall thickness, meaning less energy is deposited per unit gas volume. Nevertheless, as the element width is kept constant, thinner walls are still more effective in generating the primary signal. While the increase of the primary signal is relatively small, the crosstalk increases more rapidly for thinner walls. Moreover, the amount of crosstalk decreases rapidly with increasing distance from the central element.

Table 4.3 Primary signal as well as the amount of crosstalk recorded by the element c and the elements 1 and 2, respectively, for different Al wall thicknesses. For element c, the signal per collecting gas volume was determined, too. A narrow beam, covering just the element c, was employed for the simulation. The numbers are normalized with respect to the signal the signal/gas volume of element c for a wall thickness of 430 μm (corresponding to the actual prototype design), respectively. All values are in percent.

wall thickness (μm)	element c		element 1	element 2
	signal	signal/gas volume	crosstalk	crosstalk
430	100.0	100.0	24.1	5.4
300	105.4	91.9	28.9	6.6
180	105.4	81.4	34.9	8.4

To investigate the significance of the material of the HV electrode, the above simulations were repeated for copper and tungsten. Table 4.4 summarizes the results. For all materials an increase in signal for thinner walls is observed since the generated high-energy electrons can more easily leave the wall without being attenuated. Moreover, the volume of the gas cavity increases so that a given high-energy electron can deposit more energy. The amount of crosstalk,

however, also rises with decreasing wall thickness. Obviously, copper is much more efficient in regard to the signal generation and the reduction of the crosstalk than aluminum. This effect is even more pronounced for tungsten due to its high density of 19.3 g/cm^3 and its high atomic number of 74. For a wall thickness of $430 \text{ }\mu\text{m}$, the signal generated in the central element is about 1.4 times larger for tungsten than for aluminum. In addition, tungsten reduces the crosstalk between the central element and element 1 about 3.5 times more effectively than aluminum for all investigated wall thicknesses. These figures illustrate the superior properties of high density and high atomic number materials like tungsten.

Table 4.4 Comparison of the signal and the crosstalk for different HV electrode materials and wall thicknesses illustrating the superior properties of high density and high atomic number materials such as tungsten. The simulated beam covers only the central element. The signal is normalized with respect to the signal of the central element for Al with a wall thickness of $430 \text{ }\mu\text{m}$ (corresponding to the actual prototype design) and expressed in percent. The crosstalk is defined to be the ratio of the signal in element 1 to the signal in element c expressed in percent.

wall thickness (μm)	Al		Cu		W	
	signal	crosstalk	signal	crosstalk	signal	crosstalk
430	100.0	24.1	121.1	14.0	139.8	6.9
300	105.4	27.4	127.7	14.2	154.8	7.4
180	105.4	33.1	129.5	19.1	165.1	10.2

Finally, the influence of an aluminum build-up plate in front of the detector on the recorded signals was investigated. The same narrow beam geometry as before was employed for the

simulations. For a plate thickness of 1 mm and 2 mm, the signal in the central element increases by about 5% and 4%, respectively. The signal in element 1 rises by about 2.5% due to the increased amount of crosstalk whereas the signal in element 2 stays nearly constant.

4.1.2.2 4x4 element prototype detector

The next step in the development of a detector system was the transition from a single row detector to a multirow/area detector. Thus, a 4x4 element detector was built as shown in figure 3.9 A preliminary testing of this prototype supports the feasibility of such a design. All elements can be read out simultaneously with multiple ribbon cables directly connected to the detector. A drawback of this design is its tubular structure. The space between the tubes is not utilized. The construction of this detector also revealed challenges from the point of engineering. One problem are the small dimensions of a detector element. Moreover, the centering of the collecting wires requires great care to avoid problems such as arcing or short-circuits.

4.2 Monte Carlo-based characterization of a multirow/area detector model

4.2.1 Separation of the total signal into a primary and crosstalk component

To illustrate the concept of the separation of the total signal into a primary and crosstalk component, the primary signal as well as the pattern of the crosstalk were determined for a 41x41 element detector array by irradiating the central element only. Figure 4.9 shows the spatial pattern of the crosstalk as well as the primary signal recorded by the central element. Figure 4.10 shows an enlarged view of figure 4.9. Each rectangular patch represents a detector element. Origin of the crosstalk is, to a large part, Compton-scattered photons generated through

interactions in the central element that undergo further interactions in the detector. In addition, high-energy electrons coming from the central element contribute to the crosstalk. Their range in metal, however, is very limited so that they can reach only the adjacent elements. Finally, these electrons also emit bremsstrahlung that can travel longer distances. It is seen that the amount of crosstalk decreases rapidly with distance from the central element (taking into account the logarithmic nature of the plot).

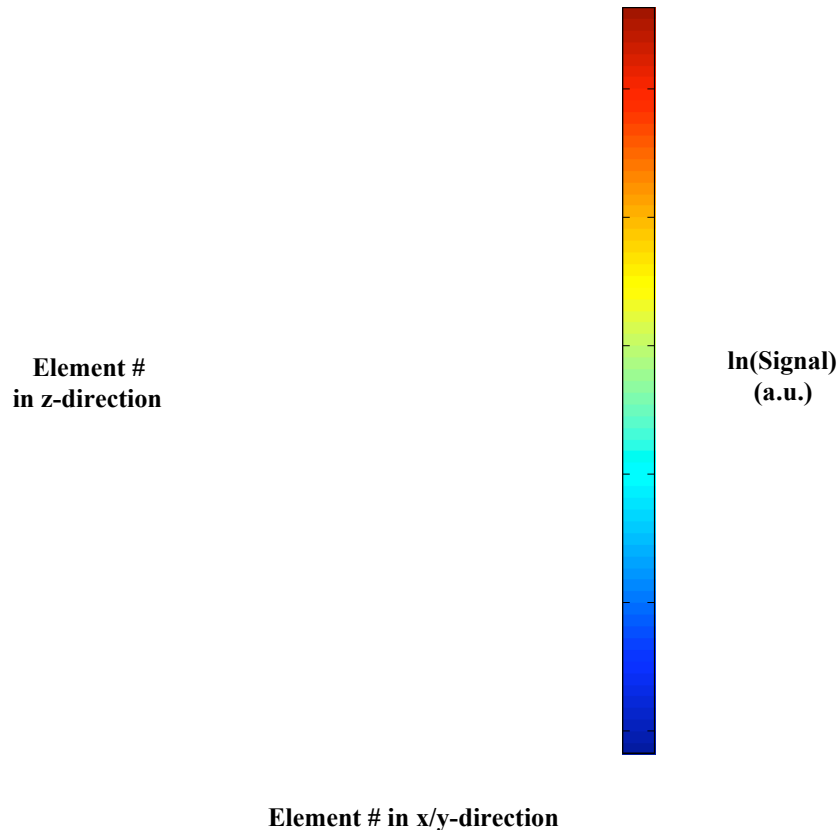


Figure 4.9 Monte Carlo simulation of the primary signal and spatial pattern of the crosstalk for a 41x41 element detector array. Each rectangular patch represents a detector element. Only the element in the center was irradiated. This element records the primary signal. The amount of crosstalk decreases rapidly with increasing distance from the central element.

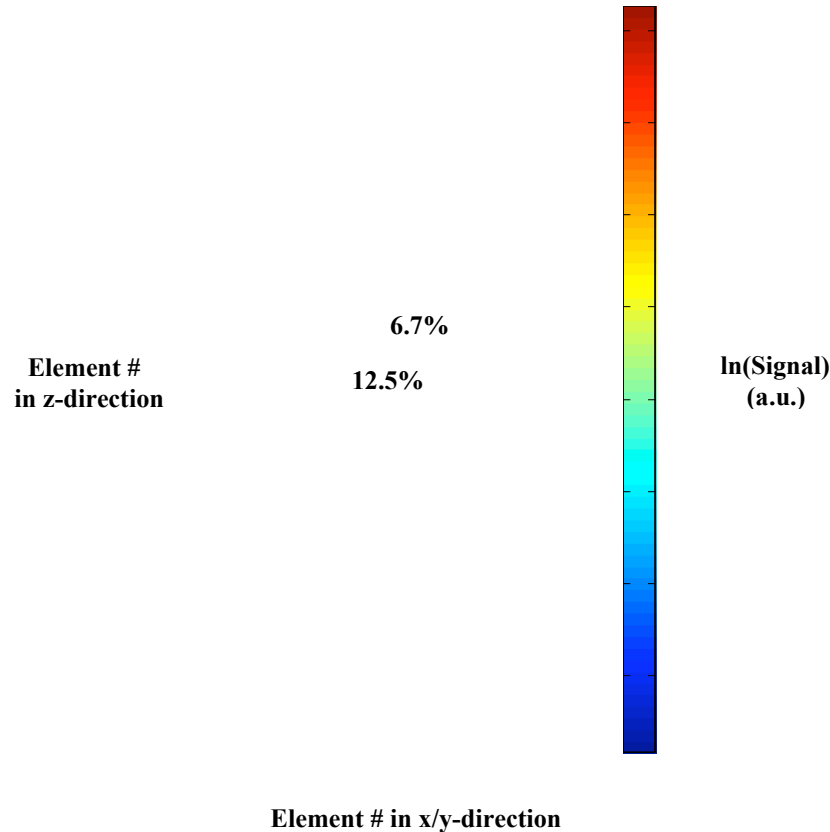


Figure 4.10 Enlarged view of figure 4.9 showing the primary signal and spatial pattern of the crosstalk in the immediate vicinity of the irradiated element. Due to the lack of rotational symmetry of the detector array, the crosstalk in this range is much more structured than farther away from the irradiated element. The numbers designate the amount of crosstalk recorded in the two elements adjacent to the irradiated element expressed as a percentage of the primary signal.

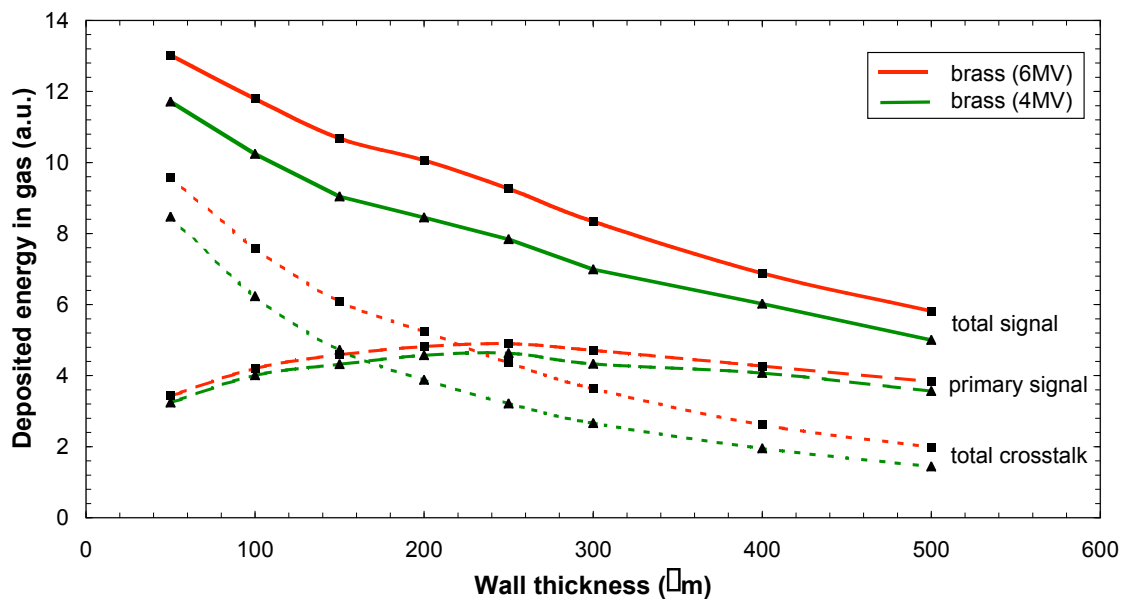
4.2.2 Significance of the wall thickness of the detector array

As seen in chapter 4.2.2.1, the wall thickness of the detector array is an important parameter that determines the extent of crosstalk as well as the amount of primary signal recorded by an element. For this purpose, the primary signal, the total amount of crosstalk as well as the total signal comprised of the sum of primary signal and total crosstalk were scored for detector arrays with different wall thicknesses. Figure 4.11 shows the results for a detector array made of brass

for the 4 MV and 6 MV photon beam. The wall thickness was varied from 50 μm to 500 μm . The primary signal exhibits a maximum at a wall thickness of about 250 μm . For smaller thicknesses the cross section of the metal walls seen by the photons is too small to result in a significant number of interactions. On the other hand, when the wall thickness is too large, the gas volume is too small. The pathlengths of the high-energy electrons through the gas cavity are too short to result in a significant energy deposition. In addition, a certain fraction of the high-energy electrons, particularly those created in the middle of the wall, gets absorbed in the metal before they can reach the cavity.

Interestingly, for a 6 MV beam the primary signal recorded is only slightly larger than that for the 4 MV beam (figure 4.11). At a wall thickness of 250 μm the signal is larger by about 6%. The reason for the increase in signal is that, on average, higher energy Compton electrons set in motion from the photons of the 6 MV beam result in more electrons reaching the gas cavity. Figure 4.11 also shows the total amount of crosstalk recorded. As expected, the crosstalk decreases continuously with increasing wall thickness. Although the 6 MV beam showed only a small increase in primary signal when compared to the 4 MV beam, the 6 MV beam exhibits a significantly larger amount of crosstalk. Compton-scattered photons originating from the primary photons of the 6 MV beam have, on average, a higher energy than the ones from the 4 MV beam. These scattered photons create electrons with higher energies when they undergo further interactions. Consequently, it is more likely that these electrons reach a cavity and contribute to the crosstalk.

Finally, figure 4.11 also shows the total signal in a given element, which is equal to the sum of the primary signal and the total amount of crosstalk, for both photon spectra. Unlike the primary signal, the curves do not show a maximum. There is only a region of a reduced fall off corresponding to the wall thickness of maximal primary signal. The large amount of crosstalk at smaller thicknesses washes out the maximum found for the primary signal. The ratio of the primary signal to the total amount of crosstalk increases continuously with increasing wall thickness. This ratio, however, is not a good figure of merit. A large value of the ratio can be caused by a low primary signal and a very small amount of crosstalk. A low primary signal,

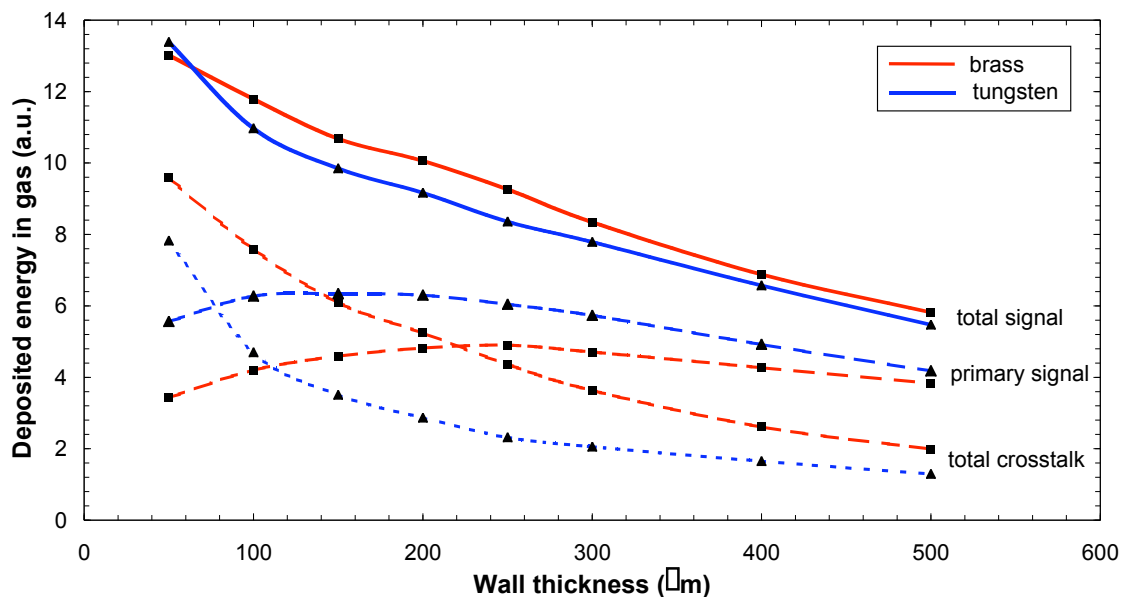


however, is not desirable since it indicates a low detection efficiency and a signal that is difficult to measure. In addition, the ratio does not take into account the complex nature and implications of the crosstalk.

Figure 4.11 Primary signal (long dashed line), total amount of crosstalk (short dashed line) and total signal (solid line) of a brass detector array for a 4 MV and 6 MV photon beam, respectively. The total signal recorded by an element can be regarded as the signal of this element in the case of a broad photon beam that covers many elements

(reciprocity principle), i.e. it is directly related to the measured signal for a more practical situation. Unlike the primary signal, the total signal does not show a maximum. This is mainly due to the large amount of crosstalk for smaller thicknesses, which washes out the maximum of the primary signal. In comparison to the 4 MV beam, the 6 MV beam exhibits a significantly larger amount of crosstalk but only a slightly increased amount of primary signal.

To investigate the significance of the material, the above calculations for the 6 MV beam were repeated for tungsten. Figure 4.12 compares the primary signal, the total amount of crosstalk and the total signal for a 6 MV beam for a detector array made of brass and tungsten, respectively. The primary signal for tungsten is significantly higher than for brass especially at smaller wall thicknesses. In addition, the maximal primary signal is associated with a much smaller wall thickness of about 150 μm . Although the primary signal is much higher for tungsten the total amount of crosstalk is greatly reduced. Due to the smaller amount of crosstalk the total signal for tungsten is lower than for brass at least for wall thicknesses ranging from



about 100 μm to 500 μm .

Figure 4.12 Comparison of the primary signal (long dashed line), the total amount of crosstalk (short dashed line) and the total signal (solid line) for a 6 MV beam for a detector array made of brass and tungsten, respectively. The primary signal for tungsten is significantly higher and it shows a maximum at a wall thickness of about 150 μm . In addition, the crosstalk is greatly reduced especially at smaller wall thicknesses.

4.2.3 Distribution of the deposited energy in an element along the beam direction

Knowledge of the distribution of the primary and crosstalk signal along the beam direction can help to find the optimal length of the detector (element) in beam direction. Figure 4.13 shows the amount of deposited energy in the gas as a function of the depth for the irradiated (element A) and for the elements one and two element widths away from the irradiated element (element B and C). After reaching a maximum at a depth of roughly 0.5 cm, the primary signal decreases continually. Although the chosen length of the brass element of 6 cm results in an attenuation of the incoming photon beam by more than 93%, the primary signal at the rear end of the element is still about 20% of the maximum value. The crosstalk signal behaves very similar. However, the maximum of the signal is more prominent and shifted towards a larger depth. To clarify, if the primary signal or the crosstalk decreases more rapidly with increasing depth at larger depths, the ratio of the crosstalk signal to the primary signal in element A was taken. The ratio was calculated for the crosstalk in element B as well as in element C. Figure 4.14 demonstrates that the primary signal decreases more slowly with increasing depth (at larger depths) than the crosstalk signal. These findings suggest an increase of the length of the detector element. Because of the more rapid fall off of the crosstalk this would increase the total amount of detected primary signal disproportionately to the total amount of recorded crosstalk.

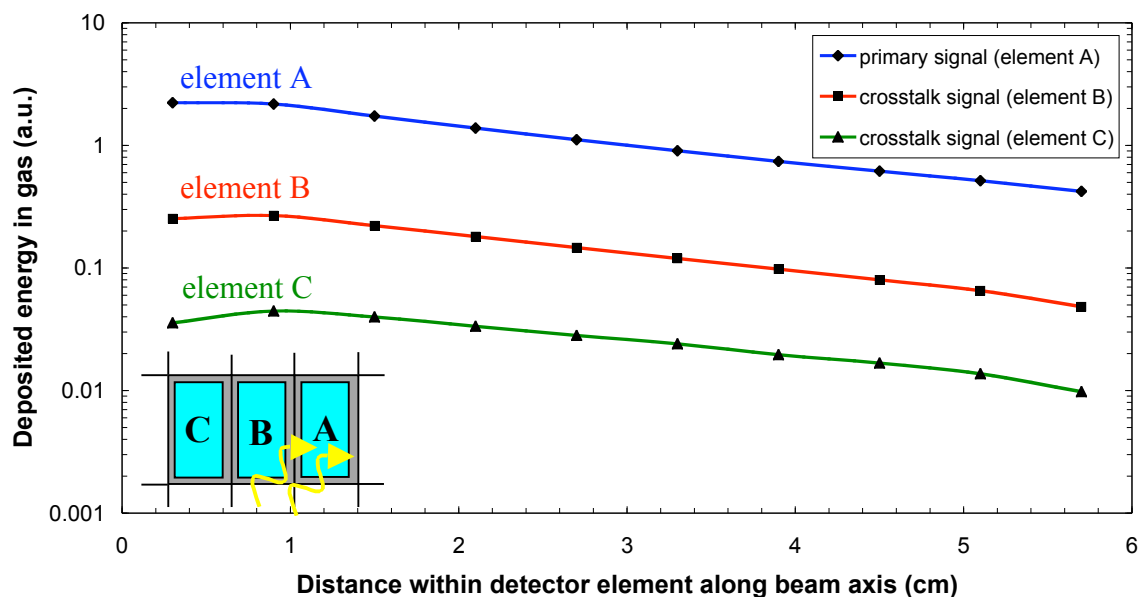


Figure 4.13 Distribution of the deposited energy in the gas as function of the depth in a given detector element similar to a depth-dose-profile in radiation therapy. The plots show the results for the irradiated (element A) and the two elements one and two element widths away from the irradiated element, respectively (element B and C). Although the length of the element was chosen to attenuate the incoming photon beam by more than 93%, the primary signal at the rear end of the element was still about 20% of the maximum value.

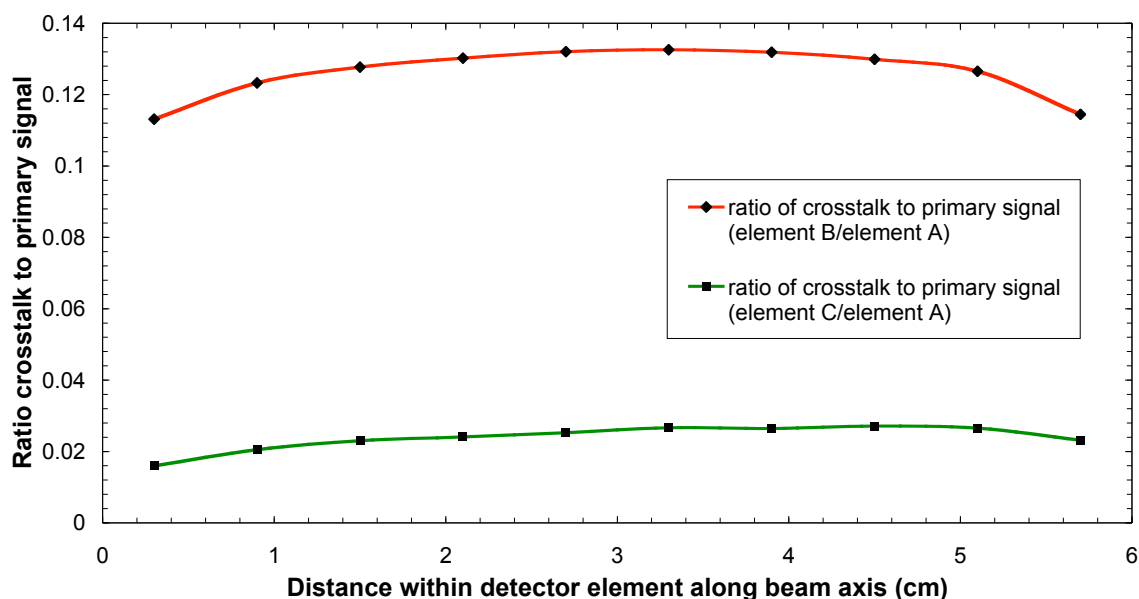


Figure 4.14 Ratio of the crosstalk to the primary signal (element A) for the elements B and C. The fall off of the ratio at larger depths illustrates that the crosstalk signal decreases more rapidly with increasing distance than the

primary signal. This finding suggests that an increase of the element length would increase the total amount of detected primary signal disproportionately to the total amount of detected crosstalk.

4.2.4 Significance of the collecting electrodes

Different kinds of collecting electrodes were investigated in terms of the amount of deposited energy. As previously shown, it is difficult to collect the charges in the corners of a tube with a square or rectangular cross section with a single collecting wire especially for lower bias voltages. To minimize this problem, the proposed elements with a rectangular cross section require two collecting wires. Alternatively, a collecting bar could be employed. The resulting geometry, resembling a parallel plate chamber, should be more suitable to collect the charges, in particular in the corners of the detector element. However, as already pointed out, a bar might be associated with some manufacturing issues. Different kinds of electrodes and dimensions were tested using Monte Carlo simulations. An element without any collecting electrodes served as a reference. For this case, a deposited energy value of 100% was arbitrarily assigned. At first, two steel wires with a diameter of 0.6 mm and a length equal to the length of the element were placed 0.7 mm above and below the center of the cavity, respectively. As listed in table 4.5 the relative amount of deposited energy dropped to about 94%. There are two competing effects to consider. The placement of additional material in the beam should result in an increased number of high-energy electrons released into the cavity. It is believed that this effect is overcompensated by the absorbance of some of the high-energy electrons, mainly coming from the walls of the element, by the wires. Without the wires in place, the electrons would have continued to travel through the other half of the cavity creating many more ionization charges. In addition, the presence of the electrodes result in a reduction of the available gas volume. Table

4.5 also lists the gas volume relative to the element without any electrodes. In general, the smaller the gas volume the smaller the amount of deposited energy. However, it is evident that the reduction of the gas volume alone cannot explain the determined numerical values. For the above reasons, a thinner wire should result in a higher recorded energy. For instance, wires with a diameter of 0.3 mm are associated with an energy value close to one of the reference element (cf. table 4.5). There might even be a wire diameter that results in a relative energy value above 100%. Finally, the use of a collecting bar was investigated. The bar with the dimensions of $0.25 \times 1.85 \text{ mm}^2$ was centered in the cavity. The scored energy was 96%. Once again, the energy value depended on the dimensions of the bar.

Table 4.5 Influence of the type of electrode on the amount of energy deposited in the gas of an element of a detector array with rectangular elements. An element without any collecting electrodes served as a reference. It was arbitrarily assigned an energy value of 100%. In general, thinner collecting wires result in higher energy values since they are associated with a smaller reduction of the gas volume with respect to the element without any collecting electrodes and they absorb less high-energy electrons mainly coming from the wall of the element. This effect overcompensates the increased production of high-energy electrons due to the presence of additional material in the beam. The same arguments apply to a collecting bar.

type of electrode	dimension	rel. gas volume	rel. amount of deposited energy
w/t electrodes (reference)	----	100%	100%
two thicker wires	Ø 0.6 mm	85.8%	93.9%
two thinner wires	Ø 0.3 mm	96.4%	99.5%
single bar	$0.25 \times 1.85 \text{ mm}^2$	88.4%	96.0%

4.2.5 Determination of the presampling MTF

The determination of the presampling MTF is a first step towards the derivation of the DQE(f) of the investigated detector model. Three approaches to determine the presampling MTF were investigated. The MTF_{pre} derived from the different methods were compared. In addition, the strengths and weaknesses of each approach was evaluated.

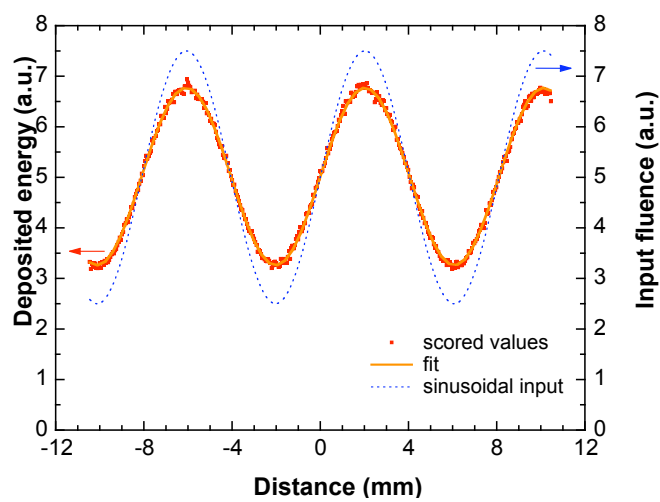
4.2.5.1. Slanted sine wave approach

To acquire a one-dimensional representation of MTF_{pre} with the slanted sine wave approach, sinusoidal input signals of different frequencies (wavelengths) were simulated. Figure 4.15 (a) shows an example for a wavelength of 8.1 mm. Clearly, slanting results in oversampling and consequently in many data points per sine wave period. Figure 4.15 (b) shows the result for a shorter wavelength (1.2 mm). Interestingly, there is a 180 degrees phase shift between the input and output signal. This was expected since the chosen wavelength corresponds to a frequency, which lies within the first sidelobe of MTF_{pre}. All of these frequencies experience this phase shift of 180°. Finally, figure 4.15 (c) illustrates the importance of slanting the input signal. The same input as for panel (b) was employed with the exception that the sinusoidal input was aligned with the detector array (0 degree tilt angle). Thus, the sampling rate is only equal to 1 sample/mm. As the frequency of the input signal was chosen to be beyond the cutoff frequency of the detector, the output is undersampled. Consequently, a sinusoidal output with a lower frequency than the sinusoidal input was reconstructed due to the aliasing effect. The frequency of the undersampled sinusoid f_{under} can be calculated from the cutoff frequency f_{cutoff} and the frequency of the properly sampled (oversampled) sinusoid f_{over} by reflecting f_{over} at f_{cutoff} to a lower frequency:

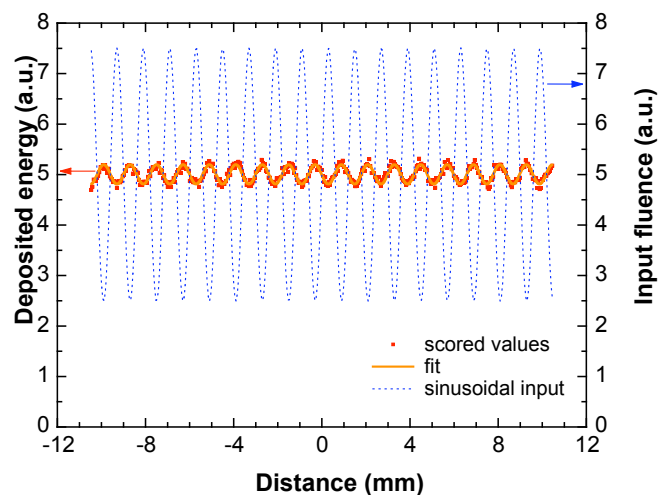
$$f_{\text{under}} = f_{\text{cutoff}} - (f_{\text{over}} - f_{\text{cutoff}}) = 0.167 \frac{\text{cycles}}{\text{mm}}, \quad (4.3)$$

where f_{cutoff} amounts to 0.5 cycles/mm and f_{over} to $\frac{1}{1.2 \text{ mm/cycle}} = 0.833 \frac{\text{cycles}}{\text{mm}}$. The aliasing effect does not change the magnitude of the modulation of the sinusoidal output signal. A quantitative analysis of figure 4.15 (c) revealed a frequency f_{under} of 0.167 cycles/mm and a corresponding MTF_{pre} value, which was equal to the MTF_{pre} value at f_{over} within 2.6% in excellent agreement with the theory of aliasing.

(a)



(b)



(c)

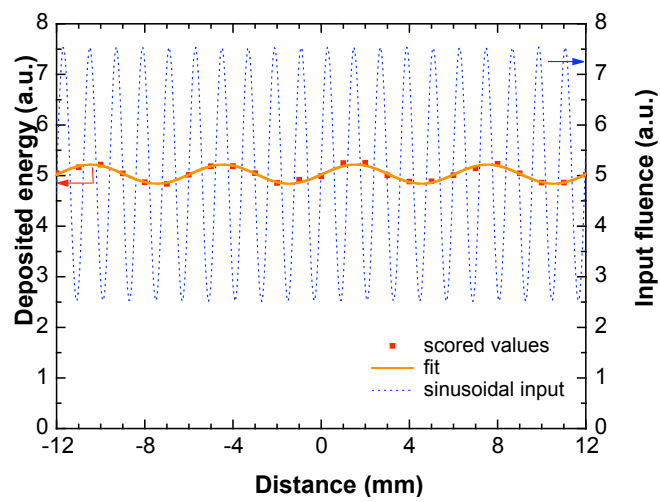
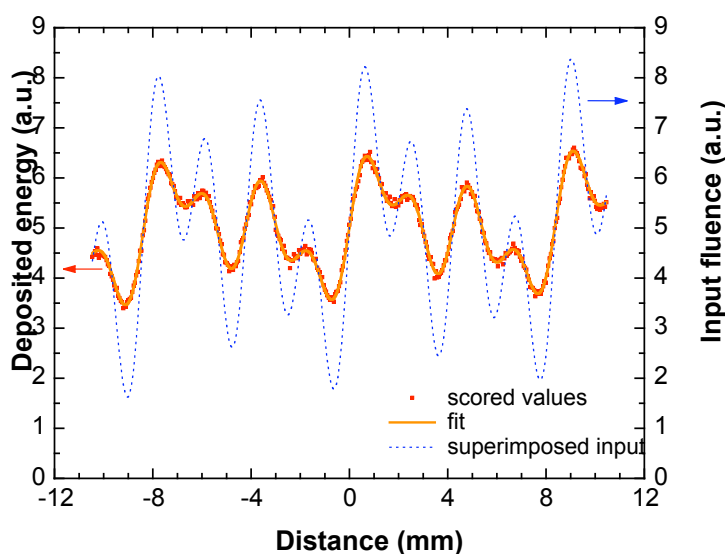


Figure 4.15 Sinusoidal input signals and corresponding scored and fitted sinusoidal output signals for two different wavelengths and tilt angles. The scored values represent the amount of deposited energy in the gas of the detector elements. Panel (a) shows the result for a sinusoidal input with a wavelength of 8.1 mm. Panel (b) was acquired with a sinusoidal input with a wavelength of 1.2 mm. Note the phase shift of 180 degrees between input and output signal. Panel (c) illustrates the importance of slanting the sinusoidal input signal. The same sinusoidal input as in (b) was employed with the exception that the input was aligned with the detector array (0 degree tilt angle). This results in 1 sample/mm. Consequently, the input signal is undersampled since the chosen frequency of the sinusoidal input is beyond the cutoff frequency. The output is interpreted as a sine wave with a lower frequency due to the aliasing effect. For the purpose of comparison, the input and output signal were normalized to the same average signal for all panels.

To make the calculation of MTF_{pre} more efficient, several sine waves having different frequencies can be superimposed to generate a new input signal. To illustrate this idea, three sine waves with the wavelengths of 8.1 mm, 4.2 mm and 1.2 mm were superimposed. Each sinusoidal contribution was weighted equally. Figure 4.16 shows the resulting fit through the scored values. The associated values of MTF_{pre} agree within 1% with the values of MTF_{pre} derived from the approach using single sine wave inputs. In general, this approach allows the



determination of MTF_{pre} up to, for instance, the first zero-crossing in a single simulation.

Figure 4.16 Superimposed sinusoidal inputs. To make the slanted sine wave approach more efficient, an input signal consisting of the superposition of sinusoids with different spatial frequencies can be generated. The figure shows an example of three superimposed sine waves. Each sinusoidal contribution was weighted equally. The fit through the scored values allows the determination of the MTF_{pre} values belonging to the individual sinusoids.

4.2.5.2. Slanted slit approach

Similar to the slanted sine wave approach, the slanted slit technique yields a one-dimensional representation of MTF_{pre} . It was implemented using the Monte Carlo method. Figure 4.17 shows the central part of the LSF for four different wall thicknesses of the detector array. The magnitude of the LSF decreases with increasing wall thickness. Thus, thicker walls reduce the amount of crosstalk more effectively. Interestingly, the signal of the LSF around the origin is also higher for thinner walls. This observation can mainly be attributed to the larger volume of gas available for signal generation for smaller wall thicknesses. For very thin walls, including the zero μm wall thickness, however, the signal decreases again since the Compton-scattered photons, originating from the interactions of the primary photons, are not very likely to interact again in the element and thus do not produce any additional high-energy electrons. The prominent maxima and minima of the LSF can be attributed to the inhomogeneous nature of the detector. The maxima indicate the locations of metal, whereas the minima the ones of the gas cavities. Figure 4.18 shows the four corresponding MTF_{pre} . All MTF_{pre} extend beyond the cutoff frequency, that means the corresponding detector designs are undersampled. MTF_{pre} for a zero wall thickness rapidly goes to zero indicating a broad signal distribution in real space. This finding illustrates the importance of the metal array in reducing the extent of crosstalk.

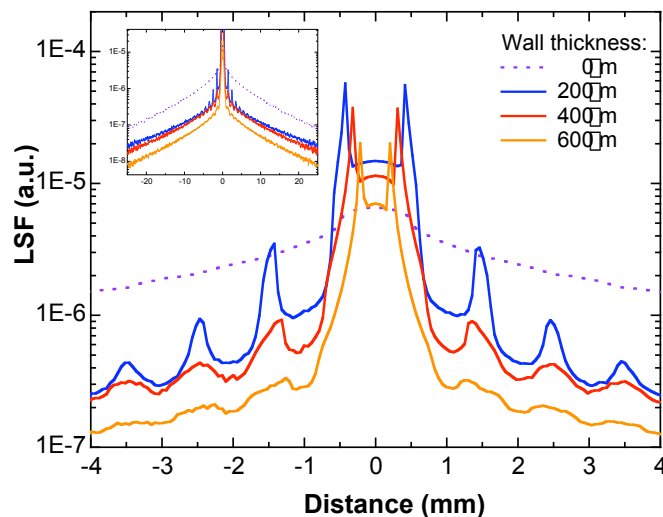


Figure 4.17 Central part of the LSF for different metal wall thicknesses of the detector array and a fixed element width of 1 mm acquired with the slanted slit technique. The prominent maxima and minima are a direct consequence of the inhomogeneous nature of the detector. The maxima indicate the locations of metal, whereas the minima the ones of the gas cavities. A wall thickness of 0 μm corresponds to a hypothetical detector consisting of a xenon gas detection medium only. In this specific case, the signal is generated by integrating the deposited energy in the gas over $1 \times 1 \times 40 \text{ mm}^3$ volumes. The inset shows the LSFs over the whole calculated range.

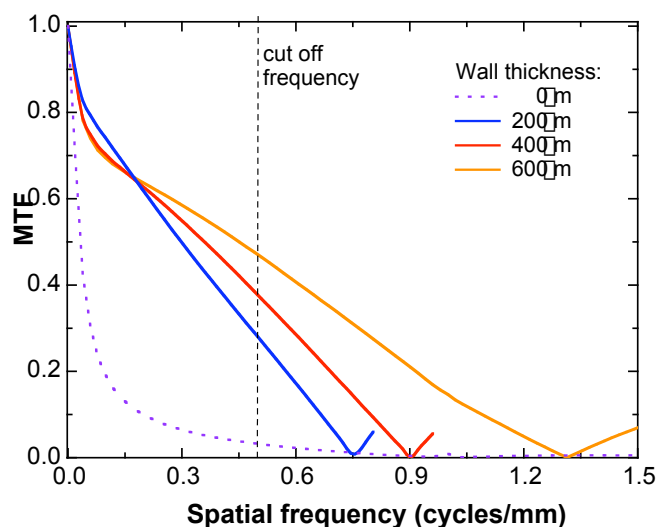


Figure 4.18 MTF_{pre} for different wall thicknesses derived from the LSFs shown in figure 4.17. The vertical dashed line indicates the cutoff frequency given by the detector pitch. Any non-zero value of MTF_{pre} beyond that frequency contributes to the aliasing effect. Except for the case of zero wall thickness, the graphs are plotted just beyond their first zero-crossing.

The curves of MTF_{pre} for wall thicknesses greater than zero show two interesting features. First, the first zero-crossing depends on the wall thickness and secondly, there is a drop of MTF_{pre} at low frequencies particularly pronounced for larger wall thicknesses. The location of the first zero-crossing can be explained qualitatively. For large wall thicknesses, a certain fraction of high-energy electrons, produced in Compton events, get absorbed in the metal before they can reach the gas cavity. The effective area, from where a sufficient number of high-energy electrons can reach the gas cavity, is smaller than $1 \times 1 \text{ mm}^2$. To a first order approximation the width of this area determines the first zero-crossing. Consequently, the Fourier transform has a first zero-crossing beyond 1 cycle/mm. On the other hand, for smaller wall thicknesses even high-energy electrons originating from the walls of the surrounding elements can reach the gas cavity of interest, which means the effective area is larger than $1 \times 1 \text{ mm}^2$. Thus, MTF_{pre} for such wall thicknesses have zero-crossings at frequencies below 1 cycle/mm. It will be shown in the following paragraphs that only the central part of the LSF, ranging from about -1 mm to $+1 \text{ mm}$, determines MTF_{pre} at higher frequencies. Figure 4.17 nicely illustrates the dependence of the width of this central part of the LSF and thus of the first zero-crossing on the wall thickness.

The average range of the high-energy electrons R_{CSDA} can be estimated using the continuous-slowing-down approximation (Attix 1986). For this purpose, copper was used as a good approximation for brass. R_{CSDA} was determined to be, on average, on the order of $250 \text{ }\mu\text{m}$. Thus, for a wall thickness of $600 \text{ }\mu\text{m}$, high-energy electrons created in the middle of the wall are not likely to reach the gas cavity. On the other hand, a wall thickness of $200 \text{ }\mu\text{m}$ is still thin enough to be penetrated by the electrons. A more comprehensive analysis would take into account the polyenergetic nature of the photon spectrum. In addition, a large fraction of the

high-energy electrons is released in the forward direction of the incoming photons. Thus, many high-energy electrons travel a significant distance in beam direction before they reach the gas cavity.

Next, the origin of the low-frequency drop of MTF_{pre} was investigated. For this purpose the LSF was represented as a sum of two components. It is assumed that the central part of the LSF can mainly be attributed to the high-energy electrons created by the interacting primary/unscattered photons. These electrons only have a limited range. The tail of the LSF, on the other hand, is mainly caused by scattered photons that undergo further interactions. As already pointed out, the source of these scattered photons are the primary photons, which have interacted in the detector. To estimate the contribution of the scattered photons over the whole investigated range of distances, the tails were fitted to a sum of two Gaussian functions as illustrated in figure 4.19.

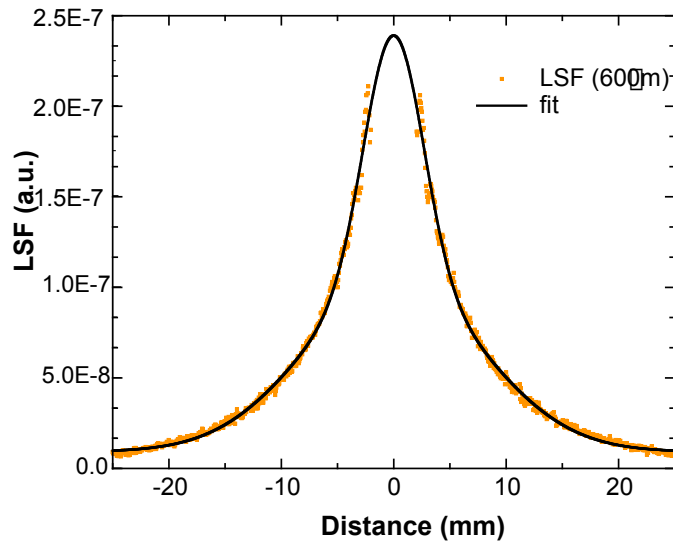


Figure 4.19 Fit through the tails of the LSF for a wall thickness of 600 μm to a function consisting of two Gaussian functions having a narrow and a broad width. This fit represents the contribution of the scattered photons to the LSF. It is assumed that the tails are mainly caused by scattered photons, which undergo further interactions.

This fit was subtracted from the (total) LSF to get the contribution from the primary/unscattered photons. The Fourier transform of the two contributions and a subsequent normalization yielded the corresponding MTF_{pre} as shown in figure 4.20. Their weighted sum is equal to the original MTF_{pre} . As can be seen, the MTF_{pre} for the scattered radiation rapidly goes to zero causing the observed low-frequency drop. This is typical for scattered radiation that usually shows a broad, slowly varying distribution in real space. The MTF_{pre} above a frequency of 0.2 cycles/mm is almost exclusively determined by the primary/unscattered radiation.

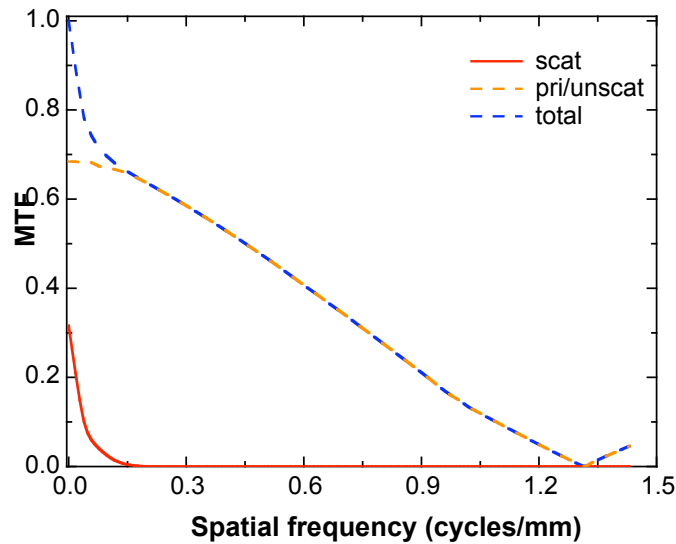
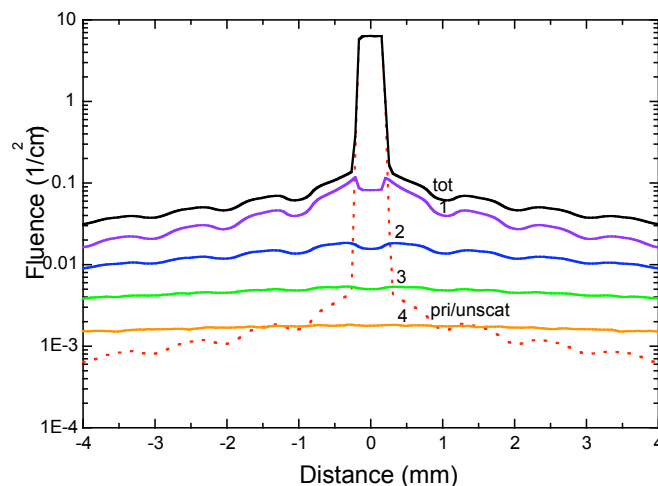


Figure 4.20 The weighted contributions of the scattered (scat) and primary/unscattered (pri/unscat) photons to MTF_{pre} for a wall thickness of 600 μ m. The sum of the two contributions yields the original MTF_{pre} (total).

To verify that the tail of the LSF is caused by the scattered photons, the photon fluence through the gas cavities of the detector elements was determined as a function of the projected distance of the center of the element from the slit beam. The photon fluence was scored separately for the primary/unscattered and the scattered photons. For this purpose, the simulation of the LSF was repeated scoring the fluence rather than the amount of deposited energy. Figure 4.21 shows the fluence distribution for the primary/unscattered and the scattered photons (first order to fourth order scattering). The total fluence is dominated by the incoming primary photons where the slit beam crosses at least a part of a gas cavity. This is the case within the range of approximately -0.23 mm to +0.23 mm as estimated from figure 4.21 (a). The fluence of the primary/unscattered photons outside this range is made up of characteristic x-ray, bremsstrahlung and annihilation photons. Around the central part of the fluence distribution, the fluence of the first order scattered photons dominates, whereas farther away, the fluence of the higher order scattered photons becomes more important. As the fluence of the scattered radiation

is at least more than one order of magnitude higher than for the primary/unscattered photons outside the range of approximately -0.23 mm to +0.23 mm, the energy deposition in this range should also be dominated by the scattered radiation.

(a)



(b)

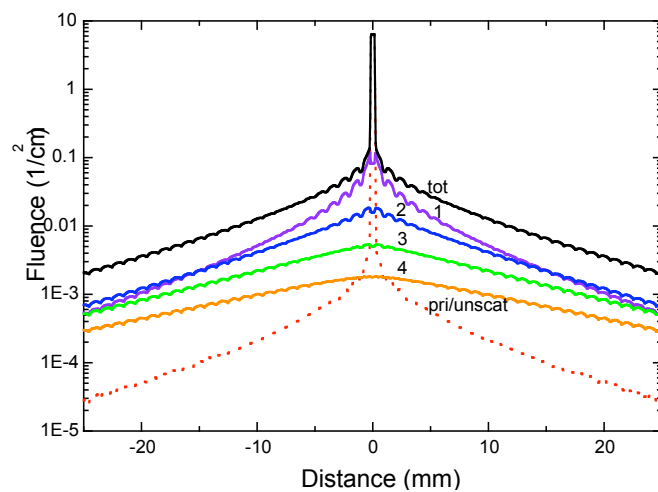


Figure 4.21 Photon fluence through the gas cavities of the detector elements as a function of the projected distance of the center of the element to the slit beam. A line source was employed in the simulation similar to the slanted slit technique. The fluence was separately scored for the primary/unscattered photons (pri/unscat) as well as the first order to fourth order Compton-scattered photons (1, 2, 3 and 4). “tot” designates the total fluence. In addition to the incoming photons, the primary/unscattered component includes other photons such as characteristic x-ray, bremsstrahlung and annihilation quanta, which have, however, a relatively small energy fluence contribution to the

total. Panel (a) shows the scored photon fluence in the proximity of the slit beam. The total fluence is dominated by the incoming primary photons where the slit beam crosses at least a part of a gas cavity. Panel (b) shows the photon fluence over the whole scored range illustrating the increasing importance of the higher order scattered photons.

To investigate the dependence of the accuracy of MTF_{pre} on the number of source particles used for the simulation, the slanted slit simulation for a wall thickness of 200 μm was repeated for different numbers of source particles. Figure 4.22 shows the result for the originally employed numbers of source particles ($1.2 \cdot 10^8$ particles) and for 1/100, 1/1000 and 1/10000 of this number. For $1.2 \cdot 10^6$ particles, there is only a very small deviation from the original MTF_{pre} curve. For $1.2 \cdot 10^3$ and less particles, the results become more or less meaningless. Interestingly, for the range of particles run, the statistical error of the Monte Carlo simulation always adds to the original MTF_{pre} curve (at least for central part of MTF_{pre}). A similar observation was made for MTF_{pre} derived from the oversampled PSF.

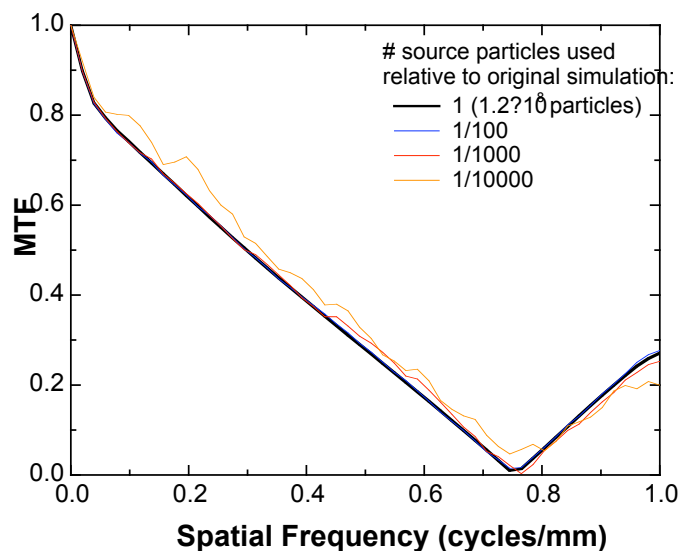


Figure 4.22 MTF_{pre} derived from the LSF for a wall thickness of 200 μm for different numbers of run source particles. The original simulation, employed for all other investigations using the slanted slit approach, employed $1.2 \cdot 10^8$ source particles.

4.2.5.3 Oversampled PSF approach

The oversampled PSF approach relies on the derivation of an oversampled PSF by rastering the central detector element with pencil beams. Figure 4.23 shows the thus determined central part of the two-dimensional oversampled PSF. Figure 4.24 shows a cut through this oversampled PSF along the horizontal axis. As for the LSFs, prominent maxima and minima are visible in these plots. This finding was expected since the LSF can be derived from the PSF by integrating the PSF in a direction which is perpendicular to the axis of the LSF (Barrett and Swindell 1981). The Fourier transform of this PSF and a subsequent normalization yields the two-dimensional MTF_{pre} shown in figure 4.25. This figure illustrates that the central part of MTF_{pre} (up to the first zero-crossing) is approximately rotationally symmetric. Figure 4.26 compares the MTF_{pre} corresponding to values along the positive horizontal and diagonal axis of the two-dimensional

MTF_{pre} . Clearly, the two curves are very similar up to the first zero crossing. Significant differences arise in the first and following sidelobes. Interestingly, figure 4.25 and figure 4.26 show spikes along the horizontal and vertical axis. The origin of these spikes was further analyzed. Figure 4.27 shows a cut through MTF_{pre} along the positive horizontal axis. As can be seen, the spikes occur at multiples of 1 cycle/mm corresponding to the periodicity of the detector array. In addition, their amplitudes are modulated by a sinc function, which has its zero-crossing at multiples of 5 cycles/mm. This modulation is caused by the finite wall thickness of 200 μ m.

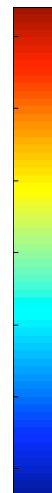


Figure 4.23 Central part of the two-dimensional oversampled PSF acquired by rastering the central detector element with infinitesimally small pencil beams. For each beam the spread of the signal was scored in 51x51 elements. Subsequently, the acquired data was remapped using the reciprocity principle. Finally, the data from all beams was combined to yield an oversampled PSF. The color at a given location indicates the amount of energy deposited in the gas of the central element, when a pencil beam would point at that location. Intriguingly, the metal array is clearly visible in the plot since the metal always generates a significantly higher signal than the surrounding gas. Besides its importance in regard to signal generation, the metal array also reduces the extent of crosstalk. Taking into account the logarithmic nature of the data, the signal contribution rapidly falls off with increasing distance from the central element.

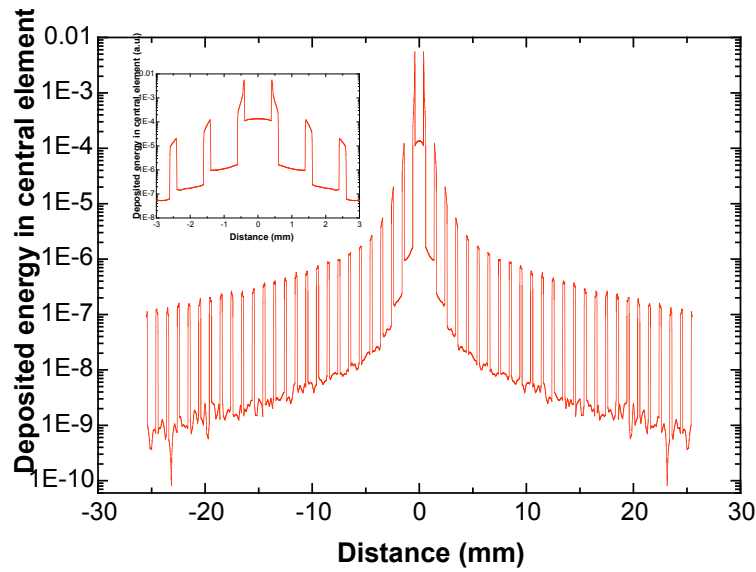


Figure 4.24 Profile through the oversampled PSF shown in figure 4.24 along the horizontal axis showing the prominent maxima and minima. The inset shows an enlarged view of the central part of the profile.



Figure 4.25 Central part of the two-dimensional MTF_{pre} including the first sidelobes derived from the oversampled PSF shown in figure 4.23. The MTF_{pre} up to the first zero-crossing is approximately rotationally symmetric.

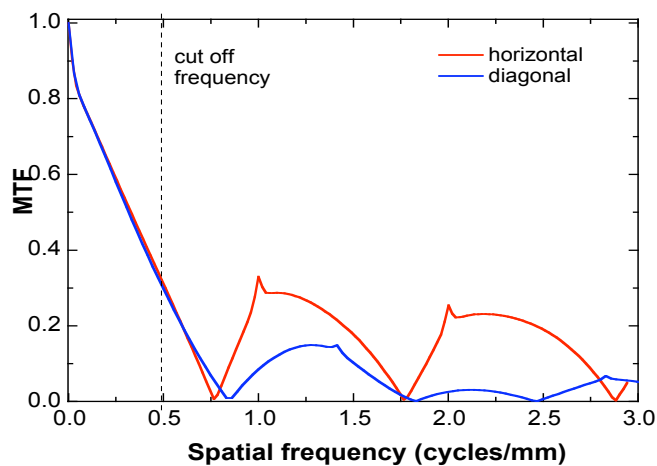


Figure 4.26 One-dimensional MTF_{pre} corresponding to values of the two-dimensional MTF_{pre} shown in figure 4.25 along the positive horizontal and diagonal axis. Both curves are similar up to the first zero-crossing as is expected since the central part of MTF_{pre} is nearly rotationally symmetric. The differences arise in the first and the following sidelobes.

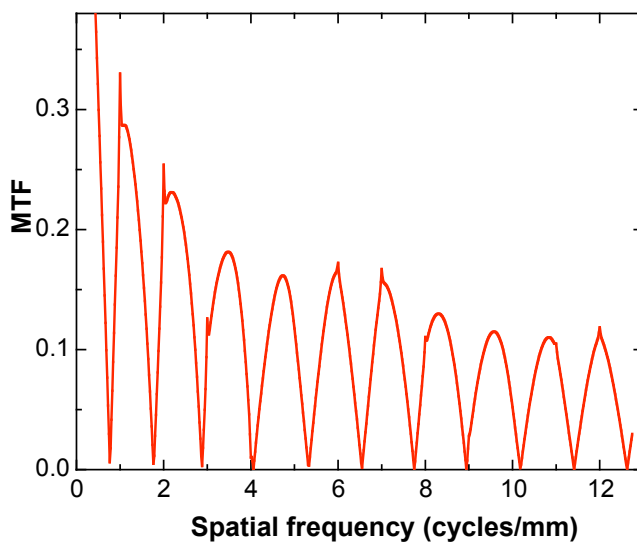
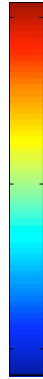


Figure 4.27 Cut through MTF_{pre} along the positive horizontal axis showing the spikes that occur at multiples of 1 cycle/mm resulting from the periodicity of the investigated detector array. Due to the finite wall thickness of 200 μm , the amplitude of the spikes is modulated by a sinc function that has its zero-crossings at multiples of 5 cycles/mm.

To investigate the influence of the wall thickness on the extent of the crosstalk and the signal generation, the oversampled PSF was determined for two different wall thicknesses of 150 μm and 350 μm as shown in figure 4.28. Clearly, the detector array with the smaller wall thickness shows a larger extent of the crosstalk. In addition, both plots illustrate the significance of the metal in regard to signal generation as indicated by the reddish color.

Figure 4.28 Central part of oversampled PSFs for a detector array with a wall thicknesses of 150 μm (left) and



350 μm (right), respectively. The simulation was done for an element size of $1.5 \times 1.5 \times 50 \text{ mm}^3$.

To illustrate the difference between MTF_{pre} and MTF_{d} and to evaluate the influence of the detector inhomogeneity on MTF_{d} , MTF_{d} was determined for a few selected pencil beams. Figure 4.29 shows the MTF_{d} for the pencil beam locations indicated. For the purpose of illustration, the MTF_{d} are plotted along the positive horizontal axis, although these functions are two-dimensional. Interestingly, the MTF_{d} of the pencil beams, which point at the gas cavity, are very similar to each other. In addition, they show only a small decrease in magnitude, indicating that the corresponding undersampled PSFs are very narrow. Both observations were also made for their two-dimensional counterparts as illustrated in figure 4.30. The width of the PSF is

determined by the extent of the crosstalk. Independent of the position of the pencil beam within the gas cavity, the high-energy electrons and the Compton-scattered photons, which potentially contribute to the crosstalk, see and penetrate exactly the same amount of wall material. Thus, a very similar spread of the signal is expected for all of these beams. The MTF_d belonging to beams pointing at the metal, on the other hand, decrease rapidly the farther the beam is located within the metal wall. The MTF_d for the beam pointing at the corner of the element even exhibits a zero-crossing. The more rapid decrease of these MTF_d indicates broader PSFs. Several factors contribute to this increased extent of crosstalk. At first, pencil beams located closer to the adjacent detector element produce high-energy electrons that are more likely to reach the adjacent gas cavity. Next, the Compton-scattered photons are exponentially attenuated in the metal wall. Similar to the interaction of the primary photons, the closer the interaction site of the scattered photon is to the adjacent element the more high-energy electrons can reach the adjacent gas cavity. In addition, more scattered photons can reach elements located even farther away. Figure 4.30 shows two examples of two-dimensional MTF_d derived from pencil beams pointing at the metal.

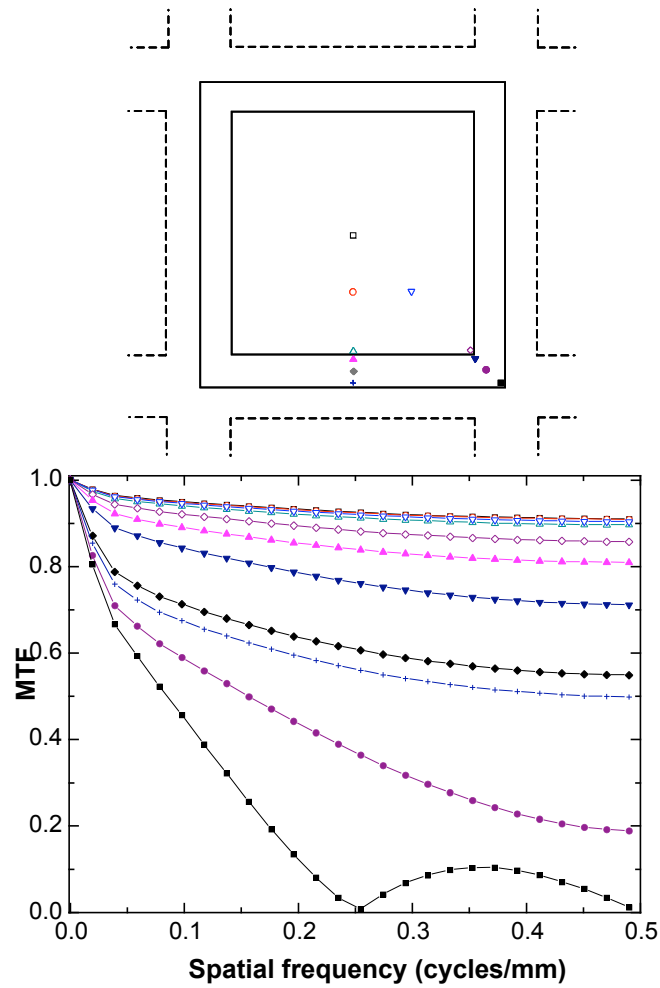


Figure 4.29 Digital MTFs for different pencil beams pointing at the locations indicated. These MTF_d were extracted along the positive horizontal frequency axis of their two-dimensional counterparts. Due to the inhomogeneous nature of the detection medium and to a smaller extent due to undersampling, the shape of MTF_d depends on the location, at which the pencil beam points.

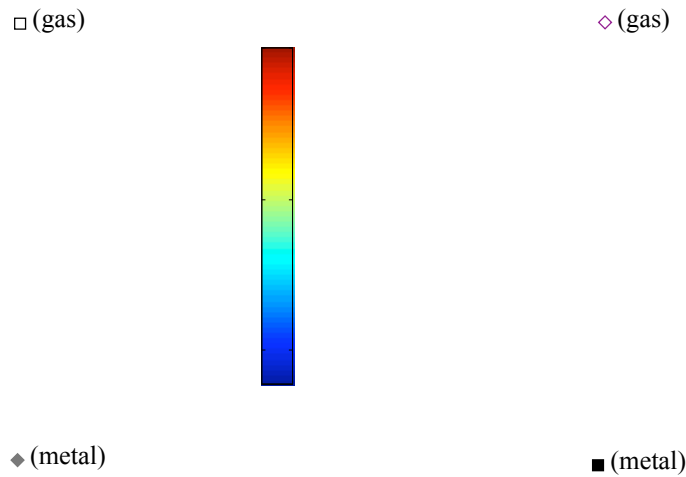


Figure 4.30 Two-dimensional representations of a few selected MTF_d . The location, at which the corresponding pencil beam points, is indicated by the symbol above each plot, which refers to figure 4.29.

4.2.5.4. Comparison of MTF_{pre} derived from the different approaches

Figure 4.31 compares the MTF_{pre} obtained with the three presented methods. The slanted sine wave and the slanted slit approach exhibit an excellent agreement. The oversampled PSF approach shows a small discrepancy especially for the intermediate frequency range. It should be pointed out that this discrepancy is enhanced by the normalization of MTF_{pre} at zero frequency. For the curve derived from the oversampled PSF, the signal was scored in a 51×51 element array for each pencil beam. The other curve shows the result for a scoring array of

31x31 elements. In the latter case the discrepancy with the other methods increases significantly particularly for lower frequencies. Due to the smaller scoring array a smaller part of the tail of the PSF is scored. The tail, however, mostly contributes to the lower frequencies. Both curves derived from the oversampled PSF exhibit a good agreement with the other two methods at higher spatial frequencies. It was found that increasing the size of the scoring array from 31x31 elements to 41x41 elements and finally to 51x51 elements continuously improves the agreement of the derived MTF with the other two approaches. Thus even larger scoring arrays should increase the agreement further. There is also evidence that the PSF is not sampled fine enough. The MTF_{pre} derived from a line input that was aligned at an angle of 4.4 degrees, corresponding to 13 samples per mm as for the oversampled PSF, shows increased values at higher frequencies in comparison to the MTF_{pre} for the slit beam oriented at 3 degrees (corresponding to 19 samples per mm). To evaluate the importance of the locations at which the pencil beams, used to acquire the oversampled PSF, point, the slanted slit technique was repeated for discrete source points along the slit. The locations chosen for the discrete source points were equivalent to the locations at which the pencil beams used for the PSF pointed. The thus determined MTF_{pre} exhibits slightly higher values over a large part of the investigated frequency range in comparison to the MTF_{pre} for a continuous line input. Consequently, the number of pencil beams employed to derive the oversampled PSF as well as the locations at which they point do matter. The derivation of the PSF for a larger scoring array and a higher number of pencil beams, however, is prohibitive due to time constraints. The simulation for a 51x51 element scoring array and a total number of pencil beams of 28, takes about 9.5 days on a cluster of 12 computers (Athlon, 800 MHz).

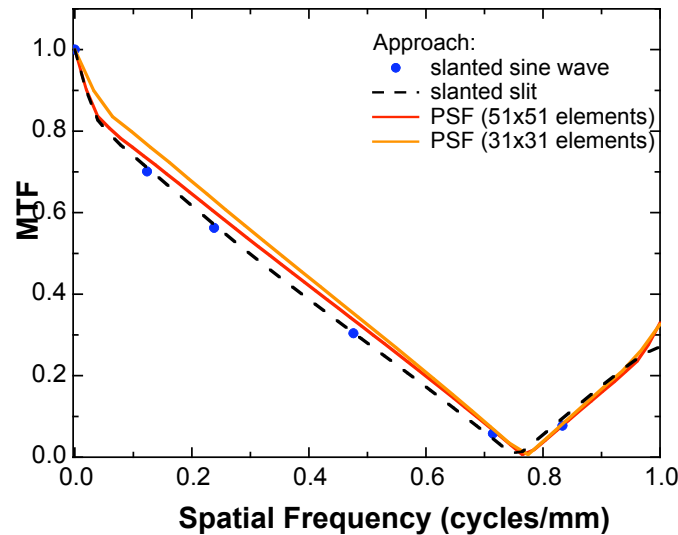


Figure 4.31 Comparison of the determined MTF_{pre} using the slanted sine wave, the slanted slit and the oversampled PSF approach. The slanted sine wave approach results in data points at frequencies, for which a corresponding input sinusoid was simulated. The curve derived from the PSF approach using a 31x31 element scoring array, rather than a 51x51 array, is also shown. It illustrates the importance of scoring a sufficiently large part of the tail of the PSF. The MTF_{pre} from the oversampled PSF approach were extracted from the two-dimensional MTF_{pre} along a line, which was oriented at an angle of 3° with respect to the horizontal axis. The statistical errors associated with the Monte Carlo simulations are minimal (see text for more details).

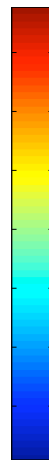
Other issues, which might explain the observed discrepancy, were investigated. The statistical errors associated with the Monte Carlo simulations are considered to be marginal. Cutting the number of simulated source particles in half, does not change the MTF derived from the slanted slit technique, whereas the MTF derived from the oversampled PSF shows slightly higher values at higher frequencies. For the slanted sine wave approach, the standard deviation of the determined amplitude of the fit of the scored sinusoidal output was never larger than a few percent for the frequencies investigated. The goodness of the sinusoidal fits is also illustrated by the reduced chi-square value, which was always close to 1. Any edge effects due to the finite size of the modeled detector were also investigated. For this purpose, the simulation of the slanted slit was repeated for a smaller geometric size of the detector of 81x81 elements rather than 121x121 elements. The changes of the MTF were negligible.

4.2.6 Digital Noise Power Spectrum

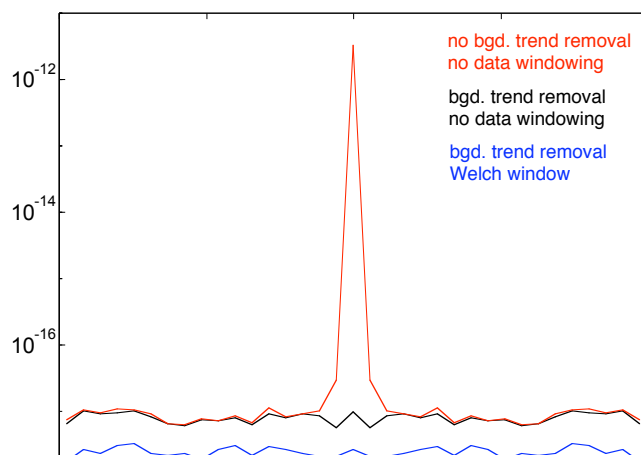
To determine NPS_d , a series of flood field images using the detector model were acquired. Figure 4.32 shows the mean flood field image estimated from the individual flood field images. Within the image, the signal varies by up to 8%. This variation is determined by the number of flood field images used or, conversely, by the total number of source particles employed. Another obvious feature of the estimate is the, on average, slightly lower signal in the corners of the image. This is caused by the finite size of the irradiated area and the geometric area of the detector model. Consequently, the mean flood field image exhibits a background trend, which needs to be subtracted from the individual flood field image according to Eq. (2.8).

Figure 4.32 Average flood field image estimated by averaging over the individual acquired flood field images of the investigated detector model. The, on average, slightly lower signal in the corners of the image can be attributed to the finite size of the irradiated area and the geometric area of the detector model. The noise of this estimate is caused by finite number of flood field images used or, conversely, by the finite total number of source particles employed.

Figure 4.33 shows a preliminary result of NPS_d . This figure also illustrates the importance of the



background trend removal from each flood field image. Without background trend removal,



NPS_d shows a prominent peak at low frequencies caused by the, in real space, slowly varying background trend. With background trend removal, the preliminary estimate of NPS_d seems to be a noisy and flat function. As only an estimate of the true mean flood field image is used, the process of background trend removal is associated with a certain uncertainty. To correct for the finite size of the flood field images, data windows like the Welch, Parzen and Hanning window were applied to the images. The data windowing did not result in a significant change of the shape of NPS_d , but it changed its magnitude. In addition, the value of NPS_d at zero frequency was investigated. NPS_d at zero frequency with background trend removal but without data windowing agreed within about 1% with the corresponding value derived from Eq. (3.6) This proves a proper normalization of NPS_d .

Figure 4.33 Preliminary result of NPS_d . The figure was obtained by cutting through the two-dimensional NPS_d along one of the main frequency axes. The background trend removal from each flood field image removes the prominent peak at low frequencies. To correct for the finite size of the flood field images, different data windows like the Welch window were tested. Although these window functions did not significantly change the shape of NPS_d , they altered its magnitude.

The preliminary result of NPS_d is associated with significant statistical noise. Thus, a considerably larger number of flood field images as well as a larger number of source particles per noise image is required to reduce the noise to an acceptable level. As the simulation of a single noise image takes about 8 hrs (the simulation of the 90 noise images used took roughly one month), there are severe time constraints.

5. Discussion and Conclusions

A main objective of this thesis was the development of small-scale prototype detectors based on the presented novel principle of an efficient detection and imaging of megavoltage photons. Another important objective was the investigation of these prototypes as well as of proposed larger scale detector arrays with Monte Carlo techniques. The findings from the development and experimental characterization of the prototype detectors and from the Monte Carlo simulations provided valuable design considerations for a large-scale detector system.

The high efficiency of the novel concept of megavoltage photon detection in comparison to other existing concepts was already, as pointed out in chapter 1, proven in several other studies. This work provided further evidence. In one experiment the amount of collected charge per gas volume was determined for one of the prototype detectors and compared with the value of a Farmer ionization chamber. The measured charge per collecting gas volume was about 13 times larger for the prototype detector. This prototype was also investigated with Monte Carlo simulations. The contributions of the different components of the detector to the detector signal were determined by adding them one-by-one. As listed in table 4.2, surrounding the gas cavity with the aluminum HV electrode rises the signal by a factor of 12. Although the steel shims occupy a relatively small volume, they also make a significant contribution to the detector signal. These simulations support the idea of placing a sufficient amount of metal, together with the interspersed gas cavities, along the direction of the beam.

It was also shown that the prototype detectors behaved in a predictable way. For instance, the saturation curves measured with the brass tubes (cf. Fig 4.2) are similar to the ones obtained

with conventional ionization chambers (Knoll 2000). This illustrates the fact that the investigated principle of megavoltage photon detection is ultimately based on ionimetry. Similarly, the linear relationship of the detector signal as function of the gas pressure (cf. figure 4.4) was as expected. Another important point is that it can be assumed that the amount of deposited energy in the gas of a cavity is proportional to the actual signal of the detector element (excluding noise). This greatly simplifies the modeling of the behavior of the detector in particular with respect to the Monte Carlo simulations. For most other active media, including scintillators, the relationship between the deposited energy in the active medium and the actual signal is not straightforward.

In general, the experimental studies allowed to draw important conclusions in regard to the design of a large-scale detector system. A problem encountered throughout all measurements was the electromagnetic stray fields and megavoltage x-ray radiation induced signals. The measurements of signal currents in the range of pA to nA is a general problem (Horowitz and Hill 1989, Keithley Instruments 1998). Certain measures are required to reduce the induced signal to an acceptable level. Measurements with pressurized gas have shown that the pressure vessel itself effectively shields the detectors as well as the connectors against electromagnetic stray fields. The ribbon cable, which connected the prototype detectors to the DAS, proved to be reliable particularly when they were wrapped in grounded tin foil. For charge measurements with an electrometer, a triax cable, rather than an ordinary BNC cable, is strongly recommended. In addition, high detector signals, achieved through the use of pressurized xenon gas, resulted in the smallest signal-to-(induced)noise ratios as illustrated in figure 4.3. Another effect that can lead to erroneous readings are leakage currents. These currents can be minimized by careful

guarding. The solution introduced in figure 3.4 was very effective and it can be applied to a large-scale detector. Further problems encountered were short-circuits caused by shims or collecting wires touching the HV electrode. To avoid such problems, a careful machining of uniform detector elements with exactly centered and stable collecting electrodes is required. This would also allow to raise the bias voltage resulting in a somewhat higher charge collection efficiency. Also, Monte Carlo simulations have shown (cf. table 4.5) that a higher primary signal is obtained with thinner electrodes because they reduce the available gas volume less and they are less likely to stop the high-energy electrons crossing the gas cavity. However, there is a lower limit on the thickness of the collecting electrode determined by engineering issues and the occurrence of microphonics (spurious signals that are induced by vibrating parts of the detector).

A high detector signal is desirable for several reasons. At first this minimizes the effect of any induced signal. In addition, high signals are usually easier and more accurately to measure. Finally, the dynamic range of the system is extended. A relatively simple way to increase the detector signal was investigated in this thesis, namely the use of a pressurized gas with a high physical density such as xenon. Pressures up to 25 atm are practical and employed by xenon gas ionization detectors (Drost *et al.* 1984, Peschmann 1981). Unlike kilovoltage imaging, rising the gas pressure increases the DQE of the detector only marginally. A simple calculation shows that the probability of interaction of a 1.6 MeV photon is 0.7% after it traveled through 4 cm of xenon at a pressure of 6 atm. When the pressure is raised to 25 atm the probability of interaction increases to 2.7%. Thus, the DQE is still largely determined by the photons incident on the metal.

Another experiment investigated the issue of alignment of the detector. Unlike for kVCT imaging (Joseph 1981), proper alignment is not critical for megavoltage imaging. It was shown (cf. figure 4.7 and figure 4.8) that a, with respect to the beam axis rotated detector, even exhibits a higher signal. In principle a plain detector array could be built. Normalization of the detector signal can correct for the spatially varying detector response.

The feasibility of the novel concept of megavoltage photon imaging was proven through the acquired MVCT images of a contrast resolution phantom using the single element prototype detectors. The images were associated with a radiation dose of 27 cGy. Other groups (Midgley et al. 1998) (Ford *et al.* 2002, Groh et al. 2002) acquired (cone beam) MVCT images with a comparable image quality at similar doses or sometimes at significantly higher doses. The dose associated with the presented images can be reduced by several means. At first, the entrance window (1.5 cm of aluminum) of the used pressure vessel attenuated the beam by about 20%. On the other hand, it was shown that an aluminum entrance window wall thickness of a few mm can serve as a built-up plate and increase the recorded signal (see below). Another measure is the increase of the detector signal (e.g. through the use of a gas at a higher pressure), which is, as discussed above, favorable in regard to an extended dynamic range and a lower signal-to-noise ratio. Finally, the detector design can be further optimized including the materials used and the dimensions chosen.

One remaining question is how to build a large-scale detector. As a spatial resolution of 1 mm in the object plane is considered to be sufficient for imaging in radiation therapy, a detector element size of about 1.4 to 1.6 mm is required depending on the magnification of the

system. This size is reasonable from the perspective of engineering. In fact, high energy physicists employ detectors consisting of an array of round tubes (Baringer *et al.* 1987, Broll *et al.* 1983). These tubes are called straws and a collection of them form a straw chamber. This chamber is usually run in proportional counter mode to track charged particles (Werner 1999). The tubes are often made of plastic, where the walls are coated with a thin layer of metal. They contain a (usually pressurized) gas and a thin collecting wire running along the central axis of each tube. Many designs are reported. There are straws with a diameter of a few mm and lengths that can exceed 1 m (Oh *et al.* 1991). Besides round tubes, straws with a hexagonal (van-der-Graaf *et al.* 1991) and a rectangular (Inoue *et al.* 1997) cross section are employed. These straw chambers illustrate that the construction of the proposed large-scale detector for megavoltage photons is feasible. The proposed detector in this thesis, however, would be used as an ionization chamber. Ion chambers in principle are the simplest of all gas filled detectors (Knoll 2000). In contrast, proportional counters require a more careful operation. To ensure constant gas gain, the bias voltage has to be precisely controlled (Brinkman and De-Groene 1968, Lampton 1971). Another issue is the required purity of the gas (Braegadze and Maslyaev 1971), which might suffer with time due to microscopic leaks. In addition, proportional counters are almost exclusively used in pulsed mode. The photon fluence in radiation therapy, however, is too high for this kind of mode.

The Monte Carlo simulations of a large detector array resulted in additional design considerations of a multirow/area detector. One important parameter is the wall thickness of the detector array. Figure 4.11 and figure 4.12 as well as table 4.3 show that there is a wall thickness, which results in a maximal primary signal. The maximum is relatively broad giving

greater flexibility with respect to the choice of the wall thickness. At the same time, the total amount of crosstalk detected continuously decreases with decreasing wall thickness. The choice of the most appropriate wall thickness is influenced by many parameters such as the wall material, the amount of crosstalk acceptable, the photon beam spectrum used, etc.

Another important dimension is the length (depth) of the detector in beam direction. It was shown that the attenuation of the primary beam is not necessarily a good measure for the required length. Even when the primary beam is almost completely attenuated by the metal, a certain part of the energy of the high-energy electrons is deposited further downstream requiring a somewhat longer detector as was shown in figure 4.14. This figure also illustrates that a longer detector would result in a larger amount of primary signal detected, whereas the amount of crosstalk would increase by a smaller factor. Of course, the detector should not be made longer than necessary since the cost of the material and machining as well as the weight of the detector increases.

An analysis of the wall material (cf. figure 4.12 and table 4.4) revealed the superiority of high density and high atomic number materials like tungsten. Such materials increase the amount of primary signal recorded whereas the extent of the crosstalk is minimized. Unfortunately, these materials are usually expensive and often difficult to machine. Alternatives include alloys like tungsten/copper (with 10-20% copper to increase the ductility) or metals like molybdenum with somewhat lower densities. Although brass has a significantly lower density and atomic number than tungsten, it offers the great advantage of being very cheap and very easily machined. The analysis of the wall material also revealed that the total signal recorded by

an element in case of a broad beam irradiation is not necessarily a reliable quantity for the detector design evaluation. Although tungsten showed a lower total signal for the investigated range of wall thicknesses than brass (cf. figure 4.12), it results in a higher primary signal and a lower amount of crosstalk.

As the detector array would rest in a pressure vessel with an entrance window for the incoming radiation, the influence of a metal plate in front of the detector was investigated. It was shown that a plate made of aluminum with a thickness of a few mm would increase the amount of primary signal by 4-5%, whereas the crosstalk would nearly be unchanged. Pressure vessels made of aluminum with entrance wall thicknesses on the order of a few mm are commonly employed by xenon gas ionization detectors (Fuchs *et al.* 2000, Peschmann 1981).

Finally, the significance of the photon spectrum used on the detector signal was evaluated. Figure 4.11 shows that a 6 MV beam results in a significantly increased amount of (total) crosstalk whereas the amount of primary signal increases only slightly in comparison to a 4 MV beam. In addition, a higher beam energy leads to an increased radiation dose to the patient. For these reasons, a lower beam energy is recommended.

The DQE(f) is perhaps the single best quantity to evaluate the performance and efficiency of a given detector design. Its determination requires the knowledge of the MTF. The determination of the MTF of a detector with a severely inhomogeneous detection medium, however, has never been investigated in detail before. Three different Monte Carlo-based methods to determine the presampling MTF of x-ray detectors with inhomogeneous detection media have been found.

The MTF_{pre} derived from all three approaches for the investigated detector array agree well with each other. Each method, however, has its strengths and weaknesses. They are to some degree complementary. Besides the MTF_{pre} , the approaches also provide additional insight into the detection process, which is usually more specific for the detector investigated.

The slanted sine wave approach proved to be a very robust technique as illustrated in figure 4.15 (c) and figure 4.16. Unlike the other two approaches, an accurate scoring of any tails is not required since this method relies on the determination of the modulation of the output signal. Contributions from locations far away from the scoring area do not contribute significantly to the modulation. In addition, the slanted sine wave approach is very intuitive and instructive particularly when only one frequency at a time is investigated. The basic meaning of the MTF based on Eq. (2.2) as well as the effect of aliasing can be nicely illustrated (cf. figure 4.15 (c)). Another example is the observed phase shift of 180 degrees between the input and output signal for a sinusoidal input having a wavelength of 1.2 mm. Intriguingly, this effect is well-known in diagnostic radiology, where a star test pattern is imaged with an x-ray film to evaluate the physical size and intensity distribution of an x-ray source (Burgess 1977, Spiegler and Breckinridge 1972). The converging spokes of the star represent the increasing spatial frequency. When the frequency approaches the first zero-crossing of the MTF, the corresponding part of the imaged spokes of the star gets blurred. If the MTF exhibits sidelobes, a 180 degrees phase shift occurs for all frequencies within the first sidelobe resulting in a contrast reversal of the imaged spokes. Regions that originally appeared bright become dark and vice versa. These events may be repeated at lesser radii.

Unlike the oversampled PSF approach, the slanted sine wave method is less computationally intensive. The simulation of a superimposed sinusoidal input takes about 35 hrs on the cluster. A drawback of this method is that it only provides a one-dimensional representation of MTF_{pre} . This is not a serious limitation even in the case of a MTF_{pre} , whose central part is not rotationally symmetric. As the central part of a MTF is well-behaved, it is usually sufficient to know the MTF along the horizontal, vertical and diagonal axis. The MTF_{pre} along the diagonal axis can be acquired by slanting the sinusoidal input appropriately. Another possibility might be the generation of a two-dimensional sinusoidal input. Another possible disadvantage is the required superposition of the sinusoids, which can be awkward.

Similar to the slanted sine wave approach, the slanted slit technique is straightforward to implement. A typical simulation takes about 10 hrs on the cluster. The short time required for a simulation allowed a more detailed analysis of the determined MTF_{pre} . For this purpose, the LSF was split into two components. Barrett and Swindell (Barrett and Swindell 1981) discuss a general approach of splitting a PSF into a primary/unscattered and scattered component. Although there are many possible sources of scattered radiation, the principle of a broad distribution in real space usually holds true. Examples of sources of scattered radiation, which the authors list, are patient scatter and septal penetration. In general, the scattered radiation reduces the contrast of the images. It was shown that the low-frequency drop of MTF_{pre} of the investigated detector was caused by the scattered radiation created within the detector. One author observed the low-frequency drop experimentally for a flat panel imager (Groh 2001). Samei and Flynn (Samei and Flynn 2003) indicate the possibility that the low frequency drop of flat panel imagers employing a phosphor screen (indirect detection method) is caused by the

spread of optical photons. Le Heron and Poletti (Le Heron and Poletti 1988) investigated the MTF including the low-frequency drop of 25 x-ray image intensifiers. In this case the drop is caused by the veiling glare of the image intensifiers.

The scoring of the primary and scattered photon fluence illustrated another distinctive feature of the investigated detector. Most of the detectors for megavoltage photons like flat panel imagers or camera and metal/phosphor plate combinations are only a few millimeters thick. The detector investigated in this work, however, consists of a several centimeter thick metal array. Therefore, primary photons that interact in the detector produce significant numbers of scattered photons, which are much more likely to undergo further interactions than in other types of detectors.

The MTF_{pre} derived from the slanted slit technique exhibits excellent agreement with the data from the slanted sine wave approach. Unlike the oversampled PSF, the slanted slit technique does not employ multiple pencil beams. Thus, a large number of photons can be simulated to ensure good statistics in particular in the tail part of the LSF. Simulations for different numbers of emitted source particles have shown that only a small number of source particles is required for a reliable and accurate estimate of MTF_{pre} . Such an estimate could be acquired within a few minutes on a standard desktop computer. The MTF_{pre} , determined with the slanted slit technique is a one-dimensional representation, which is, however, not a serious limitation as discussed for the slanted sine wave approach.

Unlike the other two methods discussed, the result of the oversampled PSF is a two-dimensional MTF_{pre} . With a total simulation time of about 10 days, however, this method is

computationally intensive. In addition, its implementation is somewhat awkward especially the simulation of multiple pencil beams and the subsequent remapping of the data. The MTF_{pre} derived from the oversampled PSF shows a small discrepancy in comparison to the MTF_{pre} derived from the other methods. Besides MTF_{pre} , the oversampled PSF approach provides the data required to determine MTF_d . For a homogeneous detector, the differences in the shape of MTF_d (solely) arise from undersampling (Boone et al. 1996, Dobbins III 1995). The discrepancy between the MTF_d is largest for a pencil beam pointing at the center of a detector element and a pencil beam pointing at the edge of the element. The situation for the investigated detector array is quite different. The MTF_d belonging to a pencil beam that points at the center of the gas cavity is not very different from the MTF_d belonging to a beam pointing at the edge of the cavity. Within the metal, the shape of the MTF_d , however, change rapidly with distance. These observations illustrate that not undersampling but mostly the binary nature of the investigated detector causes the observed differences in the shape of the MTF_d . In virtue of the binary nature of the detector, a determination of an average MTF_d in form of the EMTF is not reasonable. The MTF_d , on the other hand, describes the response of the system to a point like object, which can be positioned anywhere with respect to the detector.

Another important point is the sidelobes of MTF_{pre} . Principally, the sidelobes are of great importance as they result in aliasing and in the transfer of high-frequency noise. The amplitude of the sidelobes derived from the Monte Carlo simulations, however, are generally overestimated. A measured MTF_{pre} is always the product of the MTF of the detector and of the x-ray source. The finite size of the source is associated with a MTF that can significantly reduce the amplitude of the sidelobes (focal spot blurring (blooming)) when the object, like the

collimating slit, is placed some distance away from the detector (Curry III *et al.* 1990). Although the sidelobes have practical consequences, it is not required to know them accurately. At first, the determination of the digital DQE requires the knowledge of the MTF only up to the cutoff frequency. In addition, the digital NPS characterizes the effect of the high-frequency noise. It can be determined independently of the MTF and thus of the sidelobes.

The thus determined MTF_{pre} can be employed for detector design evaluation. As an example, MTF_{pre} was determined for different wall thicknesses. Similarly, the significance of the wall material, the gas pressure, etc. could be investigated. The derived MTF_{pre} must be interpreted properly. For instance, when MTF_{pre} exhibits high values up to the cutoff frequency, the signals are transferred efficiently through the detector system for all frequencies of interest. At the same time, however, the system can suffer from significant aliasing. A fast dropping MTF_{pre} , on the other hand, might exhibit less aliasing at the cost of a reduced signal transfer at higher frequencies.

In general, the strength of the presented Monte Carlo-based determination of MTF_{pre} is more of a comparative nature. The MTF_{pre} of different detector designs can be compared with each other. In addition, the simulations provide insight into physical processes, which cannot easily be investigated experimentally or analytically. All three presented methods to determine MTF_{pre} can be applied to a broad range of digital x-ray detectors with homogeneous as well as inhomogeneous detection media, both in the diagnostic as well as in the megavoltage energy regime.

The other quantity required to determine the digital DQE is NPS_d . The possibility to determine NPS_d of the investigated detector array using Monte Carlo methods was investigated in this thesis. It was found that the determination of NPS_d is severely hampered by the time requirements. The NPS_d determined from the limited number of acquired flood field images is a noisy and flat function. Typical NPS found in the literature (Dainty and Shaw 1974, El-Mohri et al. 2001, Munro *et al.* 1987, Williams *et al.* 1999), both digital and analog ones in the diagnostic as well as in the therapeutic energy regime, fall off at higher frequencies. It was also shown (Giger et al. 1984) that aliasing can reduce the extent of the fall off. For the investigated detector array, it is difficult to judge the consequences of the aliasing effect and the contribution of the sidelobes to NPS_d . The work done so far indicates that the computer cluster of the Department of Medical Physics at the University of Wisconsin – Madison is not sufficient to get a satisfactory statistics. To simulate a sufficient number of flood field images (using a sufficient number of source particles per image) within a reasonable amount of time, a larger-scale computer cluster like the CONDOR project at the University of Wisconsin – Madison is required. Still, it is not guaranteed that a sufficient number of flood field images can be simulated within a reasonable amount of time. Another possibility is variation reduction techniques, i.e. techniques that speed up Monte Carlo simulations. However, great care is required for their implementations since noise is a second order effect. In addition, any possible noise correlations can easily be destroyed.

This thesis dealt with the development of a novel efficient detector system for megavoltage photons. Experimental studies as well as Monte Carlos simulations resulted in a wealth of

important design considerations. Based on these findings, a large-scale prototype detector system consisting of several hundred elements and ultimately a full-scale detector could be built.

References

Antonuk L E, Yorkston J, Boudry J, Longo M L, Jimenez J and Street R A 1990 Development of hydrogenated amorphous silicon sensors for high-energy photon radiotherapy imaging *IEEE T. Med. Imaging* **NS-37** 165-170

Antonuk L E, Yorkston J, Boudry J, Longo M L and Street R A 1991a Large area amorphous silicon photodiode arrays for radiotherapy and diagnostic imaging *Nucl. Instrum. Meth. A* **310** 460-464

Antonuk L E, Boudry J, Kim C W, Longo M J, Morton E J, Yorkston J and Street R A 1991b Signal, noise, and readout considerations in the development of amorphous silicon photodiode arrays for radiotherapy and diagnostic imaging *Proc. SPIE* **1443** 108-119

Antonuk L E 1993 Thin-film, flat-panel imagers: A coming revolution in megavoltage and diagnostic x-ray imaging *Phys. Medica* **9** 63-68

Attix F 1986 *Introduction to Radiological Physics and Radiation Dosimetry* (New York, NY: John Wiley & Sons)

Baily N A, Horn R A and Kampp T D 1980 Fluoroscopic visualization of megavoltage therapeutic x ray beams *Int. J. Radiat. Oncol. Biol. Phys.* **6** 935-939

Balog J 1998 Tomotherapy dosimetry and the tomotherapy benchtop *Ph.D. thesis* Department of Medical Physics, University of Wisconsin, Madison, WI

Baringer P, Jung C, Ogren H O and Rust D R 1987 A drift chamber constructed of aluminized mylar tubes *Nucl. Instrum. Meth. A* **254** 542-548

Barnes G T 1982 Radiographic mottle: a comprehensive theory *Med. Phys.* **9** 656-667

Barrett H H and Swindell W 1981 *Radiological Imaging: The Theory of Image Formation, Detection, and Processing* (New York, NY: Academic Press)

Boag J W 1973 Xeroradiography *Phys. Med. Biol.* **18** 3-37

Boone J M, Yu T and Seibert J A 1996 Sinusoidal modulation analysis for optical system MTF measurements *Med. Phys.* **23** 1955-1963

Boyer A L, Antonuk L, Fenster A, van Herk M, Meertens H, Munro P, Reinstein L E and Wong J 1992 A review of electronic portal imaging devices (EPIDs) *Med. Phys.* **19** 1-16

Braegadze Y I and Maslyaev P F 1971 Unit for the continuous pumping of gas through a proportional counter under a variable pressure *Instrum. Exp. Tech.* **14** 73-74

Briesmeister (ed) J F 1997 MCNP - a General Monte Carlo N Particle Transport Code *Los Alamos National Laboratory Report*

Brinkman A C and De-Groene P 1968 Proportional counter with automatic gain control *Nucl. Instrum. Meth.* **66** 316-320

Broll C, Charveys A, Declais Y, Favier J, Lebeau M, Moynot M and Perrot G 1983 Large drift tube arrays with external delay line readout *Nucl. Instrum. Methods* **206** 385-395

Bunch P C, Huff K E and Van Metter R 1987 Analysis of the detective quantum efficiency of a radiographic screen-film combination *J. Opt. Soc. Am. A* **4** 902-909

Bunch P C 1989 Detective quantum efficiency of selected mammographic screen-film combinations *Proc. SPIE* **1090** 67-77

Burgess A E 1977 Interpretation of star test pattern images *Med. Phys.* **4** 1-8

Cunningham I A, Westmore M S and Fenster A 1994 A spatial-frequency dependent quantum accounting diagram and detective quantum efficiency model of signal and noise propagation in cascaded imaging systems *Med. Phys.* **21** 417-427

Cunningham I A 1997 Degradation of the detective quantum efficiency due to a non-unity detector fill factor *Proc. SPIE* **3032** 22-31

Cunningham I A 2000 Applied linear-systems theory *Physics and Psychophysics* ed J Beutel, H L Kundel and R L Van Metter (Bellingham, WA: SPIE) pp 79-159

Cunningham I A, Yao J and Subotic V 2002 Cascaded models and the DQE of flat-panel imagers: noise aliasing, secondary quantum noise and reabsorption *Proc. SPIE* **4682** 61-72

Curry III T S, Dowdey J E and Murry R C 1990 *Christensen's Physics of Diagnostic Radiology* (Philadelphia, PA: Lea & Febiger)

Dainty J C and Shaw R 1974 *Image Science* (London, United Kingdom: Academic Press)

Dobbins III J T, Chotas H G and Benveniste H 1992 Direct digitization of optical images using a photostimulable phosphor system *Med. Phys.* **19** 1071-1080

Dobbins III J T 1995 Effects of undersampling on the proper interpretation of modulation transfer function, noise power spectra, and noise equivalent quanta of digital imaging systems *Med. Phys.* **22** 171-181

Dobbins III J T, Ergun D L, Rutz L, Hinshaw D A, Blume H and Clark D C 1995 DQE(f) of four generations of computed radiography acquisition devices *Med. Phys.* **22** 1581-1593

Dobbins III J T 2000 Image quality metrics for digital systems *Physics and Psychophysics* ed J Beutel, H L Kundel and R L Van Metter (Bellingham, WA: SPIE) pp 161-222

Drost D J and Fenster A 1982 A xenon ionization detector for digital radiography *Med. Phys.* **9** 224-230

Drost D J, Mehuys D and Fenster A 1984 A xenon ionization detector for scanned projection radiography: Xenon/Freon 13B1 comparison *Med. Phys.* **11** 610-617

Dutreix A 1984 When and how can we improve precision in radiotherapy? *Radiother. Oncol.* **2** 275-292

El-Mohri Y, Jee K, Antonuk L, Maolinbay M and Zhao Q 2001 Determination of the detective quantum efficiency of a prototype, megavoltage indirect detection, active matrix flat-panel imager *Med. Phys.* **28** 2538-2550

Falco T, Wang H and Fallone B G 1998 Preliminary study of a metal/a-Se-based portal detector *Med. Phys.* **25** 814-823

Ford E C, Chang J, Mueller K, Sidhu K, Todor D, Mageras G, Yorke E, Ling C C and Amols H 2002 Cone-beam CT with megavoltage beams and an amorphous silicon electronic portal imaging device: potential for verification of radiotherapy of lung cancer *Med. Phys.* **29** 2913-2924

Fuchs T, Kachelriess M and Kalender W A 2000 Direct comparison of a xenon and a solid-state CT detector system: measurements under working conditions *IEEE T. Med. Imaging* **19** 941-948

Fujita H, Ueda K, Morishita J, Fujikawa T, Ohtsuka A and Sai T 1989 Basic imaging properties of a computed radiographic system with photostimulable phosphors *Med. Phys.* **16** 52-59

Fujita H, Tsai D-Y, Itoh T, Doi K, Morishita J, Ueda K and Ohtsuka A 1992 A simple method for determining the modulation transfer function in digital radiography *IEEE T. Med. Imaging* **11** 34-39

General Electric CT/T technology continuum

General Electric 1988 E-DAS Technical Reference Manual (AN59630G)

Giger M L, Doi K and Metz C E 1984 Investigation of basic imaging properties in digital radiography. 2. Noise Wiener spectrum *Med. Phys.* **11** 797-805

Glass M 2001 personal communication

Gordon B M 1981 Data acquisition systems *Technical Aspects of Computed Tomography* ed T H Newton and D G Potts (St. Louis, MO: The C. V. Mosby Company) pp 4133-4158

Griffiths S 1990 Radiotherapy quality control - portal and verification films *Radiography Today* **56** 17

Groh B 2001 *A study of the use of flat-panel imagers for radiotherapy verification* (Düsseldorf, Germany: VDI-Verlag)

Groh B A, Siewerdsen J H, Drake D G, Wong J W and Jaffray D A 2002 A performance comparison of flat-panel imager-based MV and kV cone-beam CT *Med. Phys.* **29** 967-975

Guan H and Zhu Y 1998 Feasibility of megavoltage portal CT using an electronic portal imaging device (EPID) and a multi-level scheme algebraic reconstruction technique (MLS-ART) *Phys. Med. Biol.* **43** 2925-2937

Herring D F and Compton D M J 1971 The degree of precision required in the radiation dose delivered in cancer radiotherapy *British Journal of Radiology Special Report #5: Computers in Radiotherapy* ed A S Glicksman, M Cohen and J R Cunningham (London, United Kingdom: British Institute of Radiology) pp 51-58

Hesse B, Spies L and Groh B 1998 Tomotherapeutic portal imaging for radiation treatment verification *Phys. Med. Biol.* **43** 3607-3616

Hillen W, Schiebel U and Zaengel T 1987 Imaging performance of a digital storage phosphor system *Med. Phys.* **14** 744-751

Hinderer R, Kapatoes J M, Jeraj R, Schmidt R, Keller H, Pearson D W, Fang G, Olivera G and Mackie T R 2001 A novel approach for a highly efficient detector for megavoltage photons (abstr) *Med. Phys.* **28** 1232

Hinderer R, Kapatoes J M, Keller H, Schmidt R, Jeraj R, Ruchala K J, Pearson D W, Fang G, Olivera G H and Mackie T R 2002a Development of a new multielement detector system for megavoltage photons *Proc. SPIE* **4682** 809-818

Hinderer R, Kapatoes J M, Keller H, Jeraj R, Schmidt R, Ruchala K J, Mackie T R and Corradini M 2002b Development of a multielement detector system for megavoltage photons *T. Am. Nucl. Soc.* **86** 225-226

Horowitz P and Hill W 1989 *The Art of Electronics* (Cambridge, United Kingdom: Cambridge University Press)

ICRU 1976 *Determination of Absorbed Dose in a Patient Irradiated by Beams of X and Gamma Rays in Radiotherapy Procedures* (Washington D.C.: International Commission on Radiation Units and Measurements)

ICRU 1986 *Modulation Transfer Function of Screen-Film Systems* (Bethesda, MD: International Commission on Radiation Units and Measurements)

ICRU 1995 *Medical Imaging - The Assessment of Image Quality* (Bethesda, MD: International Commission on Radiation Units and Measurements)

Inoue Y, Kato Y, Maruyama A, Nakano E, Okusawa T, Shimonaka A, Takahashi T, Teramoto Y, Kichimi H, Watanabe Y, Yamamoto A and Yamaoka H 1997 The TOPAZ muon detector *Nucl. Instrum. Meth. A* **385** 248-257

Jaffray D A, Drake D G, Moreau M, Martinez A A and Wong J W 1999 A radiographic and tomographic imaging system integrated into a medical linear accelerator for localization of bone and soft-tissue targets *Int. J. Radiat. Oncol. Biol. Phys.* **45** 773-789

Jaffray D A and Siewerdsen J H 2000 Cone-beam computed tomography with a flat-panel imager: initial performance characterization *Med. Phys.* **27** 1311-1323

Jaffray D A, Siewerdsen J H, Groh B A, Drake D G, Wong J W and Martinez A A 2000 Cone-beam computed tomography on a medical linear accelerator using a flat-panel imager *Proc. 13th Int. Conf. on Computers in Radiotherapy* (Heidelberg, Germany) ed W Schlegel and T Bortfeld (Berlin, Germany: Springer) pp 558-560

Jeraj R 2001 personal communication

Johansson S, Lebedinsky Y A and Predko K G 1991 Experimental MTF measurements of CCD using an interferometrically generated test pattern *J. Imaging Sci.* **35** 320-325

Joseph P M 1981 Artifacts in Computed Tomography *Technical Aspects of Computed Tomography* ed T H Newton and D G Potts (St. Louis, MO: The C. V. Mosby Company) pp 3956-3992

Kahn F M 1994 *The Physics of Radiation Therapy* (Baltimore, MD: Lippincott Williams & Wilkins)

Kalender W A 2000 *Computed Tomography: Fundamentals, System Technology, Image Quality and Applications* (München, Germany: Publicis MCD Verlag)

Kapatoes J M, Olivera G H, Ruchala K J, Smilowitz J B, Reckwerdt P J and Mackie T R 2001a A feasible method for clinical delivery verification and dose reconstruction in tomotherapy *Med. Phys.* **28** 528-542

- Kapatoes J M, Olivera G H, Balog J P, Keller H, Reckwerdt P J and Mackie T R 2001b On the accuracy and effectiveness of dose reconstruction for tomotherapy *Phys. Med. Biol.* **46** 943-966
- Kausch C, Schreiber B, Kreuder F, Schmidt R and Dössel O 1999 Monte Carlo simulations of the imaging performance of metal plate/phosphor screens used in radiotherapy *Med. Phys.* **26** 2113-2124
- Keithley Instruments 1998 *Low Level Measurements* (Cleveland, OH: Keithley Instruments Inc.)
- Keller H, Glass M, Hinderer R, Ruchala K J, Jeraj R, Olivera G H and Mackie T R 2002 Monte Carlo study of a highly efficient gas ionization detector for megavoltage imaging and image-guided radiotherapy *Med. Phys.* **29** 165-175
- Knoll G F 2000 *Radiation Detection and Measurement* (New York, NY: John Wiley & Sons)
- Kuhn H and Schwierz G 1990 Quantitative assessment of image quality *Imaging Systems for Medical Diagnostics* ed E Krestel (Berlin and Munich, Germany: Siemens Aktiengesellschaft) pp 44-60
- Lachaine M and Fallone B G 1998 Monte Carlo detective quantum efficiency and scatter studies of a metal/a-Se portal detector *Med. Phys.* **25** 1186-1194
- Lachaine M, Fourkal E and Fallone B G 2001 Detective quantum efficiency of a direct-detection active matrix flat panel imager at megavoltage energies *Med. Phys.* **28** 1364-1372
- Lachaine M and Fallone B G 2001 Design considerations for direct and indirect active matrix flat-panel portal imagers *Radiol. Oncol.* **35** 63-71
- Lampton M 1971 Feedback control of proportional counter gain *Rev. Sci. Instrum.* **42** 117-119
- Langmack K A 2001 Portal imaging *Brit. J. Radiol.* **74** 789-804
- Le Heron J C and Poletti J L 1988 Measurement of x-ray image intensifier sharpness in the x-ray department *Phys. Med. Biol.* **33** 93-104
- Leong J and Shimm D 1985 A method for consistent precision radiation therapy *Radiother. Oncol.* **3** 89-92
- Lewis D G, Morton E J and Swindell W 1988 Precision in radiotherapy: a linear accelerator based CT system *Megavoltage Radiotherapy 1937-1987 Brit. J. Radiol. Suppl.* **24** 24
- Lewis D G, Swindell W, Morton E J, Evans P M and Xiao Z R 1992 A megavoltage CT scanner for radiotherapy verification *Phys. Med. Biol.* **37** 1985-1999

Lu W 2001 Motion detection and correction in conformal radiotherapy and adaptive tomotherapy *Ph.D. thesis* Department of Medical Physics, University of Wisconsin, Madison, WI

Mackie T, Holmes T, Swerdloff S, Reckwerdt P, Deasy J, Yang J, Paliwal B and Kinsella T 1993 Tomotherapy: a new concept for the delivery of dynamic conformal radiotherapy *Med. Phys.* **20** 1709-1719

Mackie T, Balog J, Ruchala K, Shepard D, Aldridge J, Fitchard E, Reckwerdt P, Olivera G, McNutt T and Mehta M 1999 Tomotherapy *Sem. Radiat. Oncol.* **9** 108-117

Mah D, Rowlands J A and Rawlinson J A 1996 Portal imaging with amorphous selenium: Demonstration of image quality using a photoinduced discharge approach *Med. Phys.* **23** 1031

Marks J E, Haus A G, Sutton H G and Griem M L 1974 Localization error in the radiotherapy of Hodgkin's disease and malignant lymphoma with extended mantle fields *Cancer* **34** 83-90

Marks J E, Haus A G, Sutton H G and Griem M L 1976 The value of frequent treatment verification films in reducing localization error in the irradiation of complex fields *Cancer* **37** 2755-2761

Meertens H, van Herk M and Weeda J 1985 A liquid ionisation detector for digital radiography of therapeutic megavoltage photon beams *Phys. Med. Biol.* **30** 313-321

Metz C E, Wagner R F, Doi K, Brown D G, Nishikawa R M and Myers K J 1995 Toward consensus on quantitative assessment of medical imaging systems *Med. Phys.* **22** 1057-1061

Midgley S, Millar R M and Dudson J 1998 A feasibility study for megavoltage cone beam CT using a commercial EPID *Phys. Med. Biol.* **43** 155-169

Morton E J, Swindell W, Lewis D G and Evans P M 1991 A linear array, scintillation crystal-photodiode detector for megavoltage imaging *Med. Phys.* **18** 681-691

Mosleh-Shirazi M A, Evans P M, Swindell W, Webb S and Partridge M 1998a A cone-beam megavoltage CT scanner for treatment verification in conformal radiotherapy *Radiother. Oncol.* **48** 319-328

Mosleh-Shirazi M A, Swindell W and Evans P M 1998b Optimization of the scintillation detector in a combined 3D megavoltage CT scanner and portal imager *Med. Phys.* **25** 1880-1890

Mosleh-Shirazi M A, Evans P M, Swindell W, Symonds-Tayler J R N, Webb S and Partridge M 1998c Rapid portal imaging with a high-efficiency, large field-of-view detector *Med. Phys.* **25** 2333-2346

Munro P, Rawlinson J A and Fenster A 1987 Therapy imaging: a signal-to-noise analysis of metal plate/film detectors *Med. Phys.* **14** 975-984

Munro P, Rawlinson J A and Fenster A 1990 Therapy imaging: a signal-to-noise analysis of a fluoroscopic imaging system for radiotherapy localization *Med. Phys.* **17** 763-772

Munro P 1995 Portal imaging technology: past, present and future *Semin. Radiat. Oncol.* **5** 115-133

Munro P and Bouius D C 1998 X-ray quantum limited portal imaging using amorphous silicon flat-panel arrays *Med. Phys.* **25** 689-702

Neitzel U, Maack I and Günther-Kohfahl S 1994 Image quality of a digital chest radiography system based on a selenium detector *Med. Phys.* **21** 509-516

NIST 2000 National Institute of Standards and Technology: <http://www.nist.gov/>

Oh S H, Wesson D K, Cooke J, Goshaw A T, Robertson W J and Walker W D 1991 Design and performance of a straw tube drift chamber *Nucl. Instrum. Meth. A* **303** 277-284

Olivera G H, Shepard D M, Ruchala K, Aldridge J S, Kapatoes J M, Fitchard E E, Reckwerdt P J, Fang G, Balog J, Zachman J and Mackie T R 1999 Tomotherapy *Modern Technology of Radiation Oncology* ed J Van Dyk (Madison, WI: Medical Physics Publishing) pp 521-587

Pang G and Rowlands J A 2002 Development of high quantum efficiency flat panel detectors for portal imaging: intrinsic spatial resolution *Med. Phys.* **29** 2274-2285

Park S K, Schowengerdt R and Kaczynski M-A 1984 Modulation-transfer-function analysis for sampled image systems *Appl. Opt.* **23** 2572-2582

Peschmann K R 1981 Xenon gas ionization detectors *Technical Aspects of Computed Tomography* ed T H Newton and D G Potts (St. Louis, MO: The C. V. Mosby Company) pp 4112-4126

Phillips G W 1995 Gamma-ray imaging with Compton cameras *Nucl. Instrum. Meth. B.* **99** 674-677

Phillips G W 1997 Applications of Compton imaging in nuclear waste characterization and verification *IEEE Nuclear Science Symposium, 1997* **1** 362-364

Press H, Flannery B P, Teukolski S A and Vetterling W T 1988 *Numerical Recipes in C: The Art of Scientific Computing* (Cambridge, United Kingdom: Cambridge University Press)

- Rabbini M, Shaw R and Van Metter R 1987 Detective quantum efficiency of imaging systems with amplifying and scattering mechanisms *J. Opt. Soc. Am. A* **4** 895-901
- Rabinowitz I, Broomberg J, Goitein M, McCarthy K and Leong J 1985 Accuracy of radiation field alignment in clinical practice *Int. J. Radiat. Oncol. Biol. Phys.* **11** 1857-1867
- Ruchala K J, Olivera G H, Schloesser E A and Mackie T R 1999 Megavoltage CT on a tomotherapy system *Phys. Med. Biol.* **44** 2597-2621
- Ruchala K J 1999 Megavoltage computed tomography for tomotherapeutic verification *Ph.D. thesis* Department of Medical Physics, University of Wisconsin, Madison, WI
- Ruchala K J, Olivera G H, Schloesser E A, Hinderer R and Mackie T R 2000 Calibration of a tomotherapeutic MCVT system *Phys. Med. Biol.* **45** N27-N36
- Ruchala K J, Olivera G H, Kapatoes J M, Reckwerdt P J and Mackie T R 2002 Methods for improving limited field-of-view radiotherapy reconstructions using imperfect a priori images *Med. Phys.* **29** 2590-2605
- Samei E and Flynn M J 2003 An experimental comparison of detector performance for direct and indirect digital radiography systems *Med. Phys.* **30** 608-622
- Shalev S, Lee T, Leszczynski K, Cosby S, Chu T and Reinstein L 1989 Video techniques for on-line portal imaging *Comp. Med. Im. Graph.* **13** 217-226
- Simpson R G, Chen C T, Grubbs E A and Swindell W 1982 A 4 MV CT scanner for radiation therapy: The prototype system *Med. Phys.* **9** 574-579
- Spiegler P and Breckinridge W C 1972 Imaging of focal spots by means of the star test pattern *Radiology* **102** 679-684
- Spyrou G, Tzanakos G, Nikiforides G and Panayiotakis G 2002 A Monte Carlo simulation model of mammographic imaging with x-ray sources of finite dimensions *Phys. Med. Biol.* **47** 917-933
- Stiersdorfer K and Spahn M 1999 Self-normalizing method to measure the detective quantum efficiency of a wide range of x-ray detectors *Med. Phys.* **26** 1312-1319
- Swain R W and Steckel R J 1966 Beam localization in cobalt and megavoltage therapy during treatment *Radiol.* **86** 529
- Swindell W, Lewis D G and Morton E J 1988 Radiological imaging methods based on a linear accelerator: implementation and application *Brit. J. Radiol.* **61** 717-718

- Swindell W and Gildersleve J 1991 Megavoltage imaging in radiotherapy *Rad. Magazine* **17** 18-20
- Taborsky S C, Lam W C, Sterner R E and Skarda G M 1982 Digital imaging for radiation therapy verification *Opt. Eng.* **21** 888-893
- Tapiovaara M and Wagner R F 1985 SNR and DQE analysis of broad spectrum x-ray imaging *Phys. Med. Biol.* **30** 519-529
- van Herk M and Meertens H 1988 A matrix ionisation chamber imaging device for on-line patient setup verification during radiotherapy *Radiother. Oncol.* **11** 369-378
- van-der-Graaf H, Buskens J, Faber G, Konig A, Rewiersma P and Wijnen T 1991 The honeycomb strip chamber: the application in LHC/SSC experiments and the test results of a prototype *Nucl. Instrum. Meth. A* **307** 220-230
- Visser A G V, Huizenga H, Althof V G M and Swanenburg B N 1990 Performance of a prototype fluoroscopic radiotherapy imaging system *Int. J. Rad. Oncol. Biol. Phys.* **18** 1843-1850
- Wagner R F and Sandrik J M 1979 An introduction to digital noise analysis *The Physics of Medical Imaging: Recording System Measurements and Techniques* ed A G Haus (New York, NY: American Institute of Physics)
- Werner J 1999 Efficiency of a straw chamber detector *Projectwork* Department of Physics, University of Konstanz, Germany
- Williams M B, Mangiafico P A and Simoni P U 1999 Noise power spectra of images from digital mammography detectors *Med. Phys.* **26** 1279-1293
- Wirrwar A, Schramm N, Vosberg H and Müller-Gärtner H W 1999 Influence of crystal geometry and wall reflectivity on scintillation photon yield and energy resolution *IEEE T. Med. Imaging* **3** 1443-1445
- Wu C 2002 Treatment planning in adaptive radiotherapy *Ph.D. thesis* Department of Medical Physics, University of Wisconsin, Madison, WI
- Yaffe M J, Fenster A and Johns H E 1977 Xenon ionization detectors for fan beam computed tomography scanners *J. Comput. Assist. Tomogr.* **1** 419-428
- Yaffe M J 1993 Direct digital mammography using a scanned-slot CCD imaging system *Med. Prog. Technol.* **19** 13-21

Yaffe M J and Rowlands J A 1997 X-ray detectors for digital radiography *Phys. Med. Biol.* **42** 1-39

Yan D, Vicini F, Wong J and Martinez A 1997 Adaptive radiation therapy *Phys. Med. Biol.* **42** 123-132

Zhao W and Rowlands J A 1992 Large-area solid state detector for radiology using amorphous selenium *Proc. SPIE* **1651** 134-143

Zhao W and Rowlands J A 1995 X-ray imaging using amorphous selenium: feasibility of a flat panel self-scanned detector for digital radiology *Med. Phys.* **22** 1595-1604

Zhao W, Blevis I, Germann S, Rowlands J A, Waechter D and Huang Z 1997 Digital radiology using active matrix readout of amorphous selenium: construction and evaluation of a prototype real-time detector *Med. Phys.* **24** 1834-1843